PREDICTION OF TURBULENT HEAT TRANSFER IN A ROTATING NARROW RECTANGULAR CHANNEL (AR = 10) ORIENTED AT 120° FROM THE DIRECTION OF ROTATION

BY

MEHABOOB BASHA N. B.

A Thesis Presented to the
DEANSHIP OF GRADUATE STUDIES

KING FAHD UNIVERSITY OF PETROLEUM & MINERALS

DHAHRAN, SAUDI ARABIA

In Partial Fulfillment of the
Requirements for the Degree of

MASTER OF SCIENCE

In

MECHANICAL ENGINEERING

OCTOBER 2005

In the Name of Allah, Most Gracious, Most Merciful.

KING FAHD UNIVERSITY OF PETROLEUM AND MINERALS
DHAHRAN 31261, SAUDI ARABIA

DEANSHIP OF GRADUATE STUDIES

This thesis, written by **MEHABOOB BASHA N.B** under the direction of his Thesis Advisor and approved by his Thesis Committee, has been presented to and accepted by the Dean of Graduate Studies, in partial fulfillment of the requirements for the degree of **MASTER OF SCIENCE IN MECHANICAL ENGINEERING.**

Thesis Committee

15 – 11 – 1426
Dec 17, 2005

Dr. Mohammad S. Al-Qahtani (Advisor)

12/12/05

Dr. Rached Ben Mansour (Co-advisor)

Dr. Mohammed A. Habib (Member)

Dr. Luai M. Al-Hadhrami (Member)

Dr. Esmail Mokheimer (Member)

Dr.Faleh Al-.Sulaiman
Department Chairman

Dr. Mohammad A Al-Ohali
Dean of Graduate Studies

Date: DEC 27, 2005

Dedicated to My Beloved Mother, Father, Sisters and Brother whose supplications, sacrifice and inspiration led to this wonderful accomplishment

ACKNOWLEDGEMENT

In the name of Allah, Most Gracious, Most Merciful. Read in the name of thy lord and Cherisher, Who created. Created man from a {leech-like} clot. Read and thy Lord is Most Bountiful. He Who taught {the use of} pen. Taught man that which he knew not. Nay, but man doth transgress all bounds. In that he looketh upon himself as self–sufficient. Verily. To thy Lord is the return {of all}.

<div align="right">(The Holy Quran, surah 96)</div>

First and foremost, all praise to Almighty Allah Who gave me courage and patience to carry out this work. I am happy to have had a chance to glorify His name in the sincerest way through this small accomplishment and ask Him to accept my efforts. May He guide us and the whole humanity to the right path (Aameen).

TABLE OF CONTENTS

LIST OF TABLES

LIST OF FIGURES

ABSTRACT (English)

Name: **Mehaboob Basha N.B.**

Title: **Prediction of Turbulent Heat Transfer in a Rotating Narrow Rectangular Channel (AR =10) Oriented at 120º from the Direction of Rotation**

Major: **Mechanical engineering**

Date: **Oct 2005**

A computational study is performed on three-dimensional turbulent flow and heat transfer in a rotating rectangular channel with aspect ratio (AR) of 10:1, oriented at 90º and 120º from the direction of rotation. Focus is on effects of high rotation and high-density ratios on the heat transfer characteristics of the 120°orientation. The finite volume code, FLUENT is used to predict the flow and heat transfer. Computational domain is meshed with fine grids to resolve the near wall viscous layer. The Reynolds stress model (RSM), which accounts for rotational effects, is used to compute the turbulent flow and heat transfer in the rotating channel. The effects of rotation and coolant-to-wall density ratio on the fluid flow and heat transfer characteristics are reported on a moderate range of rotation numbers and density ratios ($0 < Ro < 0.25$ and $0.07 < \Delta\rho/\rho < 0.4$). The computational results are in good agreement with experimental data. The results show that the density ratio, rotation number and channel orientation significantly affect the flow field and heat transfer characteristics in the rotating rectangular channel. Flow reversal occurs at high rotation number and density ratio.

ABSTRACT (Arabic)

ملخص الرسالة (العربية)

اسم الطالب: محبوب باشا ن . ب

عنوان الرسالة: التنبؤ بانتقال الحرارة المضطرب في قناة دوارة ضيقة ذات شكل مستطيل ولها نسبة بعدية 10:1 بزاوية 120 درجة من اتجاه الدوران.

التخصص: هندسة ميكانيكية

تاريخ التخرج: أكتوبر / 2005م

تم عمل دراسة حسابية على سريان مضطرب ثلاثي الأبعاد وانتقال الحرارة في قناة دوارة ذات شكل مستطيل ولها نسبة بعدية 10:1 بزاويتين °90 و°120 من اتجاه الدوران. تركزت الدراسة على تأثير الدوران السريع ونسبة الكثافة العالية على خصائص انتقال الحرارة في الاتجاه 120 درجة. تم استخدام برنامج (Fluent) والذي يعتمد طريقة الحجم المحدود لحسابات السريان وانتقال الحرارة وفيه تم تقسيم النطاق الحسابي إلى تقسيمات صغيرة جدا لتحليل الطبقة اللزجة بجوار الجدار. تم استخدام أنموذج رينولدز للإجهاد لحساب السريان المضطرب وانتقال الحرارة في القناة الدوارة حيث أن هذا الأنموذج يأخذ بعين الاعتبار التأثيرات الناتجة عن الدوران, كذلك تم دراسة تأثير الدوران والنسبة بين كثافة سائل التبريد عن المدخل وكثافته عن الجدار على خصائص كل من السريان وانتقال الحرارة وتم تسجيل نتائج الدراسة لأرقام الدوران في المدى (0 > Ro > 0.25) ونسب كثافة في المدى (0.07 > Δρ/ρ > 0.4) .

النتائج الحسابية التي تم الحصول عليها تتوافق بصورة جيدة مع النتائج العملية والدراسة أوضحت أن نسبة الكثافة ورقم الدوران واتجاه القناة لهم تأثير كبير على خصائص مجال السريان وانتقال الحرارة في حالة القناة الدوارة ذات الشكل المستطيل كما لوحظ حدوث سريان عكسي عند القيم العالية لرقم الدوران ونسبة الكثافة.

NOMENCLATURE

AR   channel aspect ratio.

Cp   specific heat, kJ/kg-K.

D_h,   hydraulic diameter, m.

h   heat transfer coefficient, W/m^2-K.

k   thermal conductivity, W/m-K.

L   length of the duct, m.

L_1, L_2 length of the unheated sections, m.

L_3 length of the heated section, m.

Nu   Nusselt number, hD_h/k.

Pr   prandtl number.

Pr_t turbulent prandtl number.

$\dot{q}$ heat flux, W/m^2.

R_r radius from axis of rotation, m.

Ro   rotation number, $\Omega D_h \big/ W_b$

Re   Reynolds number, $\dfrac{\rho W_b D_h}{\mu}$.

S   arc length, m.

T   local coolant temperature, K.

T_i inlet coolant temperature, K.

T_w wall temperature, K.

u, v & w   the mean relative velocities in x, y, and z –direction respectively, m/s.

u_f friction velocity, m/s.

W_b bulk velocity, m/s.

GREEK SYMBOLS

ρ density of fluid, kg/m^3.

$\Delta\rho/\rho$ density ratio, $\dfrac{T_w - T_i}{T_w}$ (See equation 4.2).

υ dynamic viscosity of the coolant, kg/m-s.

μ laminar viscosity, kg/m.s.

μ_t turbulent viscosity, kg/m.s.

β angle of channel orientation measured from direction of rotation, deg.

Ω Rotational speed, rad/s.

θ Dimensionless temperature, $\left(\dfrac{T - T_i}{\dot{q}/(\rho\,Cp\,u_f)}\right)$ for constant wall heat flux, and

$\left(\dfrac{T - T_i}{T_W - T_i}\right)$ for constant wall temperature.

CHAPTER 1

INTRODUCTION

1.1. Overview

The demand for more power, whether it be thrust from an aircraft engine or shaft horsepower from an industrial gas turbine, provides incentive for gas turbine manufacturers to continually seek improvements in gas turbine performance. One of the ways to increase the performance of a turbine is to raise the turbine inlet temperature. At the same time, blade cooling is required in order to provide an acceptable service life. In general, turbine blades must either be made from superior materials or has superior cooling design or both in order to survive in higher performance turbine [1].

This work is motivated by the need of accurate heat transfer prediction in cooling channels. For efficient gas turbine operation, flow temperatures in the hot gas path exceed acceptable metal temperatures in many regions of the engine. So that the integrity of the parts can be maintained for an acceptable engine life if the blades are cooled. Efficient cooling schemes require accurate heat transfer prediction to minimize regions that are overcooled and, even more importantly, to ensure adequate cooling in high-heat-flux regions.

Turbine blades undergo high rotation. Rotation induces considerable effect on the hydrodynamic and thermal characteristics of internal flow. Hence heat transfer in rotating

heated channel is complex. This aspect is of prime concern for the design of the turbine blade cooling passage.

A smooth rotating duct simulates the condition of the internal cooling passage in the turbine blades. Earlier studies on cooling passages were primarily based on stationary models, which are easier to build and work on. Stationary models neglect the Coriolis and centrifugal buoyancy effects, which affect the velocity, temperature, and turbulence distributions. Rotation causes unstabilization and enhancement of turbulence on one side and stabilization of the flow on the other. Location of the unstabilized and stabilized surfaces depends on the flow direction, rotation direction, and the model orientation. Heat transfer from the unstabilized walls is superior compared to that from the stabilized walls. Therefore, investigating heat transfer characteristics of rotating coolant passages is vital. Unlike a stationary duct, the model (duct) orientation may significantly affect the heat transfer characteristics in rotation. The Coriolis influenced flow distribution depends on the duct orientation and consequently, the heat transfer from the individual surface changes with the model orientation.

1.2. Turbine blade cooling concepts

In addition to high thermal and aerodynamic loads, turbine blades operate at extremely high inertial stresses. Creep and rupture life of the blade material at certain temperatures often define the life of the entire engine. The blade failure explains the level of attention paid to the blade cooling design that is required to support the constantly increasing turbine rotor inlet temperatures (TRIT).

Figure 1.1 shows a sectional view of a typical turbine blade. Many techniques of cooling have been proposed over the years; air cooling, water cooling, steam cooling, fuel cooling, liquid metal cooling, heat pipe, thermosyphon, and so on. The cooling techniques can be classified as follows [2]:

Internal cooling (for external stream temperatures of 1300-1600 K): convection cooling, impingement cooling and internally air-cooled thermal barrier

External cooling (for external stream temperatures > 1600 K): local film cooling, full-coverage film cooling, and transpiration cooling.

1.2.1. Internal cooling

Because of its high thermal load combined with large inertial and dynamic forces, the turbine blade is the most critical component for engine durability. In order to achieve the bulk metal temperatures capability of about 1500 F, required by creep-rupture life characteristics for advanced blade alloys, highly effective blade-cooling techniques are inevitable for long-term durability.

1.2.1.1. Convective cooling

It is one of the earliest forms of cooling used in practice, and it is employed in both industrial and aircraft gas turbines. The coolant air passes through very complex passages, which may include ribs and turbulence generators to increase their effectiveness. Some of the air is bled at the leading edge or the blade tip or the trailing edge, or it goes through an 180^0 return channel to finally be vented near the trailing edge. In general, a blade convection cooling techniques can be subdivided into:

1. Schemes employing straight-through radial holes or channels that may be connected to form multipass, or serpentine, systems in which the air passes through the blade/vane several times before exiting

2. Schemes involving enhanced heat transfer by mean of ribs, dimples, matrixes, pin-fins, or similar devices to extend the cooled surface and promote turbulence.

3. Schemes using impingement cooling to more closely match the cooling to external thermal loads.

4. Swirl cooling schemes utilizing heat transfer augmentation due to centrifugal force field in a strong vortex that is induced inside that blade, primarily for leading edges.

Since the level of internal convective cooling depends on the internal cooling passage surface area and the convection heat transfer coefficient acting over this area, both of these parameters must be maximized for an efficient cooling design. For all cooling systems covered by first two groups, custom tailoring of the cooling passage cross sectional flow provides an effective means of controlling the local Reynolds number, and thereby the local heat transfer coefficient. The simplest form of internal cooling system using airfoil designs generally consists of smooth radial passages of circular, elliptical, or triangular cross section.

1.2.1.2. Jet impingement cooling

The heat flux distribution on the turbine airfoil must be appropriately matched with an effective cooling system that will achieve the desired design temperature distribution

while minimizing the amount of cooling air used. In the leading edge region of the airfoil, this often results in the use of impingement cooling. Impingement cooling refers to the use of orifices through which the coolant flow is accelerated and the resulting jets impinge normal to the target surface. Heat transfer coefficients generated by normal impingement of air jets are generally considerably higher than those obtainable by other conventional methods. Jet impingement cooling, which has proven to be highly effective for turbine nozzles, and where spent air is removed towards the trailing edge through the passage between airfoil inner wall and insert. An important advantage of impingement cooling, particularly, if the design uses metal inserts, is that it is usually relatively easy to modify the geometry for engine temperature up rates or if shortfalls are encountered in a design.

1.2.2. External cooling

1.2.2.1. Film cooling

Another effective way to protect a surface from a hot fluid stream is to inject a cooler fluid under the boundary layer, thus forming a protective layer or film along the surface. The injected fluid can enter the boundary layer in a number of ways, and the possible geometrical arrangement is considerable.

1.2.2.2. Transpiration cooling

For the cooling air to be cooled much more efficiently than that in traditional film cooling based designs, the single layer perforated sheet must be replaced with a multiple-layer sheet structure where the cooling air is routed through a winding path between the layers.

This arrangement is referred to as transpiration cooling. This method approaches an ideal-wall cooling system that can maintain the entire liner at the maximum temperature of the material, avoiding cooler regions that would represent wasteful use of cooling air.
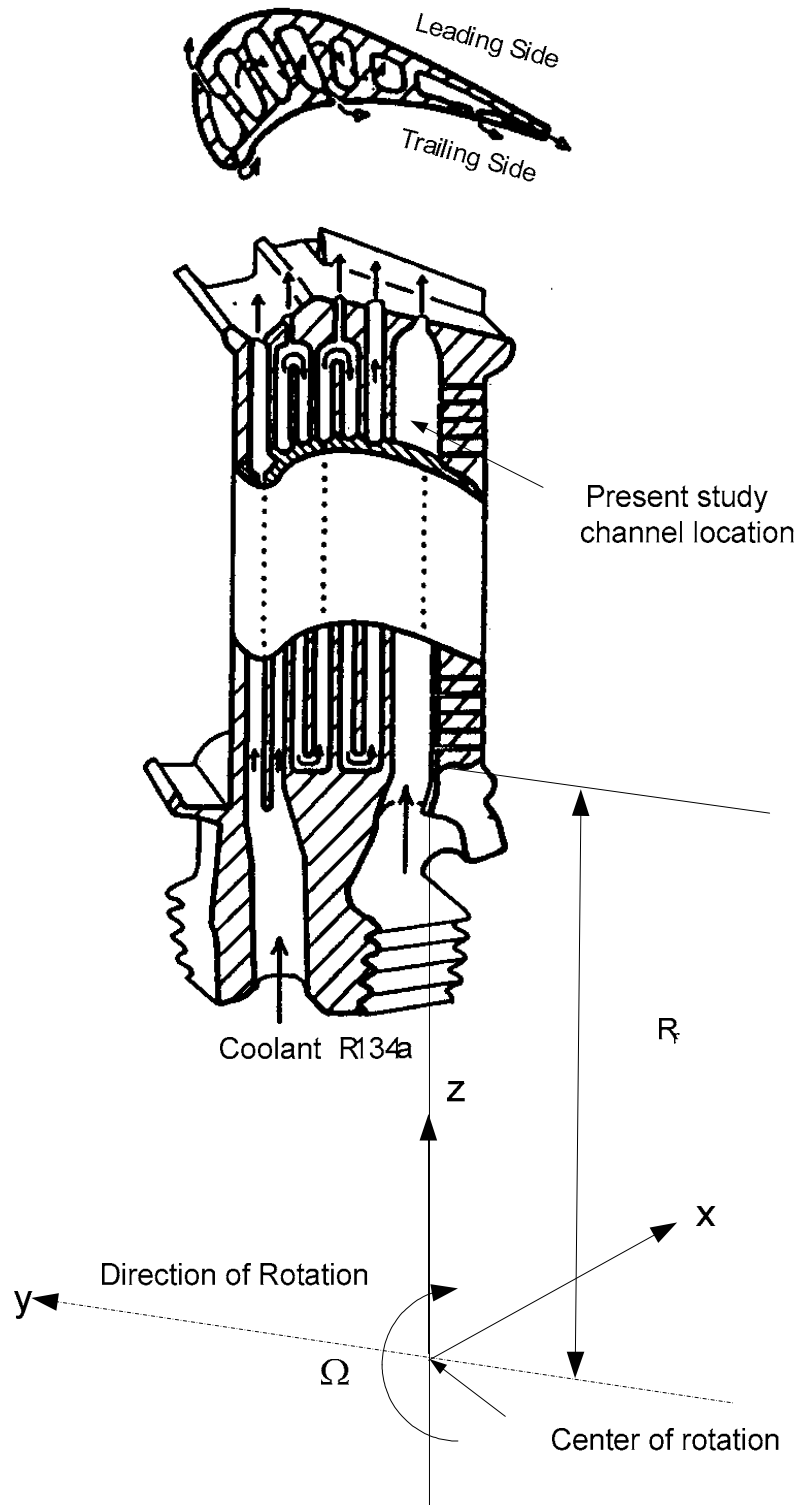
Figure 1.1: A typical turbine blade [2].

CHAPTER 2

LITERATURE REVIEW

2.1. Experimental studies

Morris and Salemi [3] investigated the combined effect of Coriolis and buoyancy forces on forced convection in a circular tube that rotates orthogonally to its centerline. They concluded that, the Coriolis force creates circumferential variations in local heat transfer that tends to improve the heat transfer on trailing edge of the tube in relation to the leading edge, and centripetal buoyancy is shown to increase the local heat transfer further in comparison to that which is caused by Coriolis-driven secondary flow. In this study Morris and Salemi, formulated a new correlating parameter, involving the product of inverse Rossby number with the buoyancy parameter to uncouple the combined effects of Coriolis forces and centripetal buoyancy for there cases. The influence of uneven wall temperature on the local heat transfer coefficient in a rotating one and two pass-square channels with smooth wall has been studied experimentally by Han et al. [4-6]. Results showed that uneven wall temperature enhances the heat transfer co-efficient in rotating channel compared to the uniform wall temperature. This is because of the interactions between rotation-induced secondary flows and uneven wall temperatures. Results also showed that the uneven wall temperature effect on local heat transfer in the second pass is greater than that in the first pass. El-Husayni et al. [6] obtained heat transfer data of stationary and orthogonally rotating asymmetric and symmetric heated smooth and

turbulated channels. For smooth case they concluded that, heat transfer coefficient in stationary mode, did not exhibit appreciable sensitivity to the choice of thermal boundary condition, and same conclusion was drawn for rotating mode with the exception of the results obtained at the highest rotation number tested. Dutta and Han [7] considered the effect of orientation and rotation on heat transfer in three channels. They found that a change in channel orientation about the rotation frame causes a change in the secondary flow structure and the associated flow and turbulence distribution. Consequently, the heat transfer coefficient from the individual surfaces of the two-pass square channel changes. Liou and Chen [8] carried out laser-Doppler velocimetry measurements to view the velocity field in rotating smooth duct with 180 deg straight-corner turn. They mentioned that for stationary duct the sharp turn is found to affect the up and down stream main flow, and also it was stated that sharp turning makes the turbulence intensity levels higher and considerable more nonuniform in the second pass as compared to the first pass. Bons and Kerrebrock [9] developed a momentum integral model for data interpretation, which accounted for Coriolis and buoyancy effects. For the first time, the (transient liquid crystal thermometry) TCLT technique was successfully implemented by Liou et al. [10], to investigate the heat transfer in rotating internal cooling channel. The results show informative spanwise variations of heat transfer enhancement of abatement resulting from rotation. A critical range of Ro is identified, below which the regional averaged Nusselt number ratios of the regions after the 180 deg sharp turn in rotating two-pass cooling passage are rather insensitive to the rotation number. Willett and Bergles [11] performed a detailed investigation of the heat transfer in a narrow, 10:1 smooth rectangular channel oriented to 60° to the r-z plane. Due to limitation in slip ring capacity, lead side and trail

side data could not be obtained simultaneously. The test rig was operated in both directions in order to collect the data on both side, and data were collected at five equally spaced transverse locations, one at the center and two each on either sides of the duct centerline. The five positions are designated as: far forward, center forward, centre line, center aft, and far aft. They studied Nusselt number as a function of both rotation and buoyancy number. Rotation speed was constant through out the investigation. Most of their focus dealt with exploring the contribution of buoyancy forces under rotation. They found that the duct orientation induced a significant variation in the heat transfer coefficient in the span wise direction. They found that the normalized Nusselt number (channel-averaged) of the trailing side is nearly constant over the range of buoyancy number studied, and normalized Nusselt number at the far-aft-end of the trailing side is a strong function of the rotation number and buoyancy number. Normalized Nusselt number of the lead side was shown to increase linearly with increase in buoyancy number, at low range of buoyancy number, and after buoyancy number of 0.2, the normalized number is nearly constant. The result also showed increase in Nusselt number with increase in rotation number at constant density ratio and vice versa. In a subsequent work, Willett and Bergles [12] studied experimentally the same channel but with 90° orientation from the direction of rotation. Again in this investigation the data on both sides were not collected simultaneously. They found the trailing and leading side heat transfer coefficients increase and decrease, respectively, with buoyancy number. In above investigations [11&12] the uncertainty in normalized Nusselt number was calculated to be ± 11.

2.2. Numerical studies

In addition to the experimental studies mentioned above, several studies have been made to predict numerically the flow and heat transfer in radially rotating ducts. First model developed by Wilcox and chambers as mentioned in [13], second and third models for Coriolis effects are based on a study of curved boundary layers by launder et al. as mentioned in [13], were tested for the effect of the Coriolis force on the turbulent structure by Howard et al. [13]. First model gave the most satisfactory prediction while containing no empirical coefficient and maintaining numerical stability at high rotation number. While third model, also predicted well at moderated rotation number. Need for inclusion of Coriolis mode for turbulence was confirmed. Iocovides and launder [14] performed parametric study of flow and heat transfer in rotating rectangular ducts. They found that the transition of stream wise vortices depends on both the cross sectional geometry and flow Reynolds number, and the rotation leads to significant difference between the values of friction factor and Nusselt number on the suction and pressure surfaces of the duct. Prakash and Zerkle [15] studied the flow and heat transfer in radially rotating smooth duct with and without rotation. They considered both the Coriolis and centrifugal-buoyancy effects. Centrifugal buoyancy is shown to increase the radial velocity of the cooler fluid near the trailing wall and decrease the radial velocity of the warmer fluid neat the leading face, and also the rotation is found to increase the heat transfer over the trailing face, while over the leading face, the heat transfer decreases near the inlet but increases downstream. The predictions are found to be quite sensitive to the inlet conditions. Tekrival [16] employed standard and extended

11

k-ε model to predict three-dimensional heat transfer model in orthogonal rotating duct. The conclusion was near wall grid size has a significant effect on the heat transfer calculation when the wall function treatment is used. Relatively large difference between the numerical prediction and experimental data near the inlet are believed to be due to neglect of the inlet swirl in the flow. Prakash and Zerkle [17] again in 1995 studied the flow and heat transfer in radially rotating ribbed duct with and without rotation. They predicted flow and heat transfer using k-ε model with wall function and enhanced near wall treatment as well. Result implied that two-layer model that permits integration to the wall did not yield satisfactory results. Bo et al. [18] has reported the application of several turbulence model (k-ε/one-equation EVM, low-Re EVM, and low-Re ASM) variants to predict the strong heated developing flow through a square duct rotating in orthogonal mode. A k-ε/one-equation EVM produces a most reasonable set of heat transfer prediction, but some deficiencies do emerge at the higher rotation number. New terms for Coriolis and rotation buoyancy has been used for prediction of heat transfer by Dutta et al. [19], modifying k & ε transport equations are shown to give predictions that are in better agreement with the experimental data. Iacovides and launder [20] did a review of computational methods applied to simulate the internal gas turbine blade cooling. This paper attempts to show that progress is being made, particularly in respect to the flow in serpentine blade-cooling passage. They mentioned that the use of wall function cannot give a better than qualitative account of effects of rotation and curvature. The use of second –moment closure in the modeling is shown to be bringing marked improvements in the quality of predictions. Chen et al. [21] employed near wall Reynolds stress closure model and two-layer isotropic eddy viscosity model to compute heat

transfer in rotating two-pass square channels. Results showed that the near-wall second-moment closure model accurately predicted the complex three-dimensional flow and heat transfer characteristics. Flow and heat transfer in a smooth and a ribbed U-shaped duct was simulated by Lin et al. [22]. For smooth U-duct with rotation, Coriolis force and centrifugal buoyancy dominate in the up-leg part of the duct. Al-Qahtani et al. [23] studied numerically rotating normal and twisted channel orientations. RSM model predicted fairly well the complex three-dimensional flow and heat transfer characteristics resulting from sharp 180^0 turn, rotation, centrifugal buoyancy force and channel orientation. They also investigated the effect of the rotation number, Ro, and inlet coolant-to-wall density ratio, $\Delta\rho/\rho$. Results showed that, for $\beta = 90^o$ orientation, the cool fluid is located next to trailing wall in the first pass, where as in the second pass the cool fluid is pushed towards leading wall. This shift in cold fluid location was attributed to change in the Coriolis force direction. For $\beta = 135^o$ orientation, the cool fluid is located next to outer wall in the first pass, where as in the second pass the cool fluid is pushed towards inner wall. Flow reversals were also reported for high rotation number and density ratio, for both channel orientations. They also concluded that the Nusselt number ratios in the first passage trailing and outer surfaces increases with increase in rotation number and density ratio for both $\beta = 90^o$ and $\beta = 135^o$ cases, with the increase in the outer surface being the most for $\beta = 120^o$ case. Al-Qahtani et al. [24] studied numerically smooth and ribbed rectangular channel with aspect ratio of 4:1 for normal and twisted channel orientations. They focused more on effect of rotation number and density ratio on ribbed channel. The study shows considerable spanwise heat transfer difference across the leading and trailing surfaces of smooth duct for $\beta = 135^o$ case. They found that the top

and bottom wall in $\beta = 135^{\circ}$ case, behave like leading and trailing wall of $\beta = 90^{\circ}$ and thus Nusselt number ratios on these surfaces are low and high respectively. Su et al. [25] also performed computation to study the three-dimensional flow and heat transfer in u-shaped duct for various aspect ratio (AR = 1:1, 1:2, and 1:4) under rotation and non-rotating conditions. For all three different aspect ratio ducts, the Nusselt number ratios decrease with increasing Reynolds numbers. For non-rotating ducts, the channel aspect ratio has small effect on spanwise averaged Nusselt number ratio. Belhoucine et al. [26] used explicit algebraic Reynolds stress model to compute turbulent flow in rotating square duct. Their model demonstrated that the Coriolis term produces considerable variation in the structure of turbulence and the mean motion. In the latest research Al-Qahtani et al. [27] used RSM model to predict the flow and heat transfer in smooth rectangular channel with aspect ratio of 4:1 for two channel orientations, $\beta = 90^{\circ}$ and $\beta = 135^{\circ}$. Their focus was on high-rotation and high-density-ratio effects on the heat transfer characteristics of the $\beta = 135^{\circ}$ orientation. They reported that at rotation number Ro of 0.28 and density ratio, $\Delta\rho/\rho$ of 0.2 flow reversal occur near the top wall, and strength of this reverse flow increased with increase in density ratio, $\Delta\rho/\rho$. The flow reversals were attributed to Coriolis-force-induced secondary flow and centrifugal buoyancy. Coriolis-force-induced secondary flow pushes the cold fluid toward the bottom wall, and on the other hand centrifugal buoyancy tends to accelerate cold fluid at the bottom and decelerate the hot fluid at the top wall. They also showed that for high rotation number and high density ratio case, turbulence intensity of $\sqrt{(uu)}/W_b$ components is relatively higher at trailing surface when compared to stationary case, which was due to coriolis driven cross stream flow. The study shows leading Nusselt number at downstream to

increases with increase in rotation number and density ratio, and this was because of flow reversals that take place downstream. Again here it was found that the Nusselt number is high on the bottom surface and low on top wall for a given rotation number and density ratio for $\beta = 135^{o}$ channel orientation.

The primary objective of the present study is to predict the three-dimensional flow and heat transfer for rotating /non-rotating smooth one-pass rectangular channel (AR = 10:1) with two channel orientation ($\beta = 90^{o}$ and 120°) and compare with available experimental data.

CHAPTER 3

MATHEMATICAL MODELING

3.1. Problem description

Figure 3.1 shows the location of the tilted cooling channel in a turbine blade. The cooling passage configuration is smooth rectangular passage with aspect ratio (AR) of 10:1, oriented such that the long sides of the channel cross-section are at $\beta = 90^o$ (in one case) and to the direction of the blade tangential direction. The first configuration (i.e. $\beta = 90^o$) is unlikely to be found in a cooled gas turbine blade, except in an unconventional design. However, it is used here for comparison with the other configuration ($\beta = 120^o$). The $\beta = 120^o$ configuration is found in the trailing edge region of a blade. Figure 3.2 shows the geometry of the computational domain. Two of the four sidewalls, in the rotational direction, are denoted as the leading and trailing wall, respectively, while the other two sidewalls are denoted as the top and bottom walls. The channel hydraulic diameter, D_h, is 4.55 mm. The distance from the inlet of the channel to the axis of rotation (Y-axis) is given by $R/D_h = 36.92$ and the length of the channel is given as $L/D_h = 27$. The channel consists of an unheated starting length ($L_1/D_h = 1.3$), a heated section ($L_2/D_h = 23.12$) corresponding to the test section in Willett and Bergles [11 & 12], and unheated exist section ($L_3/D_h = 1.5$). The arc length S is measured from the beginning of the heated section to its end. The two axial locations at which results are presented are at locations $Z/D_h = 12$ and $Z/D_h = 22$, which is denoted as plane a & b, respectively.

3.2. Mathematical model

3.2.1. Governing equations

The Reynolds-averaged Navier-Stokes equations in conjunction with a Reynolds Stress Turbulence closure models are solved using the commercial software Fluent. In such a system, account must be taken for the Coriolis and centrifugal forces, which appear as source terms in the equations of motion. The governing equations for mean flow variables are [28]:

Continuity:

$$\nabla(\rho\vec{u}) = 0 \tag{3.1}$$

X-Momentum:

$$div(\rho\vec{u}u) = -\frac{\partial p}{\partial x} - 2\rho\Omega w + \rho\Omega^2 x + div[\mu\,grad(u)] + div[-\rho\overline{u'v'}] \tag{3.2}$$

Y-Momentum:

$$div(\rho\vec{u}v) = -\frac{\partial p}{\partial y} + div[\mu\,grad(v)] + div[-\rho\overline{v'w'}] \tag{3.3}$$

Z-Momentum:

$$div(\rho\vec{u}w) = -\frac{\partial p}{\partial z} + 2\rho\Omega u + \rho\Omega^2 z + div[\mu\,grad(w)] + div[-\rho\overline{w'u'}] \tag{3.4}$$

Energy:

$$div(\rho\vec{u}_i T) = div\left[\left(\frac{\mu}{Pr}\right)grad(T)\right] + div[-\rho\overline{u'_i T}] \tag{3.5}$$

The second and third terms on the right hand sides of equation (3.2) and (3.4) occur due to the Coriolis and centrifugal forces, respectively. It is worth to mention here, that the Governing equations are solved in rotating reference frame, where u, v and w represent relative velocity components. Various forces acting on the rotating cooling channel and effect of rotation on the velocity field is shown in the figure 3.3.

3.2.2. Turbulence modeling

The Reynolds stress model involves calculation of individual Reynolds stresses through solving their differential equations. The individual Reynolds stresses are then used to obtain closure of the Reynolds-averaged momentum equation. Following [28] the model equations for the transport of the Reynolds stresses may be written as follows.

$$C_{ij} = D_{ij}^{T} + D_{ij}^{L} + P_{ij} + G_{ij} + \phi_{ij} + \varepsilon_{ij} + F_{ij} \tag{3.6}$$

$$C_{ij} = \frac{\partial}{\partial x_k}\left(\rho \overline{u_i u_i u_j}\right) \qquad \text{is the convective term,} \tag{3.7}$$

$$D_{ij}^{T} = -\frac{\partial}{\partial x_k}\left[\frac{\mu_t}{\sigma_k}\frac{\partial \overline{u_i u_j}}{\partial x_k}\right] \qquad \text{is the turbulent diffusion term,} \tag{3.8}$$

$$D_{ij}^{L} = \frac{\partial}{\partial x_k}\left[\frac{\mu_t}{x_k}\left(\overline{u_i u_j}\right)\right] \qquad \text{is the laminar diffusion term,} \tag{3.9}$$

$$P_{ij} = \left(\overline{u_i u_j}\frac{\partial U_j}{\partial x_k}\right) + \left(\overline{u_i u_k}\frac{\partial U_i}{\partial x_k}\right) \qquad \text{is the stress production term,} \tag{3.10}$$

18

$$G_{ij} = \beta \frac{\mu_t}{\mathrm{Pr}_t} \left(g_i \frac{\partial T}{\partial x_j} + g_j \frac{\partial T}{\partial x_i} \right)$$ is the buoyancy production term, (3.11)

$$\phi_{ij} = \phi_{ij,1} + \phi_{ij,2} + \phi_{ij}^w$$ is the pressure strain term, (3.12)

$$\phi_{ij,1} = -C_1 \rho \frac{\varepsilon}{k} \left(\overline{u_i u_j} - \frac{2}{3} \delta_{ij} k \right)$$ is the slow pressure strain term, (3.12a)

$$\phi_{ij,2} = -C_2 \left[\left(P_{ij} + F_{ij} + G_{ij} - C_{ij} \right) - \frac{1}{3} \delta_{ij} \left[P_{kk} + G_{kk} - C_{kk} \right] \right]$$ (3.12b)

$$k=1,2,3$$

is the rapid pressure strain term,

$$\phi_{ij}^w = C_1' \frac{\varepsilon}{k} \left(\overline{u_k u_m} n_k n_m \delta_{ij} - \frac{3}{2} \overline{u_i u_k} n_j n_k - \frac{3}{2} \overline{u_j u_k} n_i n_k \right) \frac{k^{3/2}}{C_1 \varepsilon d}$$
$$+ C_2' \left(\phi_{km,2} n_k n_m \delta_{ij} - \frac{3}{2} \phi_{ik,2} n_j n_k - \frac{3}{2} \phi_{jk,2} n_i n_k \right) \frac{k^{3/2}}{C_1 \varepsilon d}$$ (3.12c)

is the wall reflection term,

d is the normal distance to the wall. n_k and x_k component of the unit normal to the wall.

$$\varepsilon_{ij} = -2\mu \frac{\overline{\partial u_i \partial u_i}}{\partial x_k \partial x_k}$$ is the dissipation term, (3.13)

$$F_{ij} = -2\rho \Omega_k \left(\overline{u_j u_m} \varepsilon_{ikm} + \overline{u_i u_m} \varepsilon_{ikm} \right)$$ is the rotation term. (3.14)

Where $C_1 = 1.8, C_2 = 0.6$, $C_1' = 0.5,$ $C_2' = 0.3$, $C_l = \dfrac{C_l^{3/2}}{k}$, $C_\mu = 0.09$ & $k = 0.41$ are

the suggested values by FLUENT software.

To close the above system of equations, expressions need to be provided for the turbulence viscosity μ_t and the turbulence prandtl number $\Pr_t$. The turbulent viscosity is obtained using Reynolds Stress Model where k and ε represent the turbulent kinetic energy and rate of dissipation of turbulent kinetic energy respectively.

Turbulent viscosity is expressed involving k and ε as: [28]

$$\mu_t = \rho C_\mu \frac{k^2}{\varepsilon} \tag{3.15}$$

k and ε are solved from the following two transport equations,

$$\rho \frac{Dk}{Dt} = \frac{\partial}{\partial x_j}\left[\left(\mu + \frac{\mu_t}{\sigma_k}\right)\frac{\partial k}{\partial x_j}\right] + \frac{1}{2}(P_{ii} + G_{ii}) - \rho\varepsilon(1 + 2M_t^2) \tag{3.16}$$

where $\sigma_k = 0.82$

$$M_t = \sqrt{\frac{k}{a^2}} \qquad \text{Where } M_t \text{ is Mach number, and } a\left(\equiv \sqrt{\gamma R T}\right)$$

$$\rho \frac{D\varepsilon}{Dt} = \frac{\partial}{\partial x_j}\left[\left(\mu + \frac{\mu_t}{\sigma_\varepsilon}\right)\frac{\partial \varepsilon}{\partial x_j}\right] + C_{\varepsilon 1}\frac{1}{2}(P_{ii} + C_{\varepsilon 3}G_{ii})\frac{\varepsilon}{k} - C_{\varepsilon 2}\rho\frac{\varepsilon^2}{k} \tag{3.17}$$

Where $\sigma_\varepsilon = 1.0, C_{\varepsilon 1} = 1.44, C_{\varepsilon 2} = 1.92$, (are the suggested values by fluent software) and

$C_{\varepsilon 3} = \tanh|v/u|$ where v is the component of the flow velocity parallel to the gravitation vector and u is the component of the flow velocity perpendicular to the gravitational vector as mention in fluent manual [28].

3.3. Near-wall treatment

Turbulent flows are significantly affected by the presence of walls. Obviously, the mean velocity field is affected through the no-slip condition that has to be satisfied at the wall.

The near-wall modeling significantly impacts the reliability of numerical solutions, in as much as walls are the main source of mean vorticity and turbulence. After all it is in the near-wall that the solution variables change with large gradients and the momentum and other scalar transports occurs most vigorously. Therefore, accurate representation of the flow in the near-wall region determines successful predictions of wall-bounded turbulent flows. The turbulence model that we have chosen is primarily valid for turbulent core flows (i.e., the flow in the regions somewhat far from walls). Consideration therefore needs to be given as to how to make these models suitable for wall-bounded flows [28]. There are two approaches for modeling the near-wall region, namely wall function and two-layer model.

3.3.1. Wall function

In first approach, the viscosity-affected inner region (viscous sublayer and buffer layer) is not resolved. Instead, semi-empirical formulas called "wall functions" are used to bridge the viscosity-affected region between the wall and the fully turbulent region. The use of wall function necessitates the need to modify the turbulence models to account for the presence of the wall. Figure 3.4 shows the meshing in the near the wall to use of wall-function approach. In high-Reynolds-number flows, the wall function approach substantially saves computational resource. This is because the viscosity-affected near wall region, in which the solution variables change most rapidly, is not resolved. The wall function approach is popular because it is economical, robust, and reasonably accurate. It is a practical option for the near wall treatment for industrial flow

simulations. Standard wall functions in fluent are based on the proposal of launder and

Spalding [28], and have been most widely used for industrial flows.

The law-of-wall for mean velocity yields

$$U^* = \frac{1}{k}\ln\left(E\,y^*\right) \qquad\qquad (3.18)$$

where

$$U^* = \frac{U_p\,C_\mu^{1/4}\,k_p^{1/2}}{\tau_w/\rho}$$

$$y^* = \frac{\rho\,C_\mu^{1/4}\,k_p^{1/2}\,y_p}{\mu}$$

and k = von karman constant (= 0.42)

   E = empirical constant (= 9.81)

   U_p = mean velocity of the fluid at point P

   k_p = turbulent kinetic energy at point P

   y_p = distance fron point P to the wall

   μ = dynamic viscosity of the fluid

3.2.2. Two-layer model

In second approach, the turbulence models are modified to enable the viscosity-affected

region to be resolved with a mesh all the way to the wall, including the viscous sub-layer.

Two-layer approach is used to solve the problem in this present study. In the two-layer

model, the whole domain is subdivided into a viscosity-affected region and a fully

turbulent region. Near wall meshing for two-layer is shown in Figure 3.4, the division of

the regions is determined by a wall-distance based, turbulent Reynolds number, Rey, defined as

$$Re_y = \frac{\rho \sqrt{k}\, y}{\mu_t} \tag{3.19}$$

Where y is the normal distance from the wall to the cell center. In fluent, y is interpreted as the distance to the nearest wall: $y \equiv \min \left\| \vec{r} - \vec{r}_w \right\|$, Where $\vec{r}$ is the position vector at the field point, and $\vec{r}_w$ is the position vector on the wall boundary.

In the fully turbulent region (Re > 200), the RSM are employed. In the viscosity-affected near-wall (Re < 200), the momentum equations and the k equations are retained as before. While ε is not obtained by solving its transport equations; rather obtained algebraically from the below equation.

$$\varepsilon = \frac{k^{3/2}}{l_\varepsilon} \tag{3.20}$$

The turbulent viscosity, μ_t, is computed from

$$\mu_t = \rho C_\mu \sqrt{k}\, l_\mu \tag{3.21}$$

The length scales that appear in equation (3.20) and (3.21) are computed from

$$l_\mu = c_l y \left[1 - \exp\left(-\frac{Re_y}{A_\mu} \right) \right] \tag{3.22}$$

23

$$l_\varepsilon = c_l y \left[1 - \exp\left(-\frac{\mathrm{Re}_y}{A_\varepsilon} \right) \right] \qquad\qquad (3.23)$$

The constant in the length scale formulas, equation (3.22) and (3.23), are taken from Chen and Patel [28]:

$$c_l = kC_\mu^{-3/4}, \; A_\mu = 70, \; A_\varepsilon = 2c_l$$
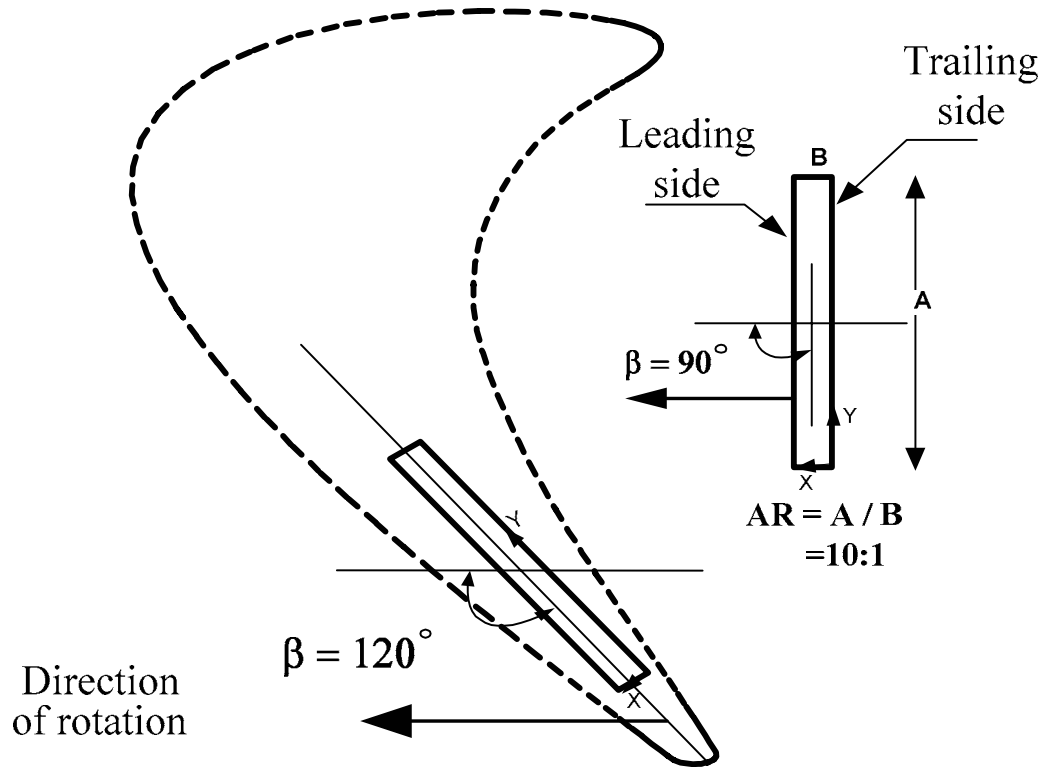
Figure 3.1: Location of the tilted cooling channel in a turbine blade.
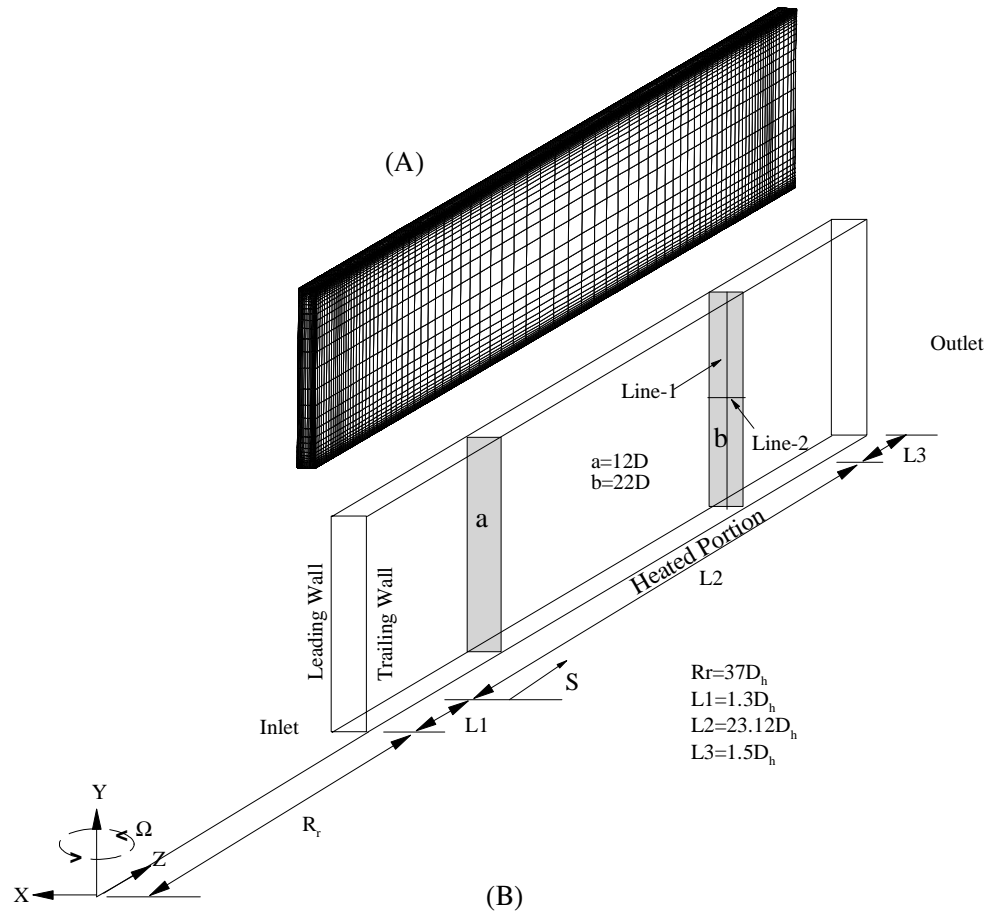
Figure 3.2: Rectangular channel aspect ratio (AR) 10:1: A, Computational grid; B, Geometry.

Coriolis force

Heating

Inlet

Outlet

No Coriolis Force
No Buoyancy Force

Heating

Coriolis force

Heating

Inlet

Outlet

With Coriolis Force
No Buoyancy Force

Heating

Coriolis force

Heating

Inlet

Outlet

Bouyancy Force

Heating

With Coriolis & Buoyancy Force

Velocity Profiles
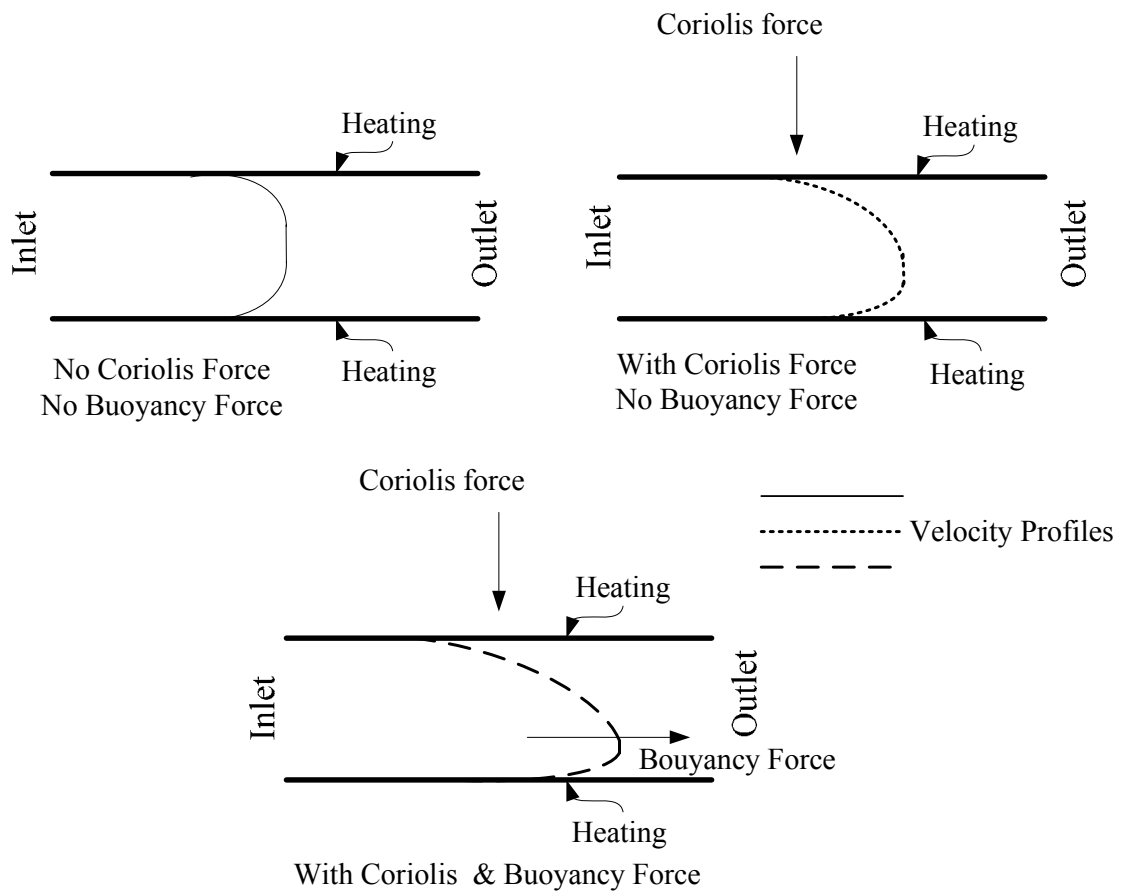
Figure 3.3: Forces acting in a rotating channel.
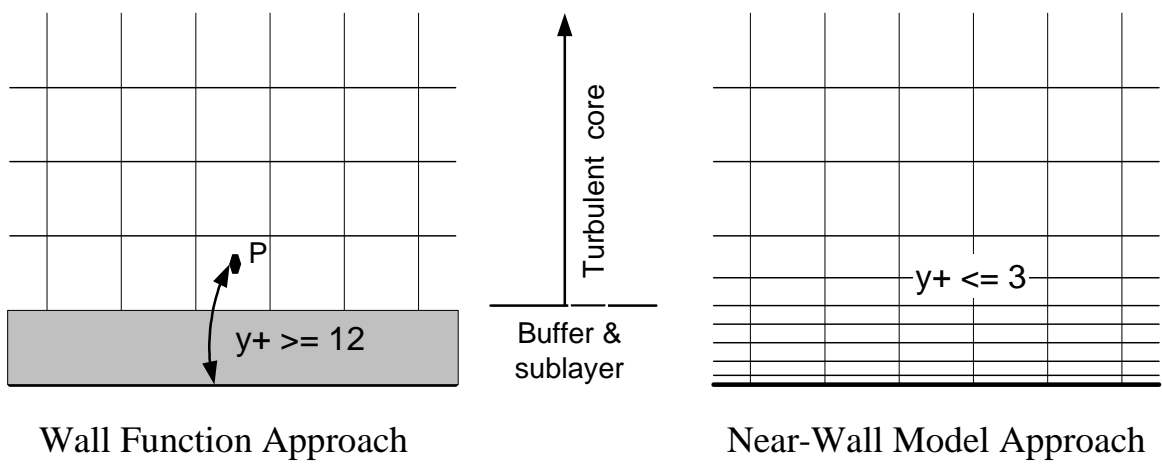
Figure 3.4: Mesh for wall-function and two-layer model [28].

CHAPTER 4

COMPUTATIONAL ASPECTS AND VALIDATION

4.1. Method of solution

The particular practice that will be chosen here for the derivation of the discretization equations is the control volume approach. The calculation domain is divided into sub-domains or control volumes such that there is one control volume around a grid point. The differential equation is integrated over this control volume to yield the discretization equations. Thus, the discretization equation represents the same conservation principle over a finite region as the differential equation does over an infinitesimal region [29&30]. This direct interpretation of the discretization equation makes the method easy to understand in physical terms; the coefficients in the equation can be identified, even when they appear in a computer program, as familiar quantities such as flow rates, conductance, areas, volumes, diffusivities, etc.

4.2. Computational grid details

The grid was generated iteratively using gambit software. Figure 3.2A shows the computational grid for the smooth duct. The pin fin case is discussed in detail in chapter 6. The block was divided into three zones, to have better distribution of nodes in the critical regions. Reynolds stress model in conjunction with two-layer approach is used. The minimum grid spacing (first node from the wall) in the near-wall region is maintained at reasonable distance, which corresponds to a wall coordinate y^+ of the order

of 1. The number of grid points in the stream wise direction from inlet to outlet is 88 while in the cross-stream plane is 41×61. The grid was made dense in the region of high gradients, such as at the near-walls, inlet and at the two junctions of heated and unheated section in order to obtain accurate results. The number of grid points and their distribution in the present smooth duct were obtained based on grid-refinement test, which is elaborated in the next section. Convergence criteria were set to 10^{-5} for all the flow variables.

4.3. Boundary conditions

For smooth channel at the inlet (z = 0), a uniform velocity profile will be used for the w-component while the u, v-components, k and ε were all assumed to be zero. Reynolds stresses are assumed to be isotropic at the inlet, Normal stresses $\overline{u'u'}$, $\overline{v'v'}$ and $\overline{w'w'}$ are set to 1, and $\overline{u'v'}$, $\overline{u'w'}$, $\overline{v'w'}$ are set to zero, [28]. Since we are using ideal gas law to incorporate the density variation with temperature, the code does not permit to use zero-gradient boundary conditions for the flow variables at the exit of the channel. The buoyancy effect is expected to be significant at high rotation number, Ro, and high density ratio, $\Delta\rho/\rho$, so, we may expect some flow reversal to occur near the outlet of the channel. Due to this reason pressure is fixed to atmospheric pressure at the exit. Reynolds number based on channel hydraulic diameter is fixed to 30000. At the walls, the no-slip condition is used. The coolant fluid at the inlet of the channel is at uniform temperature T = T_i. The top and bottom walls are unheated and thermally insulated in the experiment of Willett and Bergles [11 & 12] so they were modeled with zero heat flux boundary condition. The leading and trailing walls are modeled with constant heat flux in one case

(Chapter 5) similar to Willett and Bergles [11&12]. In a further study, the leading and trailing walls are kept at constant surface temperature (Chapter 6).

4.4. Physical properties

To validate the present results, the geometry and physical properties are chosen similar to those used in the experiment of Willett and Bergles [11&12]. The physical properties of R134a are used, and the density variation with temperature is obtained using ideal gas law for both, smooth and pin-finned channel.

$$\text{i,e} \qquad \rho = P/RT \qquad\qquad (4.1)$$

Where T, P, and R are local temperature, local pressure, and gas constant respectively.

$\mu = 1.1879 \times 10^{-5}$ kg/m-s. k = 0.013538 W/m-K and $C_p = 854$ kJ/kg-K.

Coolant-to-wall density ratio is defined as

$$\Delta\rho \Big/ \rho = \frac{\rho_i - \rho_w}{\rho_i}$$

where ρ_i & ρ_w are density of the coolant at the inlet and at the wall, respectively.

Using equation (4.1) the above equation can be written as

$$\Delta\rho \Big/ \rho = \frac{\frac{1}{T_i} - \frac{1}{T_W}}{\frac{1}{T_i}} = \frac{T_W - T_i}{T_w} \qquad\qquad (4.2)$$

4.5 Assumptions

- Flow and heat transfer are assumed to be steady.

- Ideal gas law is used to calculate density variation with temperature.

- The cooling channel in the leading edge is assumed to have narrow rectangular cross-section with aspect ratio (10:1).

- Uniform distribution of temperature/heat flux on walls is assumed.

- Reynolds stresses are assumed to be isotropic at the inlet.

- Uniform velocity profile at the inlet ($z = 0$) is assumed.

4.6. Grid independency test

To choose a suitable computational grid, a grid independence test must be performed, to ensure grid independence; the solutions were computed using different grid sizes. The tested grid size are 31×51×88, 41×61×88, and 57×71×88. From now onwards, these grids will be referred to as Grid-1, Grid-2, and Grid-3 respectively. The parameters used to check the grid independency are axial velocity, temperature, and Nusselt number. Comparisons of the various parameters are shown in Figure 4.1 through Figure 4.3 and values of average Nusselt number are tabulated in Table 4.1. It can be seen from Figure 4.1a and Figure 4.2a that the velocity profile obtained from the all the grids are overlapping, and in Figure 4.1b, Figure 4.1b the temperature profile obtained from Grid-2 and Grid-3 are almost same, and span wise averaged Nusselt number ratio obtained from above grids are shown in Figure 4.3. Table 4.1 depicts the percentage changes in the average Nusselt number on both leading and trailing wall for different grids. Percentage difference in averaged Nusselt number on leading wall is about 0.16 % from Grid-2 to Grid-3 and on trailing wall it is about 0.725 % from Grid-2 to Grid-3 at Rotation number, $Ro = 0.056$ and density ratio, $\Delta\rho/\rho$ of 0.07.

From the above set of observations, it is concluded that the accuracy of the solution on Grid-2 (41×61×88) is deemed to be satisfactory for the sake of presentation and better visualization of the flow parameters. To check the Grid sensitivity in stream wise direction, 16 nodes were increased in z-direction, and simulation was performed, but no appreciable difference in Nusselt number was found. The corresponding Cpu time on Zeon 3.06 Ghz/2Gb ram computer is about 16 hours for convergence, and typically it takes 1508 iterations to reach convergence. Detailed information about computations time, memory used and iteration for each grid is shown in Table 4.2. Because of limitation in computing facility, grid independency test is not performed for pin-fin case.
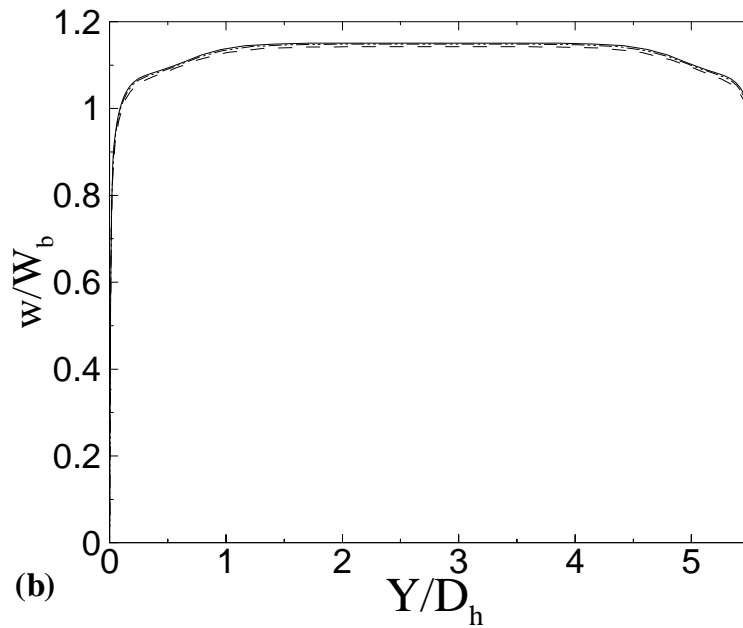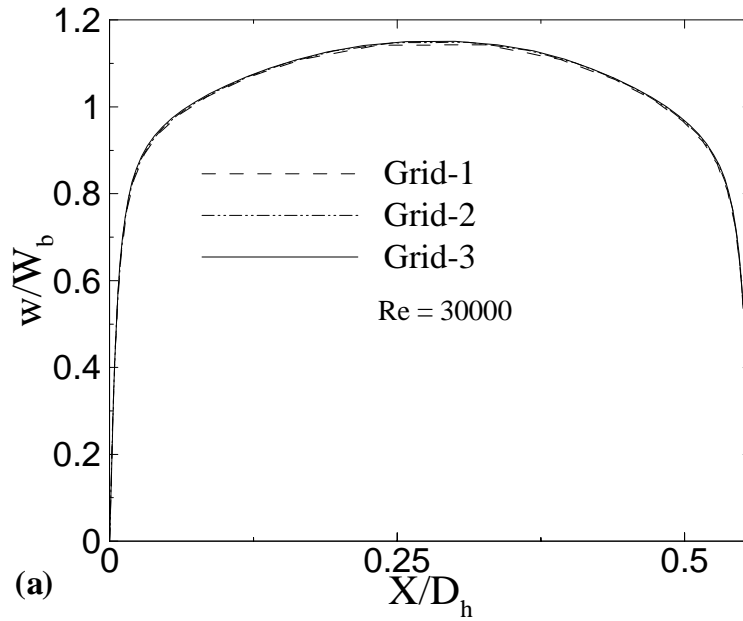
Figure 4.1: Comparison of dimensionless velocity [w/W_b] for different grids at $Z/D_h = 22$. $Ro = 0.056$ and $\Delta\rho/\rho = 0.07$: (a) $X/D_h = 0.56$; (b) $Y/D_h = 5.56$.
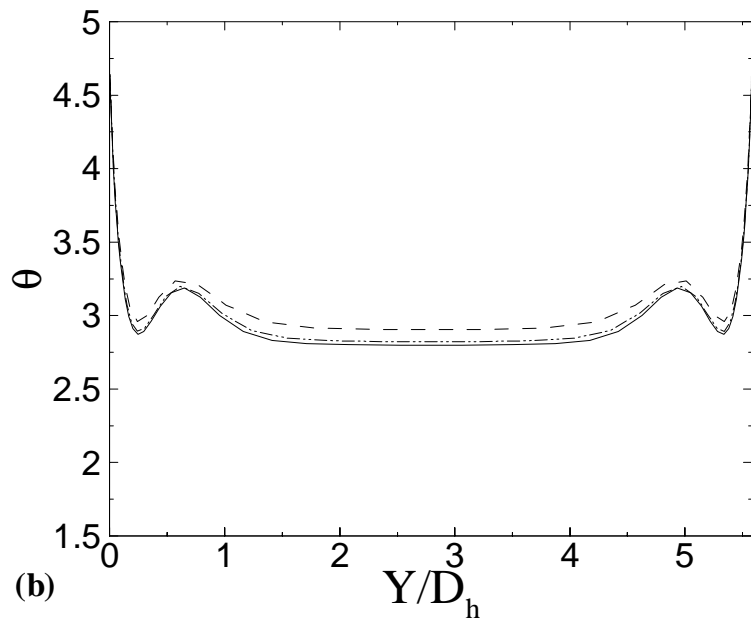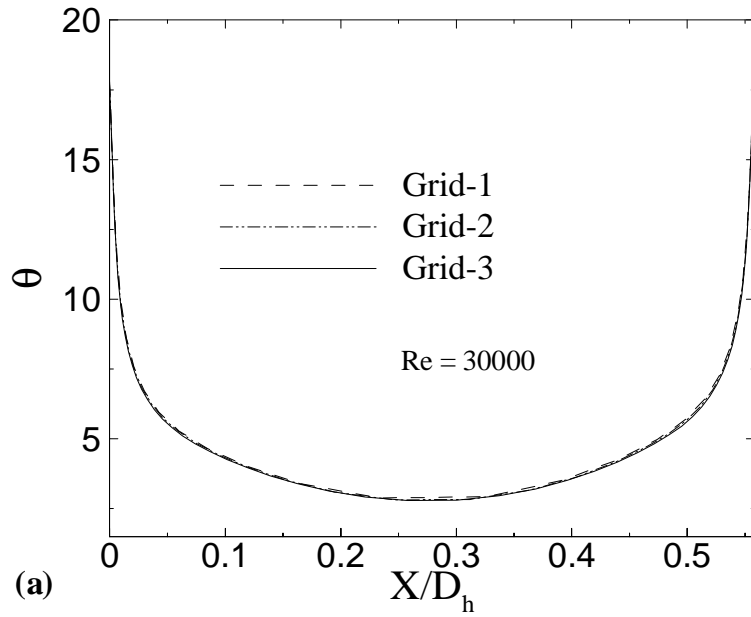
Figure 4.2: Comparison of dimensionless temperature [$\theta = (T-Ti)/(q/ (\rho\ Cp\ uf))$] for different grids at $Z/D_h = 22$. Ro = 0.056 and $\Delta\rho/\rho = 0.07$: (a) $X/D_h = 0.56$; (b`) $Y/D_h = 5.56$.
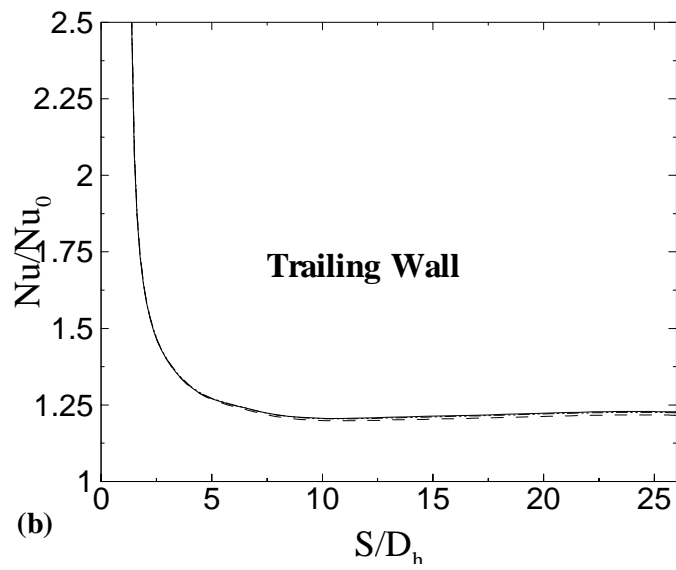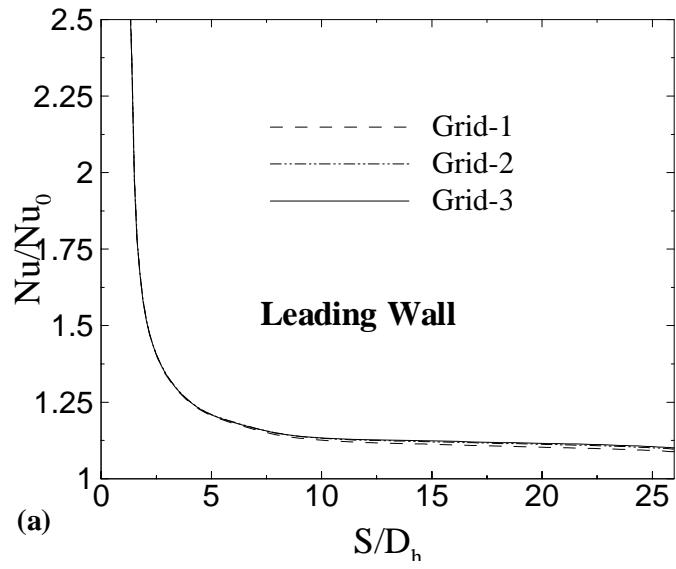
Figure 4.3: Span wise averaged Nusselt number for different grids, Ro = 0.056, Re = 30000 and $\Delta\rho/\rho = 0.07$: (a) leading wall; (b) trailing wall.

Table 4.1: Grid independency test, Re = 30000, Ro = 0.056 and $\Delta\rho/\rho$ = 0.07

Grid	Global Averaged Nusselt number		Percentage error
	Leading wall	Trailing wall	
Grid-1	1.156	1.2181	0.725 %
Grid-2	1.162	1.225	0.16 %
Grid-3	1.165	1.227	------

Table 4.2: CPU time for different grids, Re = 30000, Ro = 0.056 and $\Delta\rho/\rho$ = 0.07

	Grid-1	Grid-2	Grid-3
CPU time (Hours)	10	16	22
Memory used (Mb)	252.108	350.108	674
Iteration to converge	729	1508	2542

4.7. Validation

4.7.1. Normalizing the temperature field

This section highlights some of critical problem faced during the process of solving the mentioned cases in the Table 5.1. Results and discussions are presented in brief and based on these results suitable changes were brought in this research. Computational cases are summarized in Table 5.1. Reynolds number based on channel hydraulic diameter is kept constant, and equals 30000. Rotation number, Ro, and density ratio, $\Delta\rho/\rho$, in computation were varied from 0 to 0.25 and 0.1 to 0.4 respectively, for two channel orientation of $\beta = 90^o$ and 120°. All computations presented here were obtained by starting with the stationary case and then gradually increasing the rotation speed. The effect of rotation, Ro, density ratio, $\Delta\rho/\rho$, and channel orientation on flow field is discussed first, followed by heat transfer result. Flow field is represented in the form of relative velocity vectors. When constant surface temperature is the boundary condition in internal flow problems, temperature fields are normalized using the reference temperature, as the following,

$$\theta = (T\text{-}T_{ref})/(T_w\text{-}T_{ref}) \tag{4.3a}$$

where T_w is the wall temperature and it is a constant. T_{ref} is chosen to be the inlet temperature T_i, and when constant surface heat flux is the boundary condition the normalized temperature takes the following form,

$$\theta = \frac{T\text{-}T_i}{\dot{q}/(\rho\,C_p\,u_f)} \tag{4.3b}$$

where $\dot{q}$, ρ, C_p, and u_f are the constant surface heat flux, density, specific heat and friction velocity, respectively.

Nusselt number is normalized using Nusselt number for fully developed turbulent flow in smooth circular tube correlated by Dittus and Boelter/McAdams as mentioned in [11].

$$Nu_o = 0.023\text{Re}^{0.8}\,\text{Pr}^{0.4} \hspace{4cm} (4.4)$$

4.7.2. Selection of near wall treatment

Grid independency analysis was carried out using two-layer model as near wall treatment to the computational domain, but one would like to optimize the computing resources by choosing wall function as near wall treatment to compute the solution. To justify the use of two-layer model as near wall treatment, simulations were carried out on stationary (Ro = 0.0 and $\Delta\rho/\rho$ = 0.07) and rotating channel (Ro = 0.056 and $\Delta\rho/\rho$ = 0.07) applying both wall-function and two-layer model, and results are compared for each case.

To apply wall function and two-layer model as near wall treatment, two computational domains were created. First computational domain was meshed such that the first grid point lies well above the viscous and buffer layer, which corresponds to y+ of 30. While second computational domain mesh is refined to a level of y+ of 1, which is close enough to wall to predict the near wall region. Both computational domain has equal number of nodes, i.e., number of grid points in x, y and z direction is fixed to 41×61×88, which was obtained from the grid independency test.

Since the problem is symmetric about the x-axis, results are presented for top-half cross section of the channel, and the results presented here are viewed from the upstream of the flow. Figure 4.4 shows the non-rotating secondary flow at a distance of 12 hydraulic diameters from the inlet of channel for wall function and two-layer model. It can be seen

in figure 4.4a, that the secondary flow is well established with four vertices close to the corners of the channel, and it represents a typical secondary flow pattern for stationary channel. In figure 4.4b similarly secondary flow pattern is observed but the strength of the secondary flow is less when compared with the secondary flow obtained using two-layer model (Figure 4.4a).

Now, consider figure 4.5, which shows calculated secondary flow and dimensionless temperature contours for the top half of the rotating channel at $Z/D_h = 22$. It is evident from the figure 4.5a that, a well established vortex pushes the cold fluid from the core region to trailing wall side, and to the top wall and then to leading wall and back to core region of the channel. This is due to Coriolis force that is acting on the system because of system rotation. Coriolis force being one of the forces that tends the flow and heat transfer characters in rotating channel to be very different from the one in stationary channel. This phenomenon of mixing is not seen in figure 4.5b. Since the flow and heat transfer are coupled and most of the turbulent activities occurs close to the wall, it is obvious that, better the approximation of the flow variables in the near wall region, higher is the solution accuracy. To qualify the above discussions consider the corresponding dimensionless temperature plots in figure 4.4a and figure 4.4b. From these figures it is apparent that there is an appreciable difference in temperature field. Resulting Nusselt numbers profiles by using wall function and two-layer model for the stationary (Ro = 0.0) and rotating (Ro = 0.056) channel is shown in Figure 4.6 and Figure 4.7, respectively. It is seen in literature [12-25] that for stationary channel the Nusselt number ratio in fully developed region is higher than unity. The Nusselt number ratio obtained by two-layer model is seen to have value of 1.1 in fully developed region. Again for rotating

channel the Nusselt number ratio obtained by the two-layer model are seem to be reasonable accurate, showing Nusselt number ratio higher than unity for both leading and trailing wall. While Nusselt number ratio obtained using wall-function approach for both stationary (Ro = 0.0) and rotating (Ro = 0.056) channel is very low, which is incorrect. It is evident from the above set of observation that the wall-function approach is much less accurate compared to the two-layer approach. It can be concluded that use of wall function to would lead to under prediction of heat transfer in stationary as well as rotating channel. Hence two-layer model is used as near wall treatment to predict heat transfer for various cases mention in Table 5.1.
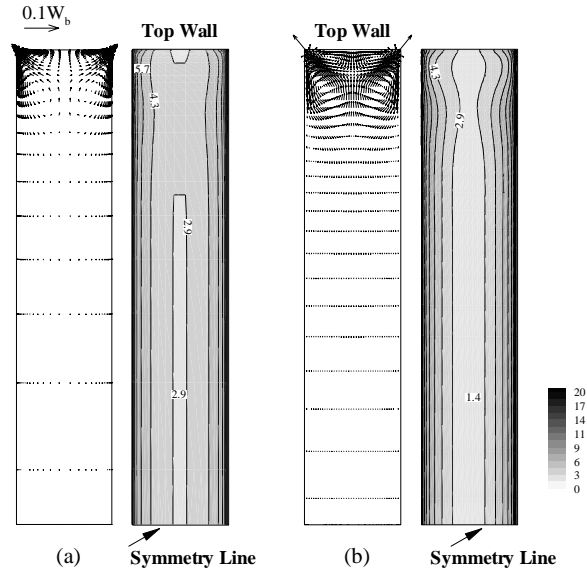
Figure 4.4: Secondary velocity vectors and dimensional temperature [θ = (T-Ti)/ (q/ (ρ Cp uf))] contours of top half cross-section at Z/D$_h$ = 22. Ro = 0.0, Re = 30000 and Δρ/ρ = 0.07: (a) Two-layer; (b) Wall function.
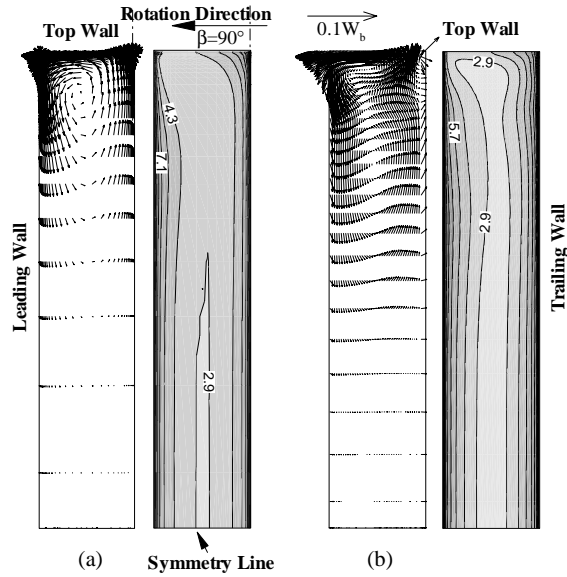
Figure 4.5: Secondary velocity vectors and dimensional temperature [θ = (T-T$_i$)/(q/ (ρ C$_p$ u$_f$))] contours of top half cross-section at Z/D$_h$ = 22. Ro = 0.056, Re = 30000 and Δρ/ρ = 0.07: (a) Two-layer; (b) Wall function.

42

(a)

(b)
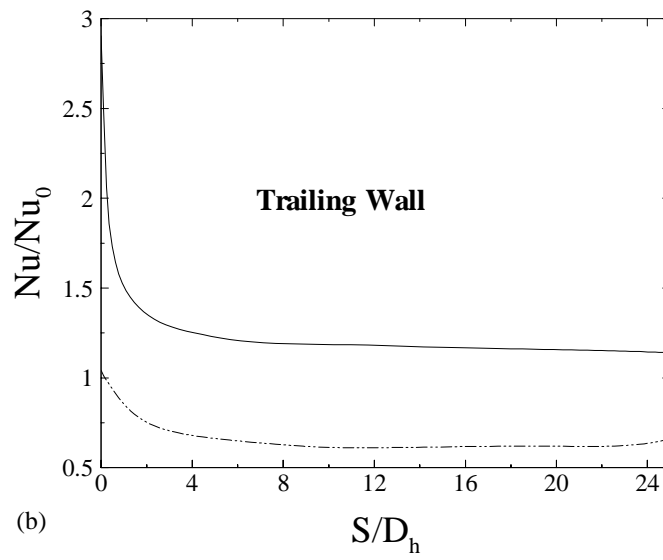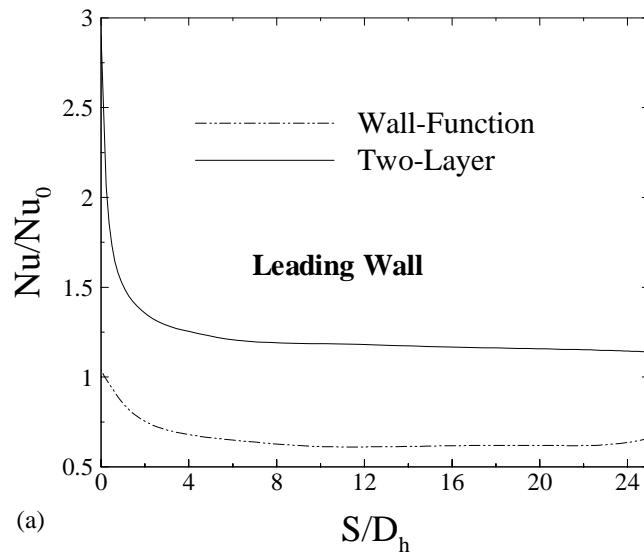
Figure 4.6: Spanwise averaged Nusselt number along the duct length. Re 30000, Ro = 0.0 and $\Delta\rho/\rho = 0.07$.
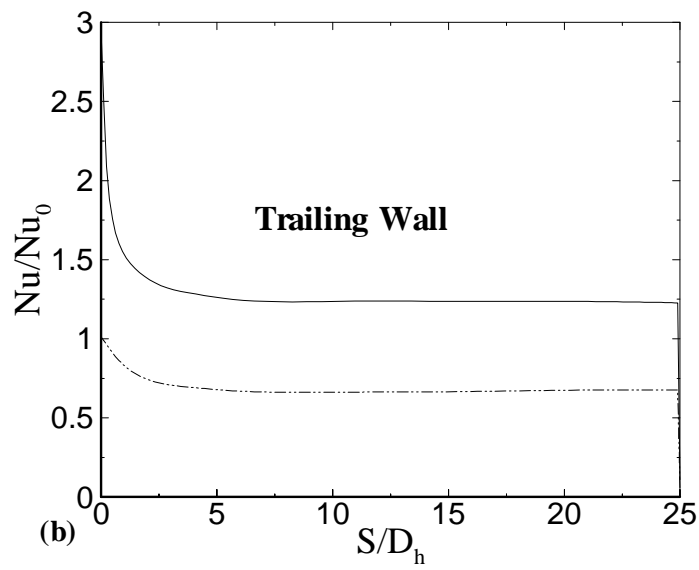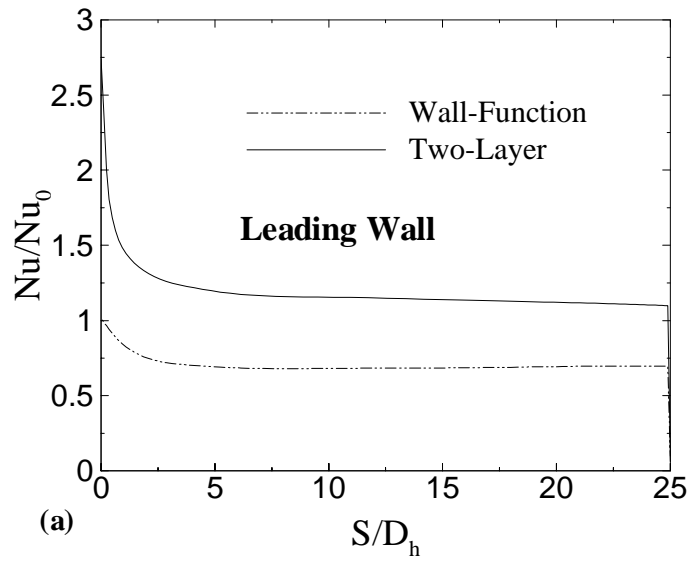
Figure 4.7: Spanwise averaged Nusselt number along the duct length. Re 30000, Ro = 0.056 and $\Delta\rho/\rho = 0.07$: (a) Leading wall; (b) Trailing wall.

4.7.3. A first validation of the computational model

Before simulating the actual cases, simulation were carried out on few cases (Ro = 0.14 and 0.28) of Al-Qahtani et al. [27], to validate the results of two-layer model. In Al-Qahtani et al. [27], solution was obtained for various rotation numbers, Ro, and density ratios, $\Delta\rho/\rho$, and fixing Reynolds number to 10000. The problem was solved by employing chimeras Reynolds averaged Navier-Stokes turbulent method of Chen et al. Figure 4.8 compares the calculated secondary velocity and temperature contours obtained by Al-Qahtani et al. [27] with corresponding results of present study, for various for above mentioned cases at location of Z/D_h = 16.24. It is seen that the calculated secondary flow and dimensionless temperature field for low rotation number, Ro and density ratio, $\Delta\rho/\rho$, are closely matching with corresponding results in the Al-Qahtani et al. [27], And slight difference in calculated secondary flow and dimensionless temperature contours is observed for high rotation number, Ro, and density ratio, $\Delta\rho/\rho$. This difference can be attributed to two facts (1) that in the Al-Qahtani et al. [27], the density was held constant, except in the centrifugal buoyancy term where density was modeled using Bossinesq approximation. (2) The exit boundary condition in Al-Qahtani et al. [27] was set to zero gradient, while in the present study it is pressure outlet.

Local Nusselt number distribution on leading wall for rotation number, Ro = 0.14 and density ratio, $\Delta\rho/\rho$ = 0.12 is shown in Figure 4.9. Again here we can see that the local Nusselt number distribution is almost similar in pattern, but the magnitude of Nusselt number is higher at the entrance region when compared with the corresponding result obtained by Al-Qahtani et al. [27].

Figure 4.10a and Figure 4.10b, show the calculated span wise averaged Nusselt for rotating channel. It can be seen that the Nusselt number is higher on trailing wall and lower on leading wall for any given set of rotation number, Ro, and density ratio, $\Delta\rho/\rho$. As the density ratio, $\Delta\rho/\rho$ is increased from 0.12 to 0.2, the Nusselt number on trailing wall increases almost asymptotically, while on the leading wall, Nusselt number decreases in the region close to inlet region and increases in the down stream of the channel. This kind of behavior can also be observed in Al-Qahtani et al. [27] (Figure 5.7).
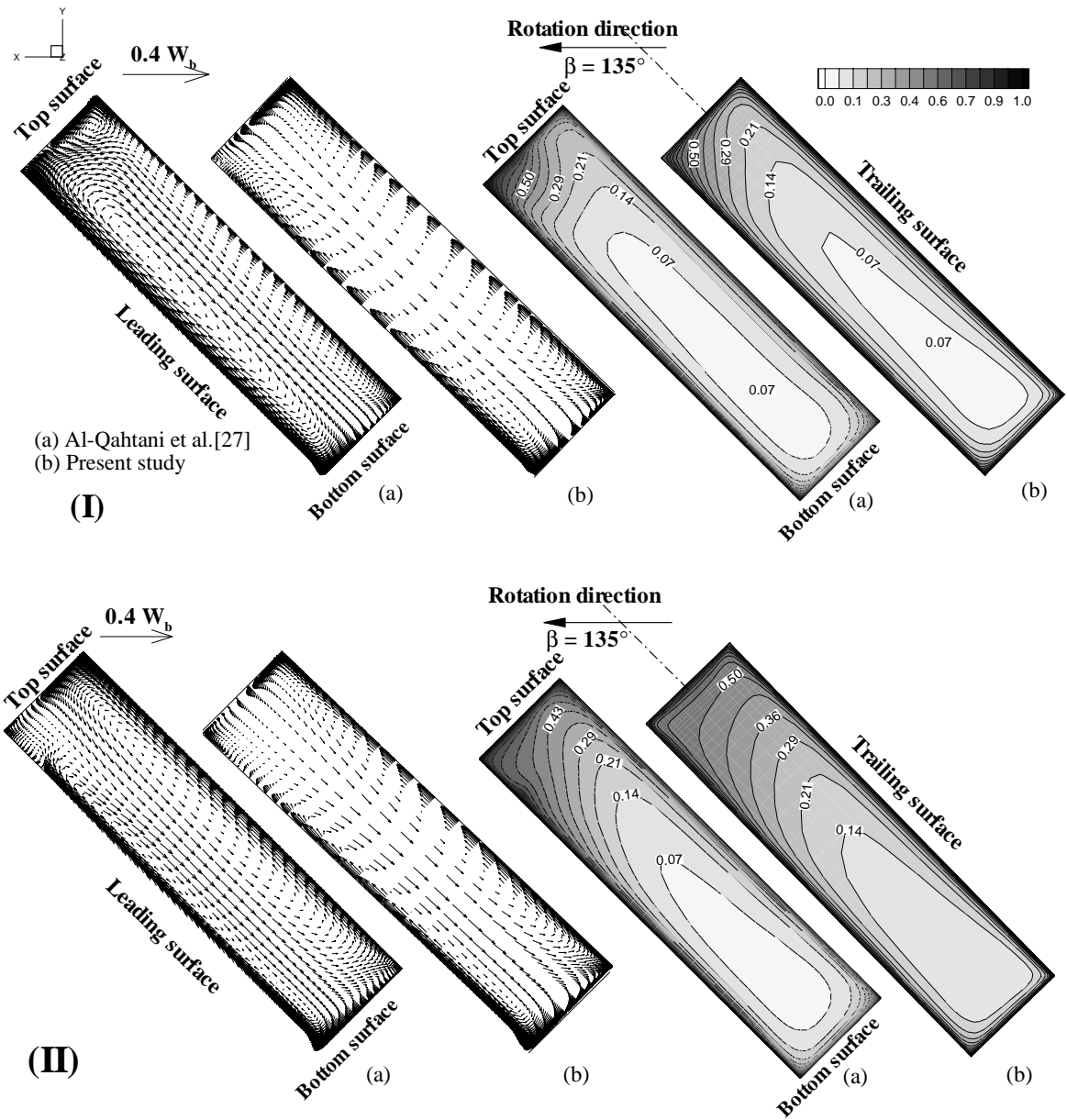
Figure 4.8: Secondary velocity vectors and dimensionless temperature [$\theta = (T-T_i)/(T_w-T_i)$] for $\beta = 135^o$: (I) Ro = 0.14, $\Delta\rho/\rho = 0.12$ and (II) Ro = 0.28, $\Delta\rho/\rho = 0.12$.
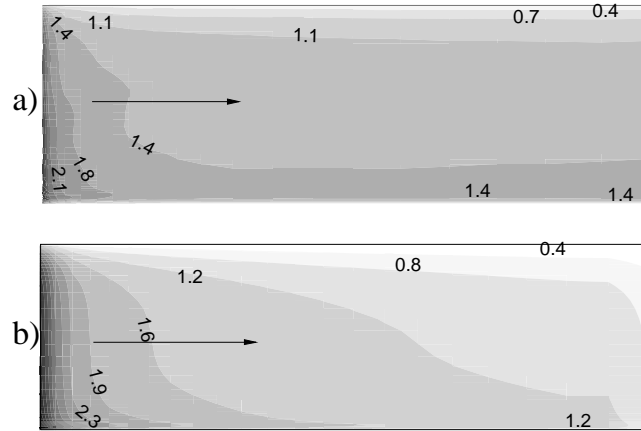
Figure 4.9: Local Nusselt number distribution on leading surface. Ro = 0.14, $\Delta\rho/\rho$ = 0.12 & β = 135°: (a) Qahtani et al. [27]; (b) Present study.
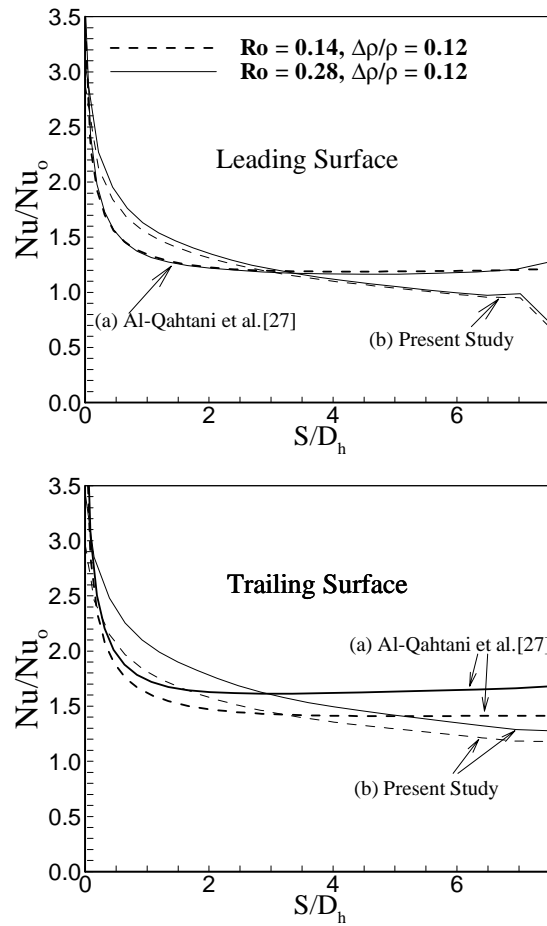
Figure 4.10: Comparison of Span wise averaged Nusselt number (for β = 135°. AR = 4:1 and Re = 10000) with Al-Qahtani et al. [27].

4.7.4. Nusselt number definition for high rotation number and density ratio

This section highlights the non-physical behavior for Nusselt number in the case of high rotation number, Ro, and high density ratio, Δρ/ρ <u>for constant heat flux boundary condition.</u> Figure 4.11 shows the Nusselt number ratio on leading and trailing wall respectively, for three density ratio, Δρ/ρ = 0.1, 0.2 and 0.3, and rotation number, Ro=0.125. Nusselt number profile obtained for density ratio, Δρ/ρ = 0.1 and 0.2 are decreasing asymptotically downstream which represents typical Nusselt number profile for similar problem. When density ratio, Δρ/ρ is increased to 0.3, while keeping the same rotation number, Ro, Nusselt number increases dramatically on both leading and trailing wall. And when rotation number, Ro, is increased to 0.25, even for low density ratio, the fluctuations in Nusselt number is observed on both the leading and trailing wall, which can be seen in Figure 4.12. These fluctuations in Nusselt number seem to increase with increase in density ratio, Δρ/ρ. The above fluctuations in Nusselt number could be due to following possible reasons:

- Coarse grid in the interior regions of the heated walls.

- Over Relaxation.

- Nusselt number definition.

Considering the first possible reason, the computational domain is refined in the interior regions of heated walls and this resulted in grid size of 41×61×105 in x, y and z direction respectively. Without making any rush to obtain the solution for high rotation number, computation is started with low rotational speed and then rotation speed is increased gradually to reach the required high rotation number. Figure 4.13 shows the Nusselt number on leading and trailing wall for refined computational domain. It is

apparent from the figure that there is still fluctuation in Nusselt number, even at rotation number, Ro= 0.15 and density ratio, Δρ/ρ = 0.15. Therefore, one can conclude that these fluctuations are not due to coarse grid.

To check whether, this problem of fluctuations is due to over relaxing the solution parameters, computation were carried out reducing relaxation factors gradually to the lowest possible. It was found that the fluctuation still persists.

Next, the boundary condition was changed from constant heat flux to constant surface temperature. Computations were performed for high rotation number, Ro = 0.25 and various density ratios, Δρ/ρ = 0.1, 0.2 and 0.4 and results are shown in Figure 4.14. One can observe in this figure that the Nusselt number profiles are smooth for both leading and trailing walls. Therefore, we concluded that these fluctuations are only due to nature of thermal boundary condition. This can be explained as follows. Since wall temperature is constant (in the Figure 4.14) and the fluid temperature in the channel is always less than the wall temperature, the denominator in equation (4.5) is always positive.

For the case of constant surface heat flux, the problem seems to be in the definition of Nusselt number. The present definition of Nusselt number is given below.

$$Nu = \frac{D_h}{\left(T_w - T_b\right)} \frac{\partial T}{\partial x}\bigg|_{x=0} \qquad (4.5)$$

where T_b is the bulk temperature.

To support this fact, consider Figure 4.15 and Figure 4.16, showing the temperature on leading wall and bulk temperature in the heated section of the channel for rotation

number, Ro = 0.25 and density ratio, $\Delta\rho/\rho = 0.2$, respectively. When we closely look at the wall temperature of the section highlighted in Figure 4.15, and bulk temperature in corresponding region of Figure 4.16. We see that the wall temperature is lower (or closer in value) than the bulk temperature. Due to this, the Nusselt number seems to have either high value when T_b and T_w are very close to each other or has negative value when T_b is greater than the wall temperature. In experiments, these phenomena cannot be observed, because there is always span-wise heat transfer conduction taking place in the heaters.

The solution to this problem is to change the definition of the Nusselt number by replacing bulk temperature with inlet temperature.

$$Nu = \frac{D_h}{(T_w - T_i)} \frac{\partial T}{\partial x}\bigg|_{x=0} \tag{4.6}$$

where T_i is the inlet temperature.
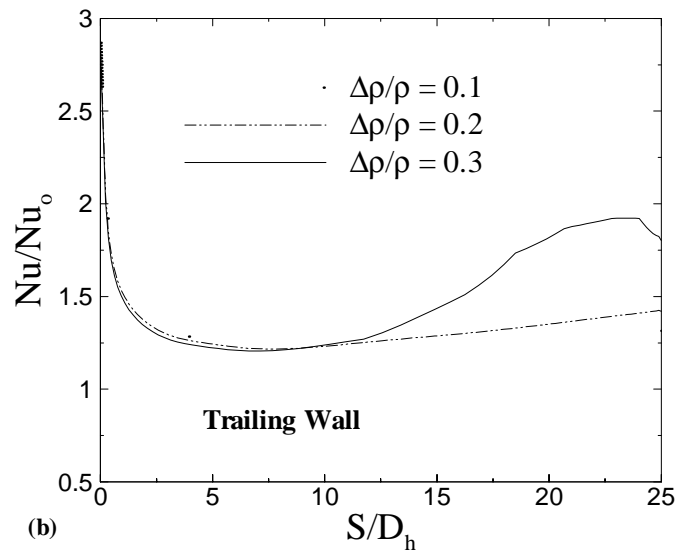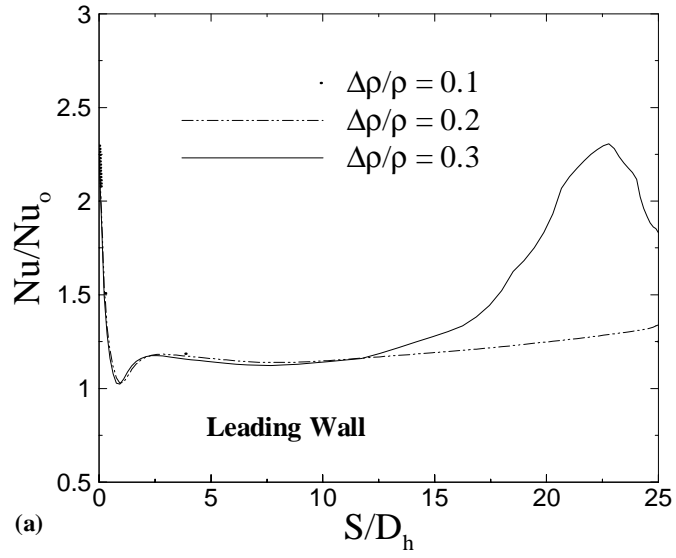
Figure 4.11: Trails for spanwise averaged Nusselt number. Re = 30000, Ro = 0.125, β = 120^0: (a) leading wall; (b) trailing wall.
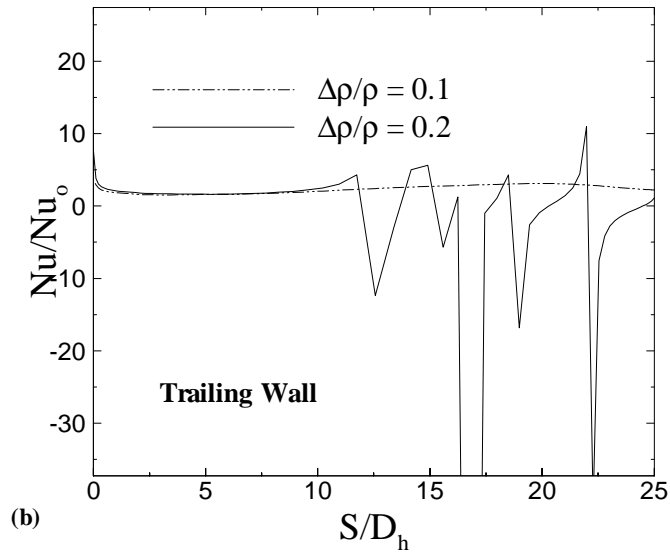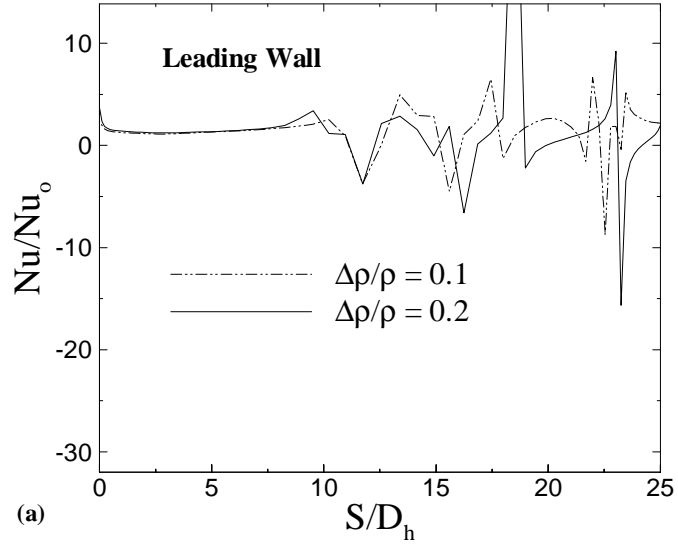
Figure 4.12: Trails for spanwise averaged Nusselt number. Re = 30000, Ro = 0.25, β = 120° and Δρ/ρ = 0.1: a) leading wall; b) trailing wall.
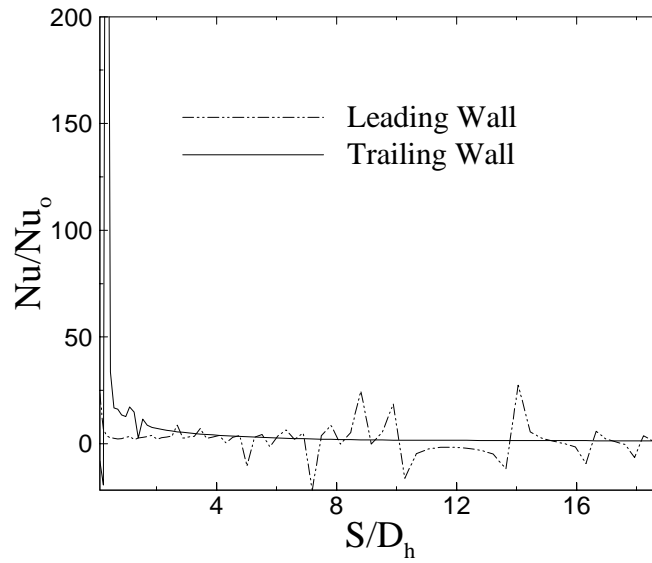
Figure 4.13: Trails for spanwise averaged Nusselt number (mesh size of 41×61×105). Re = 30000, $\beta = 120^0$, Ro = 0.18 and $\Delta\rho/\rho = 0.15$.
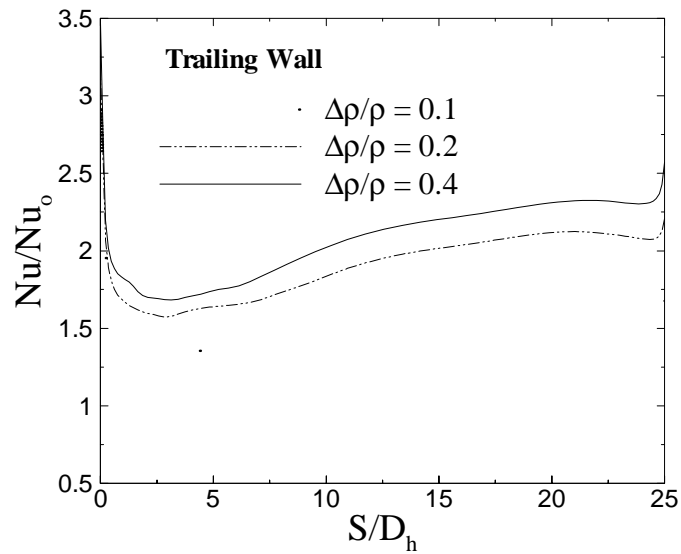
Figure 4.14: Spanwise averaged Nusselt number (for constant wall temperature) on Trailing Wall. Re = 30000, $\beta = 120^0$, Ro = 0.25.
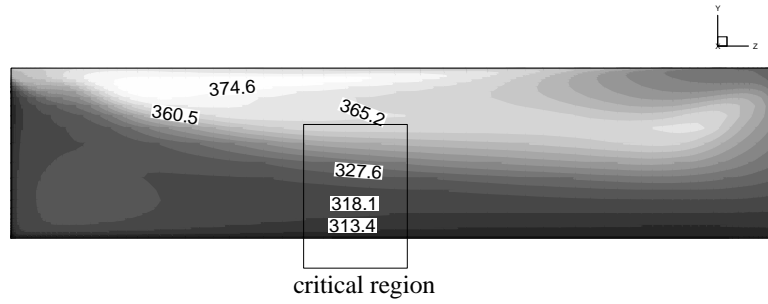
Figure 4.15: Temperature field on leading wall. Re = 30000, Ro = 0.25 and Δρ/ρ = 0.1.
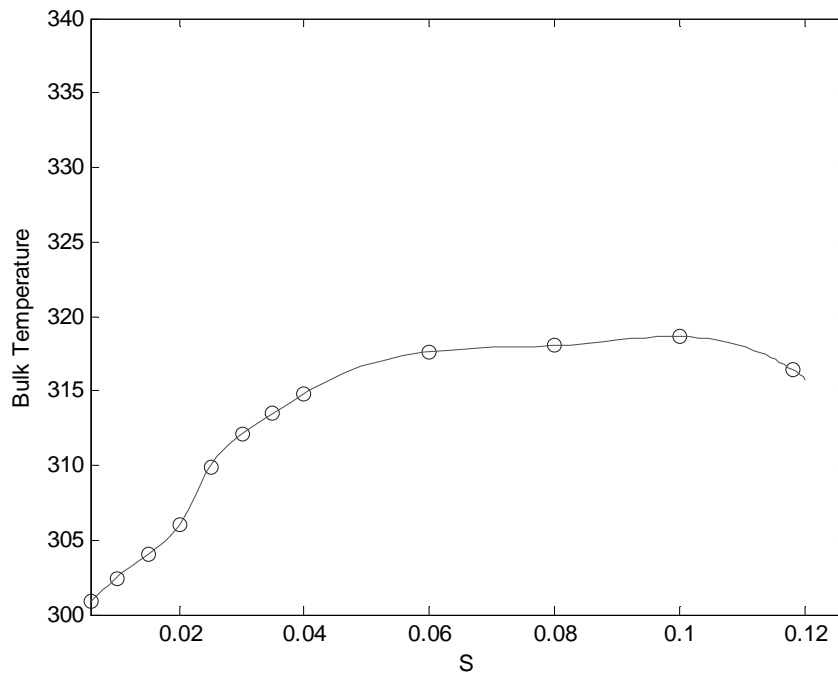
Figure 4.16: Bulk Temperature along the channel heated section. Re = 30000, Ro = 0.25 and Δρ/ρ = 0.1.

CHAPTER 5

CONSTANT HEAT FLUX BOUNDARY CONDITION

5.1. Introduction

This chapter presents results and discussion for smooth channels with leading and trailing walls being held at constant surface heat flux while the top and bottom walls are kept adiabatic. Computational cases are summarized in Table 5.1. Reynolds number based on channel hydraulic diameter is kept constant, and equals 30000. Rotation number, Ro, and density ratio, $\Delta\rho/\rho$, in computation were varied from 0 to 0.125 and 0.1 to 0.2 respectively, for two channel orientations of $\beta = 90^o$ and 120°. All computations presented here were obtained by starting with the stationary case and then gradually increasing the rotation speed.

The effect of rotation, Ro, density ratio $\Delta\rho/\rho$, and channel orientation on flow field is discussed first, followed by heat transfer results. Flow field is represented in the form of relative velocity vectors. Dimensionless temperature is defined as in equation (4.3b), and Nusselt number is defined as in equation (4.5). Nusselt number is normalized using equation (4.4).

5.2. Conceptual view

Figure 5.1 shows a conceptual view of the secondary flow induced by channel rotation. For the 90° channel orientation, the Coriolis force produces two counter-rotating vortices that push the cooler fluid from the core region to the trailing wall. When the domain is

tilted to 120° from the direction of rotation, the Coriolis force produces two long vortices parallel to leading and trailing wall, and third vertex is set at the top corner of the trailing wall.
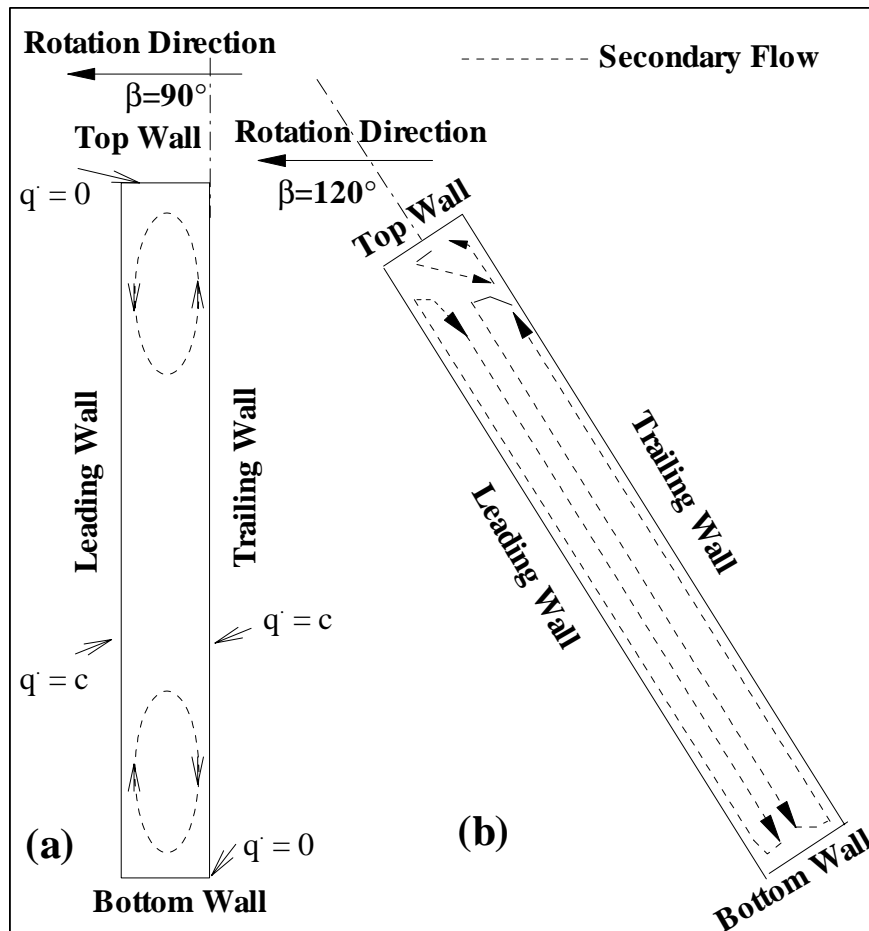
Figure 5.1: Conceptual view of the secondary flow induced by rotation: (a) $\beta = 90^{\circ}$; (b) $\beta = 120^{\circ}$.

Table 5.1: Computational cases for constant heat flux boundary condition

Case	Rotation Number, Ro	Density Ratio, $\Delta\rho/\rho$	β
1	0.0	0.1	--
2	0.125	0.1	90°
3	0.125	0.2	90°
4	0.125	0.4	90°
5	0.125	0.1	120°
6	0.125	0.2	120°

5.3. Velocity and temperature fields

It is worth to mention in the beginning of the discussion that the results presented at axial locations are viewed from upstream of the channel. Since the channel has high aspect ratio, some plots are magnified at critical regions to have better visualization. Calculated secondary flow vectors and dimensionless temperature contours at two axial locations (Z/D_h = 12 and 22) for all the cases mentioned in Table 5.1 are presented in Figure 5.2 though Figure 5.7. Calculated secondary flow vectors and dimensionless temperature contours for stationary case (case 1) is shown in Figure 5.2. Four vortices at the corners are formed due to anisotropy in Reynolds stresses. From the corresponding dimensionless temperature contours it seen that cold fluid is located at core region of the channel. As we move on to downstream of the channel (Figure 5.2b), the secondary flow pattern is same but, the fluid is heated more in the core region of the channel.

Figure 5.3 shows computational secondary flow vectors and dimensionless temperature contours for the case 2. Coriolis force which arises due to system rotation, that pushes cold fluid from the core towards the trailing wall and then to top wall and bottom wall and then brings along leading wall back to core. This leads to formation of vortices in the regions close to top and bottom wall of the channel. The transport of relatively cooler, and hence heavier, fluid from the core region to the trailing wall results in steep temperature gradient (hence higher heat transfer) on the trailing wall. And fluid after receiving considerable amount of heat from the trailing wall sweeps along the leading wall and small temperature gradient (relatively low heat transfer) on leading wall, which can be seen in corresponding dimensionless temperature contours of Figure 5.3. It is worth noticing that the temperature gradient at the leading corners is high when

compared with temperature gradient at trailing corners, this is due to the fact that the top and bottom wall are unheated and some portion of cold fluid from core region is directly pushed to top and bottom wall and then to leading corners and hence high temperature gradient occur at these locations. Figure 5.4 and 5.5, shows the computed secondary flow-vectors and dimensionless temperature contours for case 3 and 4. It is seen that as the density ratio, $\Delta\rho/\rho$, is increased to 0.2 and 0.4 while fixing rotation number, Ro to 0.125. The secondary flow pattern seems to remain same. The dimensionless temperature contours remain almost unchanged.

Figure 5.6 shows the computed secondary flow vectors and dimensionless temperature contours for case 5. In this case the channel orientation angle, β equals 120^0. One can notice from figure 5.6, that Coriolis-induced secondary flow pushes the cold fluid away from the top leading corner to core region and then to bottom wall then it sweeps upwards along the leading and trailing walls. This action of Coriolis force sets two elongated counter rotating vortices near the leading and trailing wall. As mentioned before, that the cooler fluid sweeps along and upwards of the leading and trailing walls, and so it is expected that the velocity and thermal boundary layer is thin in lower portion of leading and trailing wall, and hence high temperature gradients occur, this is illustrated in corresponding dimensionless temperature contours of Figure 5.6. As density ratio, $\Delta\rho/\rho$ is increased to 0.2, the calculated secondary flow patterns at two axial locations remain unchanged (Figure 5.7), but the strength of secondary flow increases, especially in the core region of the channel, and also it is seen that the dimensionless temperature contour pattern remains same.

Now focus is turned on to stream wise flow and dimensionless temperature field for two cases, Figure 5.8 shows combined velocity vectors and dimensionless temperature contours midway between leading and trailing wall for the cases 5 and 6. In the above figure the unheated section is omitted to focus on heated section of the channel. The main intention to illustrate these plots is to highlight the effect of buoyancy on the flow field and hence heat transfer. Figure 5.8a shows calculated velocity vectors and dimensionless temperature contours for case of stationary channel (Ro = 0.125, β = 120° and $\Delta\rho/\rho$ = 0.1), the velocity vectors are thick at the bottom wall and thin at the top wall. This is because the relatively cold and heavier fluid at the bottom wall experience high buoyancy forces than the warm fluid at the top wall. As the density ratio, $\Delta\rho/\rho$, is increased to 0.2, while fixing the rotation number, Ro to 0.125, the buoyancy force is seem to increase the fluid velocity at the bottom wall in the downstream of the channel dramatically, and in order maintain continuity in the flow, hot and lighter fluid at the top wall decelerates and hence low velocity.
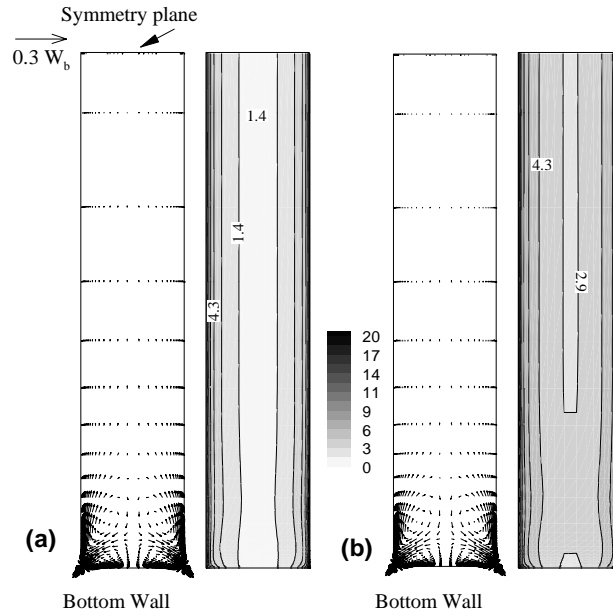
Figure 5.2: Secondary flow vectors and dimensionless temperature [$\theta = (T-T_i)/ (q/ (\rho\, C_p\, u_f))$]. Re = 30000, Ro = 0.0, and $\Delta\rho/\rho = 0.1$: (a) $Z/D_h = 12$; (b) $Z/D_h = 22$.
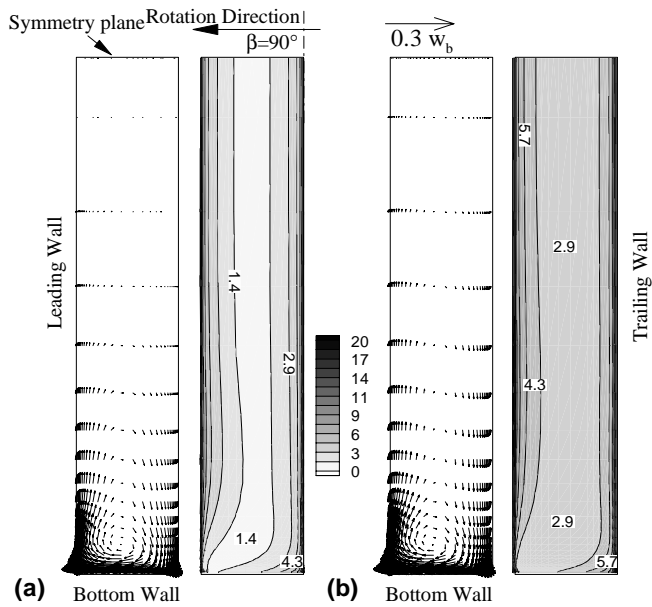
Figure 5.3: Secondary flow vectors and dimensionless temperature [$\theta = (T-T_i)/ (q/ (\rho\, C_p\, u_f))$]. Re = 30000, Ro = 0.125, $\beta = 90^o$ and $\Delta\rho/\rho = 0.1$: (a) $Z/D_h = 12$; (b) $Z/D_h = 22$.
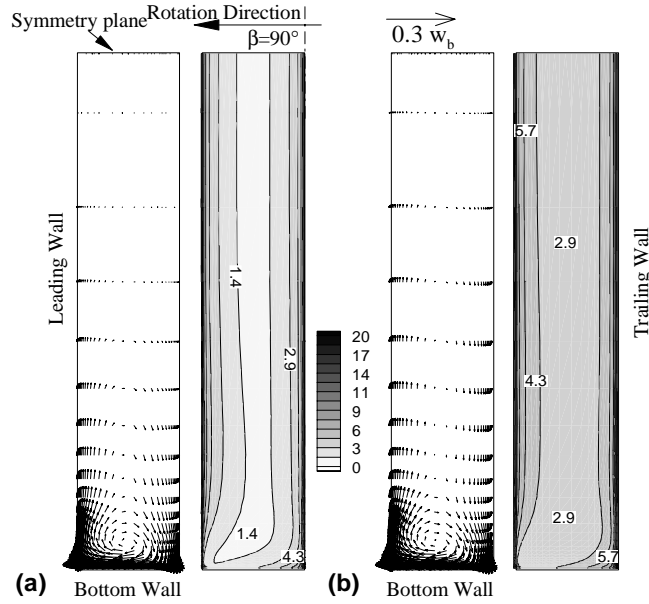
Figure 5.4: Secondary flow vectors and dimensionless temperature [$\theta = (T-T_i)/ (q/ (\rho\, C_p\, u_f))$]. Re = 30000, Ro = 0.125, $\beta = 90^o$ and $\Delta\rho/\rho = 0.2$: (a) $Z/D_h = 12$; (b) $Z/D_h = 22$.
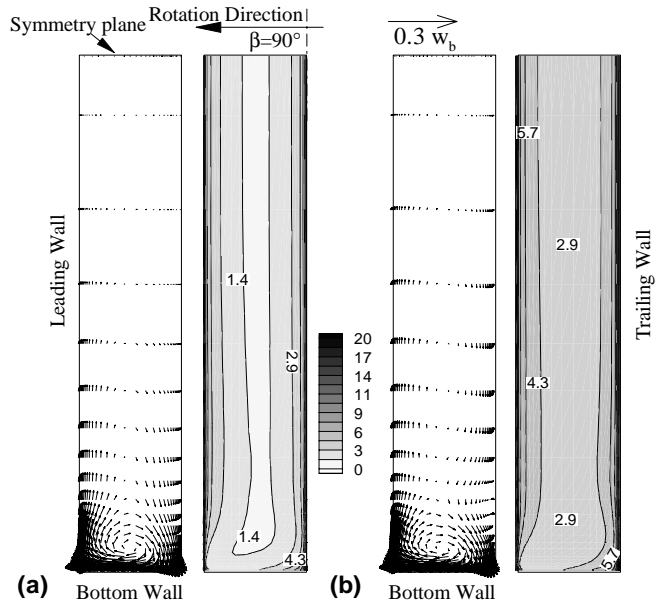
Figure 5.5: Secondary flow vectors and dimensionless temperature [$\theta = (T-T_i)/ (q/ (\rho\, C_p\, u_f))$]. Re = 30000, Ro = 0.125, $\beta = 90^o$ and $\Delta\rho/\rho = 0.4$: (a) $Z/D_h = 12$; (b) $Z/D_h = 22$.
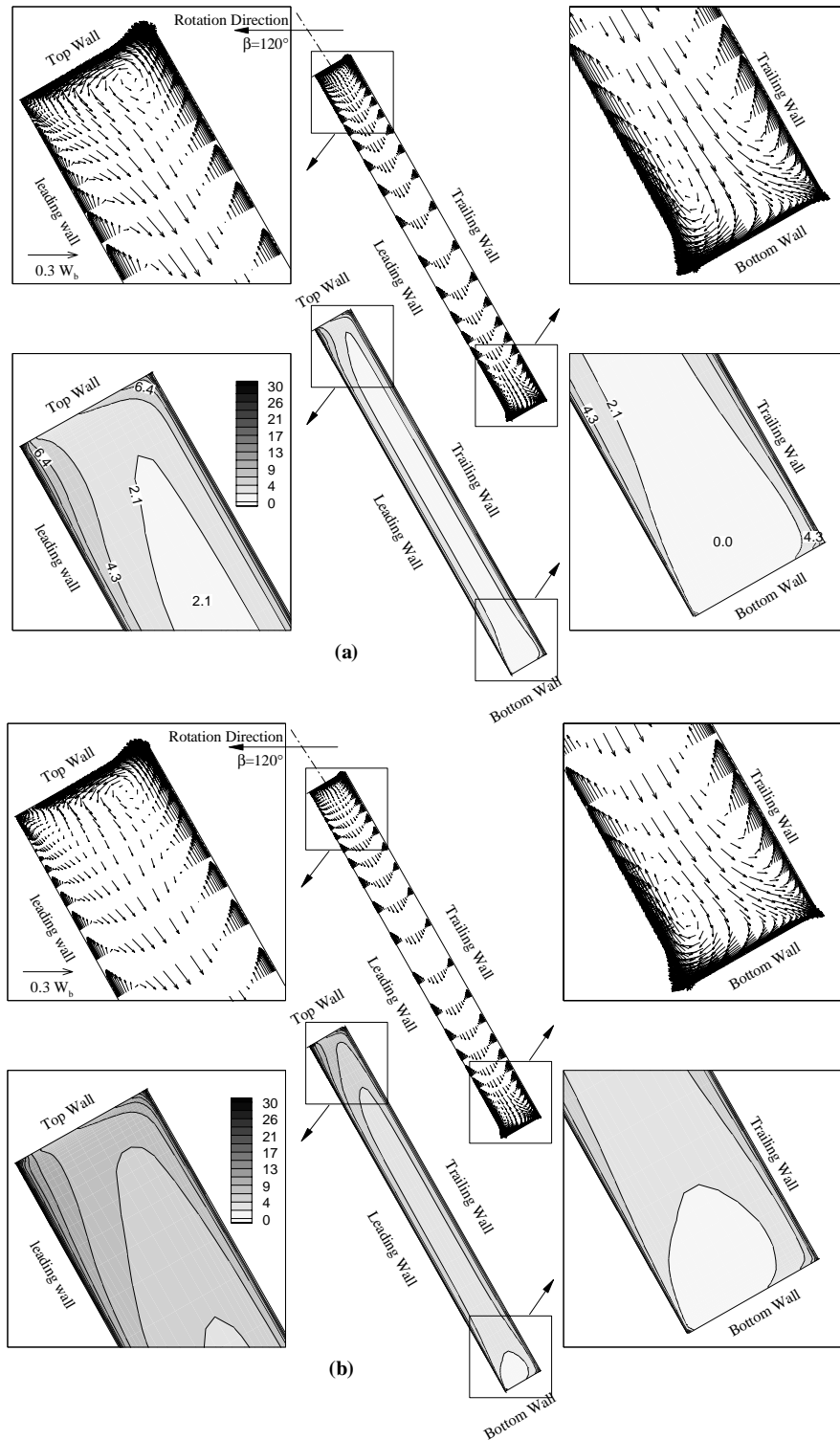
Figure 5.6: Secondary flow vectors and dimensionless temperature [$\theta = (T-T_i)/ (q/ (\rho C_p u_f))$]. Re = 30000, Ro = 0.125, $\beta = 120^o$ and $\Delta\rho/\rho = 0.1$: (a) $Z/D_h = 12$; (b) $Z/D_h = 22$.
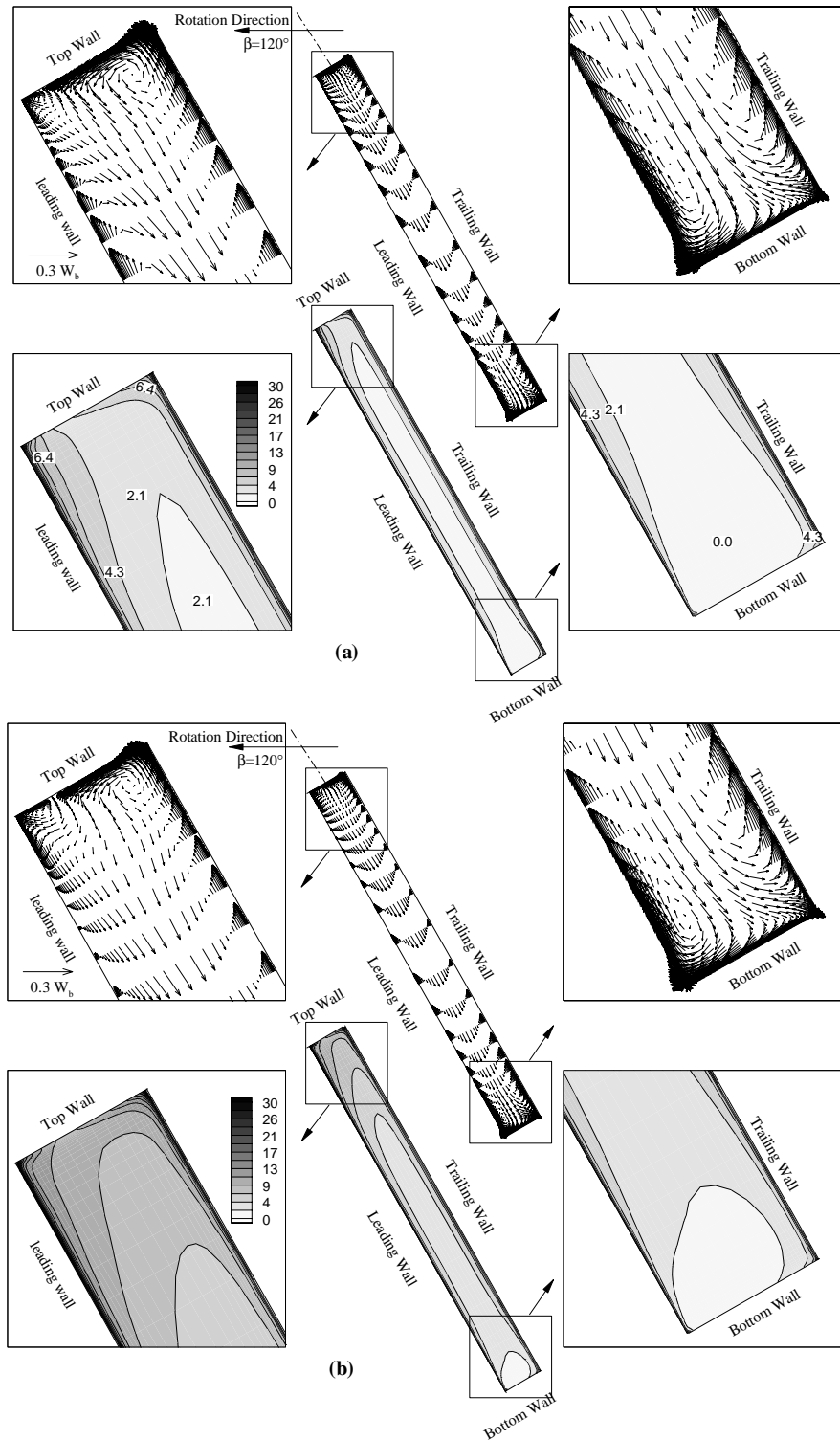
Figure 5.7: Secondary flow vectors and dimensionless temperature $[\theta = (T\text{-}T_i)/ (q/ (\rho\, C_p\, u_f))]$. Re = 30000, Ro = 0.125, $\beta = 120^o$ and $\Delta\rho/\rho = 0.2$: (a) $Z/D_h = 12$; (b) $Z/D_h = 22$.
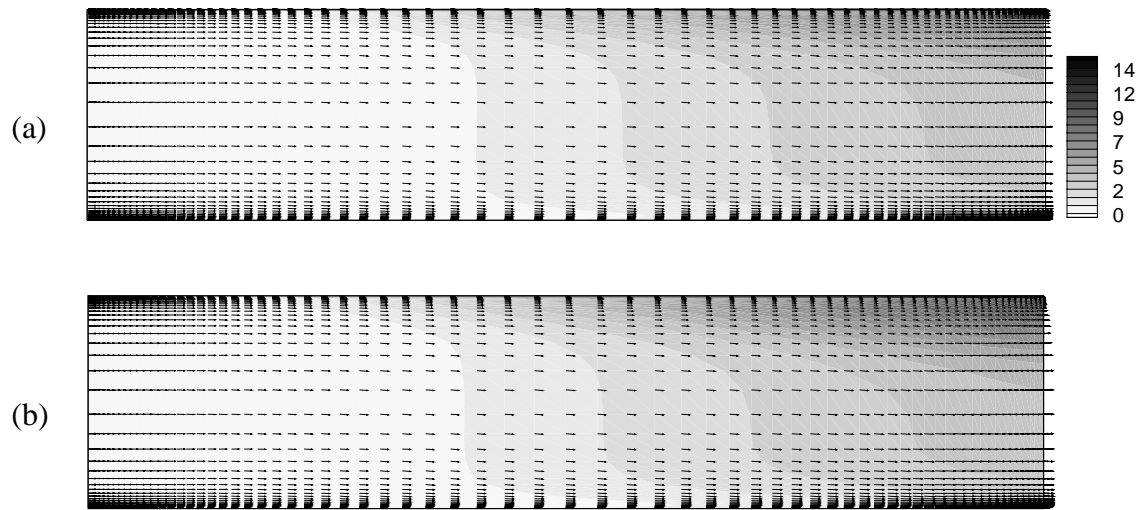
Figure 5.8: Velocity vectors and dimensionless temperature $[\theta = (T-T_i)/ (q/ (\rho\ C_p\ u_f))]$ contours midway between leading and trailing wall. Re = 30000: (a) Ro = 0.125, $\beta = 120^o$ and $\Delta\rho/\rho = 0.1$; (b) Ro = 0.125, $\beta = 120^o$ and $\Delta\rho/\rho = 0.2$.

5.4. Local heat transfer-coefficient

The effect of the Coriolis, buoyancy, and centripetal forces exerts strong influence on the heat transfer characteristic in rotating channels. Results of heat transfer for various rotation number, Ro, and density ratio, $\Delta\rho/\rho$ for leading and trailing wall are presented in this section. Heat transfer result of stationary case will be used to compare with other cases.

Effect of increasing the rotation number, Ro, on leading wall

Calculated Nusselt number ratios contours on leading wall for stationary case are shown in Figure 5.9a. It can be seen that high Nusselt number ratios contours exist near the beginning of leading wall due to thinner boundary layers. It can be seen also in region next to the top and bottom walls that Nusselt number ratios is quite high when compared to core region. This is because of high temperature gradient that resulted due to nature of boundary condition (top and bottom wall are adiabatic). For the case of rotation number, Ro = 0.125, β =120° and density ratio, $\Delta\rho/\rho$ = 0.1, the Nusselt number ratios pattern changes dramatically with high and low Nusselt number ratios contours being next to bottom and top walls, respectively (Figure 5.9e), which is due to action of coriolis force that sweeps cold fluid from the bottom wall to top wall via leading wall, and hence high heat transfer at the bottom portion of the leading wall. The Nusselt number ratios next to bottom portion in this case is 15 percent higher that of stationary case.

Effect of increasing density ratio, $\Delta\rho/\rho$ on leading wall

 To portray the effect of increasing the density ratio on leading wall, case 4, and 5 are selected, which have common rotation number of 0.125. Figure 5.9e and Figure 5.9f shows the calculated Nusselt number ratios contours for above mentioned cases. In Figure 5.9e, the Nusselt number ratios range from 3.66 to 0.5 with high value Nusselt number ratios contour at the inlet and bottom portion. Increase in density ratio, $\Delta\rho/\rho$ seems to have appreciable effect on Nusselt number ratios distribution and magnitude on leading wall, which is depicted in Figure 5.9f. Low Nusselt number ratios are found next to top wall in the downstream region. This is due to the rotation induced secondary flow, which pushes cold fluid from the top wall to the bottom wall.

Effect of increasing rotation number on the trailing wall

To show the effect of rotation on heat transfer characteristics on the trailing wall, calculated Nusselt number ratios for higher rotation number is compared with Nusselt number ratios obtained for stationary channel. So, again we refer back to Figure 5.10a for calculated Nusselt number ratios contours on trailing wall for stationary case. This is because; in stationary channel the heat transfer characteristic is same on both leading and trailing wall. The calculated Nusselt number ratios contours Ro = 0.125 and density ratio, $\Delta\rho/\rho = 0.1$, is shown in Figure 5.10d. In this figure, pattern of the Nusselt number ratios contours is remarkably different from the stationary channel. High Nusselt number ratios contours next to the bottom wall occur all the way to the end of the channel. Again here a low Nusselt number ratios contour starts appearing in the top and outlet portion of the trailing wall.

Effect of increasing density ratio on trailing wall

In Figure 5.10d, the rotation number, Ro, is kept at 0.125 and density ratio is increased to 0.1. Here the Nusselt number ratios contour next to bottom wall attains to a value of 1.89.and again it is seen that the low Nusselt number ratios contours stretch towards the upstream. In Figure 5.10e, the density ratio, $\Delta\rho/\rho$, is increased further to 0.2 while keeping the rotation number, Ro, to 0.125. Nusselt number ratios next to bottom surface attains a value as high as 2.22 times the corresponding Nusselt number ratios in the stationary case, and a Nusselt number ratios contour valued 0.95 appear on top surface showing location of hot fluid close to the top surface.

Effect of channel orientation on the leading and trailing wall

Figure 5.9c and Figure 5.9f, shows the leading wall Nusselt number ratios contours for same rotation number, Ro = 0.125 and density ratio, $\Delta\rho/\rho$ = 0.l, but with orientation β = 90° and 120°, respectively. Figure 5.10b and Figure 5.10e, shows the trailing wall Nusselt number ratios contours for same rotation number, Ro = 0.125, but with orientation β = 90° and 120°, respectively. Nusselt number ratios contour pattern on leading wall for orthogonal orientation, are quite different form the β = 120°, with high Nusselt number ratios contours on top and bottom region. After comparing with stationary case, it is found the Nusselt number ratios obtained in the later case is higher. When trailing wall Nusselt number ratios for case 7 (which is shown in Figure 5.10e), is compared with stationary case, it is found that the Nusselt number ratios for case 7 is 10% higher.

5.5. Spanwise averaged heat transfer coefficients

There are four figures presenting the Spanwise averaged Nusselt number ratios on leading and trailing wall for all the cases mentioned in Table 5.1. Figure 5.11a and Figure 5.11b, shows the Spanwise averaged Nusselt number ratios for leading and trailing wall, respectively for case 1, 2, 3, and 4. In these figures it is seen that the Spanwise averaged Nusselt number ratios decreases at the entry region, with increase in density ratio, $\Delta\rho/\rho$. However, downstream and beyond the middle of the leading wall, the spanwise averaged Nusselt number ratios begin to increase slightly with increase in density ratio, $\Delta\rho/\rho$. While on trailing wall the spanwise averaged Nusselt number ratios seem to decrease with increase in density ratio, $\Delta\rho/\rho$. Figure 5.11a and Figure 5.11b presents the spanwise averaged Nusselt number ratios on leading and trailing wall for the case 6 and 7, in which the channel makes an angle of 120° from the rotation direction. Again it is seen that the spanwise average Nusselt number ratios on leading and trailing wall decreases in the entry region with increase in density ratio, $\Delta\rho/\rho$. but it is seen to increase from middle and downstream of the heated sections. It is seen from these figures that the spanwise Nusselt number ratios increase with increase in rotation number, Ro, for both leading and trailing wall.

5.6. Comparison with experiment

To validate the results, we carried out extra simulation for rotation number, Ro, and density ratio, $\Delta\rho/\rho$, similar to that of experiments of Willet and Bergles [11], and results were shown in Figure 5.13. It can be seen that the computed Nusselt number is overestimated to experiment data of [11]. This difference can be attributed partially to uncertainty in experimental data ($\pm$ 11 percent) & partially to numerical errors.
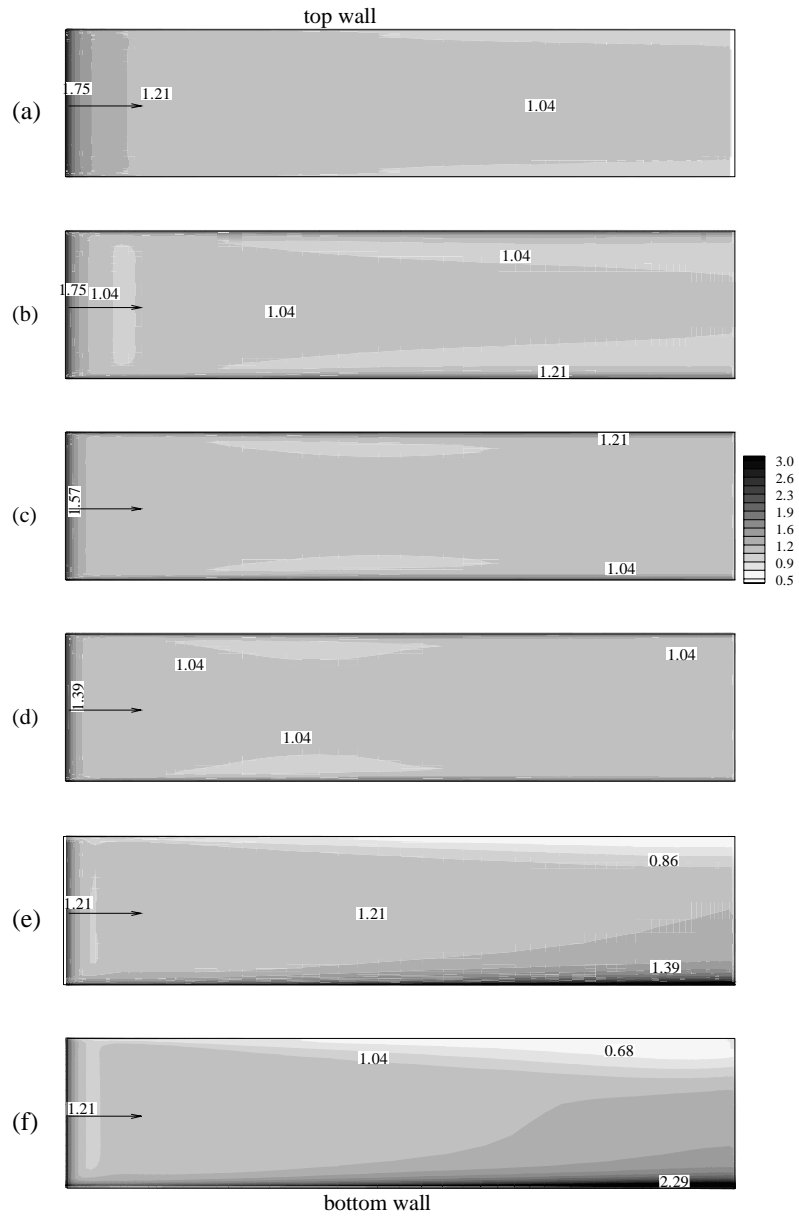
Figure 5.9: Nusselt number distribution on leading wall. Re = 30000: (a) Ro = 0.0 and

$\Delta\rho/\rho$ = 0.1; (b) Ro = 0.125, β = 90° and $\Delta\rho/\rho$ = 0.1; (c) Ro = 0.125, β = 90° and $\Delta\rho/\rho$ =0.2; (d) Ro = 0.125, β = 90° and $\Delta\rho/\rho$ = 0.4; (e) Ro = 0.125, β = 120° and $\Delta\rho/\rho$ = 0.1; (f) Ro = 0.125, β =120° and $\Delta\rho/\rho$ = 0.2.

Figure 5.10: Nusselt number distribution on trailing wall. Re = 30000: (a) Ro = 0.125, β = 90⁰ and Δρ/ρ = 0.1; (b) Ro = 0.125, β = 90⁰ and Δρ/ρ = 0.2; (c) Ro = 0.125, β = 90⁰ and Δρ/ρ = 0.4; (d) Ro = 0.125, β = 120⁰ and Δρ/ρ = 0.1; (e) Ro = 0.125, β =120⁰ and Δρ/ρ = 0.2.
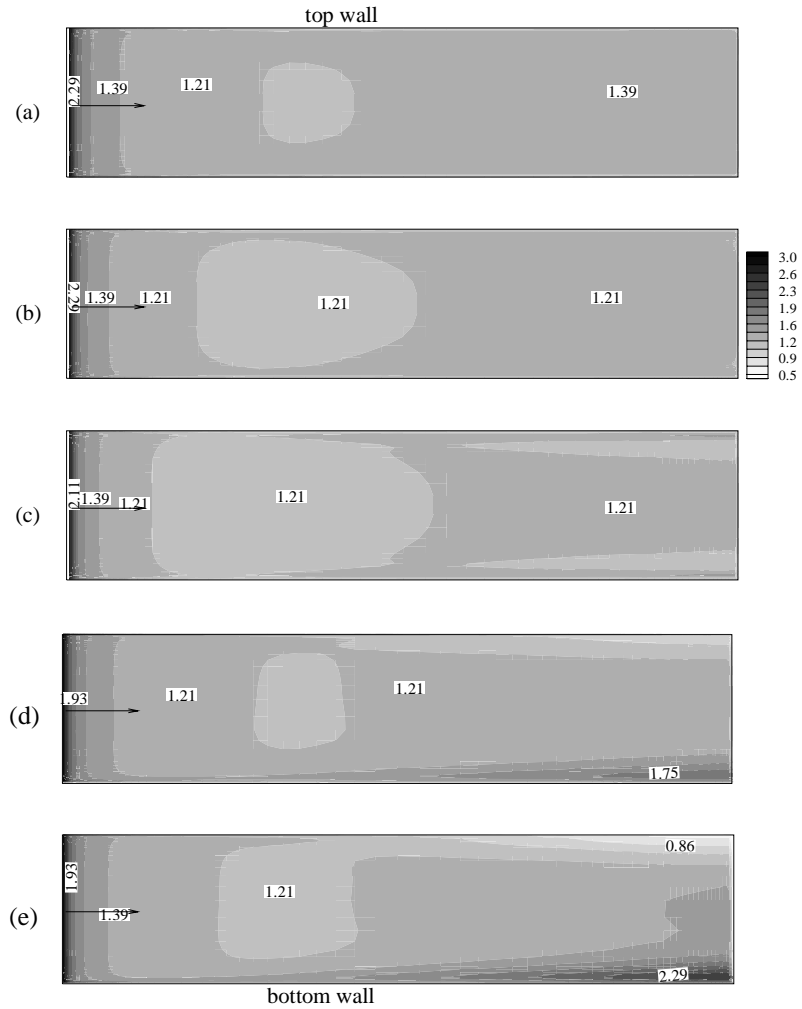
Figure 5.10: Nusselt number distribution on trailing wall. Re = 30000: (a) Ro = 0.125, $\beta = 90^0$ and $\Delta\rho/\rho = 0.1$; (b) Ro = 0.125, $\beta = 90^0$ and $\Delta\rho/\rho = 0.2$; (c) Ro = 0.125, $\beta = 90^0$ and $\Delta\rho/\rho = 0.4$; (d) Ro = 0.125, $\beta = 120^0$ and $\Delta\rho/\rho = 0.1$; (e) Ro = 0.125, $\beta = 120^0$ and $\Delta\rho/\rho = 0.2$.

Figure 5.11: Spanwise averaged Nusselt number. Re = 30000, $\beta = 90^{\circ}$: (a) leading wall; (b) Trailing wall.
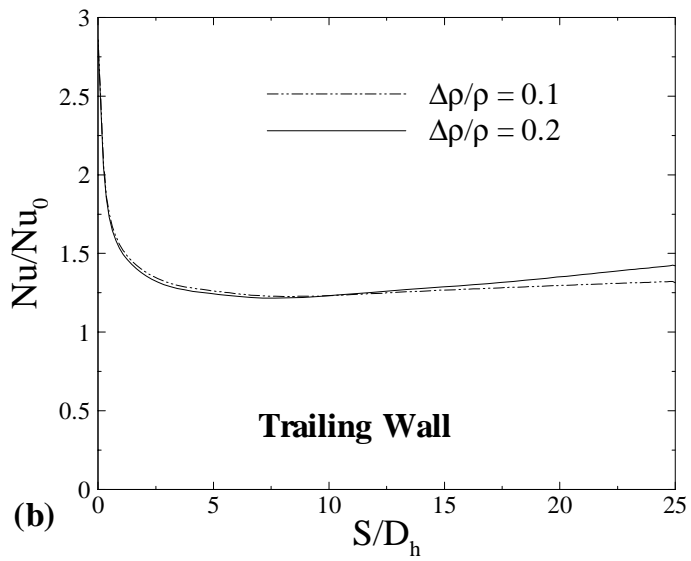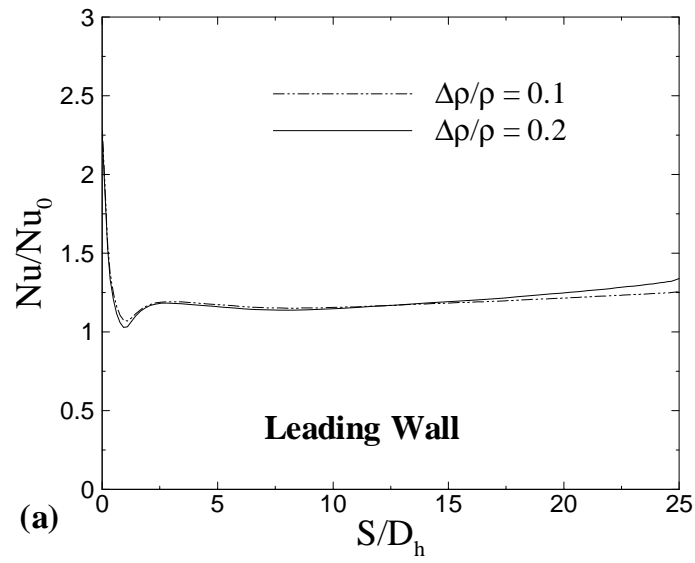
Figure 5.12: Spanwise averaged Nusselt number. Re = 30000, Ro = 0.125 & β =120$^{\text{o}}$: (a) Leading wall; (b) Trailing wall.
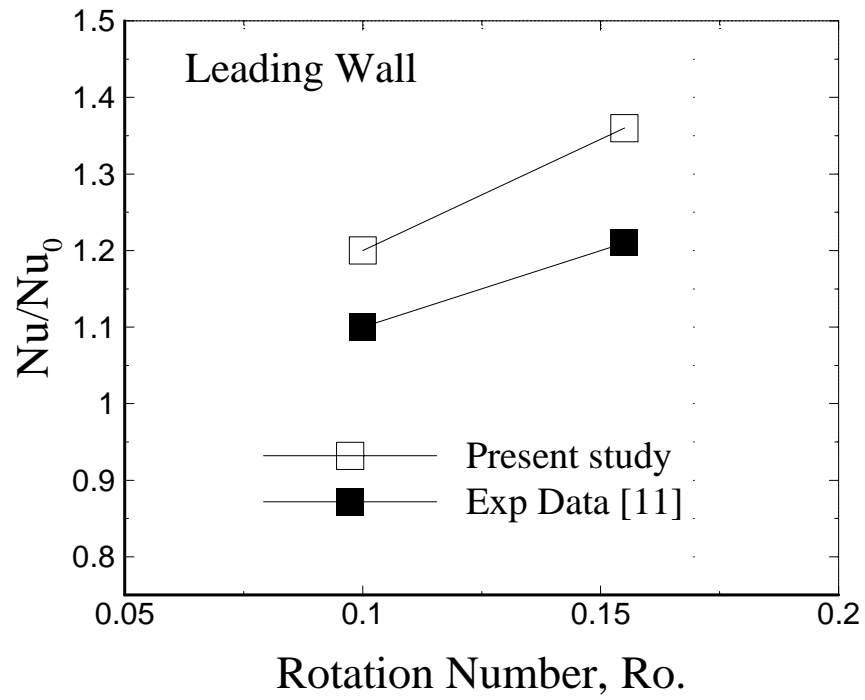
Figure 5.13: Comparison of Average Nusselt number.

CHAPTER 6

CONSTANT TEMPERATURE BOUNDARY CONDITION

6.1. Introduction

This chapter presents results and discussion for smooth channels with leading and trailing walls being held at constant surface temperature while the top and bottom walls are kept adiabatic. Computational cases are summarized in Table 6.1. Reynolds number based on channel hydraulic diameter is kept constant, and equals 30000. Rotation number, Ro, and density ratio, $\Delta\rho/\rho$, in computation were varied from 0 to 0.25 and 0.1 to 0.4 respectively, for two channel orientations of $\beta = 90^o$ and 120°. All computations presented here were obtained by starting with the stationary case and then gradually increasing the rotation speed.

The effect of rotation, Ro, density ratio, $\Delta\rho/\rho$, and channel orientation on flow field is discussed first, followed by heat transfer results. Flow field is represented in form of relative velocity vectors. Dimensionless temperature is defined as in equation (4.3a). Nusselt number is defined as in equation (4.5), and Nusselt number is normalized using equation (4.4).

Table 6.1: Computational cases for constant wall temperature boundary condition

Case	Rotation Number, Ro	Density Ratio, $\Delta\rho/\rho$	β
1	0.0	0.1	--
2	0.125	0.1	90°
3	0.125	0.2	90°
4	0.125	0.4	90°
5	0.125	0.1	120°
6	0.125	0.2	120°
7	0.125	0.4	120°
8	0.25	0.1	120°
9	0.25	0.2	120°
10	0.25	0.4	120°

6.2. Velocity and temperature field

It is worth to mention in the beginning of the discussion that the results presented at axial locations are viewed from upstream of the channel. Since the channel has high aspect ratio, some plots are magnified at critical regions to have better visualization. Secondary flow is known to affect the heat transfer in rotating turbulent flow, so secondary flow and dimensionless temperature field are discussed first and then discussion will focus on streamwise flow and dimensionless temperature field. Calculated secondary flow vectors and dimensionless temperature contours at two axial locations (Z/D_h = 12 and 22) for all the cases mentioned in Table 6.1 are presented in Figure 6.1 through Figure 6.10. Calculated secondary flow vectors and dimensionless temperature contours for stationary case (case 1) is shown in Figure 6.1. Four vortices at the corners are formed due to anisotropy in Reynolds stresses. From the corresponding dimensionless temperature contours it seen that cold fluid is located at core region of the channel. As we move on downstream of the channel (Figure 6.1b), the secondary flow pattern is same but, the fluid is heated more in the core region of the channel.

Figure 6.2 shows secondary flow vectors and dimensionless temperature contours for the case 2. Coriolis force which arises due to system rotation, that pushes cold fluid from the core towards the trailing wall and then to top wall and bottom wall and then brings it back along leading wall to core. This leads to formation of vortices in the regions close to top and bottom wall of the channel, one of which can be viewed clearly in the magnified portion of the Figure 6.2a. The transport of relatively cooler, and hence heavier, fluid from the core region to the trailing wall results in high temperature gradient (hence higher heat transfer) on the trailing wall. After receiving considerable amount of heat from the

trailing wall, the fluid sweeps to the leading wall along the top and bottom walls creating low temperature gradient (relatively low heat transfer) on leading wall. This can be seen in corresponding dimensionless temperature contours of Figure 6.2b. And it is worth noticing that the temperature gradient at the leading corners is high when compared with temperature gradient at trailing corners, this is due to the fact that the top and bottom walls are unheated and some portion of cold fluid from core region is directly pushed to top and bottom walls and then to leading corners resulting into high temperature gradient. Figure 6.3 and Figure 6.4, show the computed secondary flow-vectors and dimensionless temperature contours for case 3 and 4. It is seen that as the density ratio, $\Delta\rho/\rho$, is increased to 0.2 and 0.4 while fixing the rotation number, Ro to 0.125, the secondary flow pattern is seemed to remain unchanged.

Figure 6.5a and Figure 6.5b Show the computed secondary flow vectors and dimensionless temperature contours for case 5 at $Z/D_h= 12$ and 22 respectively. In this case the channel orientation angle, β equals 120°. One can notice from the figures, that the Coriolis-induced secondary flow pushes the cold fluid away from the leading corner of the top wall to the core region and then to bottom wall, thereby causing the fluid located in vicinity of the bottom wall to sweep upwards along the leading and trailing wall. This action of Coriolis force sets two elongated counter rotating vortices near the leading and trailing wall, and a third vortex at the top trailing corner. As mentioned before, that the cooler fluid sweeps along and upwards of the leading and trailing wall, and so it is expected that the velocity and thermal boundary layers to be thin in the lower portion of leading and trailing walls, and hence high temperature gradients, and due to this secondary flow behavior, cold fluid is located near the bottom portion. This is

illustrated in corresponding dimensionless temperature contours of Figure 6.5b. As density ratio, $\Delta\rho/\rho$ is increased to 0.2 (Figure 6.6a and 6.6b), the calculated secondary flow patterns at two axial locations remain unchanged, but the strength of flow increases, especially in the core region of the channel, and also it is seen that the dimensionless temperature contour pattern remains same.

Now, consider Figure 6.7a that shows computed secondary flow vector and dimensionless contours for the case 7 ($\Delta\rho/\rho$ increased to 0.4) at axial location $Z/D_h = 12$. Here the secondary flow pattern resembles to secondary flow pattern of the case 6, but the magnitude of secondary flow is higher. Further downstream of the channel (Figure 6.7b, $Z/D_h = 22$), secondary flow is quite different, with Coriolis force pushing the fluid from top trailing corner to leading wall (see magnified figure) and then to bottom wall through core region. The secondary flow vortex on trailing wall stretches from bottom trailing corner to almost top trailing corner, while the secondary flow vortex on near leading wall does not.

Figure 6.8 through Figure 6.10 show the calculated secondary flow vectors and dimensionless temperature contours for the case 8 to 10 which are for the same rotation number (Ro=0.25). As rotation number is increased to 0.25 the vortex near leading and trailing wall is pushed towards the bottom wall, and third small vortex appears in the vicinity of top wall (Figure 6.8a). Downstream of the channel, the third vortex is well established that pushes warm fluid from leading wall to trailing wall via top wall. And since Coriolis force is function of angular velocity and radial distance, it is apparent from the Figure 6.8b, that the strength of the secondary flow vectors is higher than the previous

case. From the corresponding temperature contours at two axial locations, it is seen that temperature gradient is high (relatively to trailing wall) in the vicinity of top leading corner and small temperature gradient in the vicinity of to trailing corner and hence high rate of heat transfer at the top leading corner when compared to top trailing corner of the channel. As density ratio, $\Delta\rho/\rho$, is increased to 0.2, the secondary flow vectors at axial location Z/D_h equals 12, the third secondary flow vortex grow to considerable size in the top portion of the channel that pushes fluid from core to leading wall and then on and along top wall and then to trailing wall and then lastly to bottom wall via leading wall. This behavior is illustrated in Figure 6.9a. In corresponding dimensionless temperature contour plot of Figure 6.9a, the fluid in the core top portion of the channel is uniformly heated due to mixing action of third secondary flow vortex. At downstream location of $Z/D_h = 22$, for the same case this type of secondary flow behavior is absent (Figure 6.9b). This is can be accredited to flow reversal in top portion of channel. Phenomena of flow reversal are explained well in later stage of discussion. Further increase in density ratio, $\Delta\rho/\rho$, is seen to have no appreciable effect on secondary flow pattern at either axial location, except increase in mixing action at the bottom wall region of the channel (Figure 6.10a and Figure 6.10b), and hence increase in heat transfer.

Now focus is turned on to stream wise flow and dimensionless temperature field for different cases, of which some of the cases depict role of buoyancy and hence effect of rotation (rotation number, Ro) and density ratio, $\Delta\rho/\rho$. Figure 6.11 shows combined velocity vectors and dimensionless temperature contours midway between leading and trailing wall for the cases 1, 4, 5, 6 7, 8, 9 and 10. In all cases of the above figure the unheated section is omitted to focus on heated section of the channel. The main intention

to illustrate these plots is to highlight the effect of buoyancy on the flow field and hence heat transfer. Figure 6.11a shows calculated velocity vectors and dimensionless temperature contours for case of stationary channel (Ro = 0.0 and $\Delta\rho/\rho$ = 0.1), which exhibits a typical channel flow, with velocity and dimensionless temperature being symmetry about the centerline. Since the top and bottom wall are unheated, the dimensionless temperature ranges from 0 to 0.5.

Under orthogonal rotation mode (Ro = 0.125) even for high density ratio, $\Delta\rho/\rho$ = 0.4, the velocity vector throughout the channel still resemble to velocity vectors in stationary case ,and no flow reversal , while fluid being heated more as it passes through the channel, this is simply due to mixing action of Coriolis force that is acting on the system. This is demonstrated in Figure 6.11b. Figure 6.11c shows the calculated velocity vectors and dimension temperature contours midway between the leading and trailing wall, for case, 5, 6 and 7. For first and second cases the velocity vectors are thick at the bottom wall and thin at the top wall (Figure 6.11e and Figure 6.11f). This is because the relatively cold and heavier fluid at the bottom wall experience high buoyancy forces than the warm fluid at the top wall. As the density ratio, $\Delta\rho/\rho$, is increased to 0.4, while fixing the rotation number, Ro to 0.125, the buoyancy force is seem to increase the fluid velocity at the bottom wall in the downstream of the channel dramatically, and in order maintain continuity in the flow, hot and lighter fluid at the top wall decelerates. At this rotation number, Ro and density ratio, $\Delta\rho/\rho$, the penetration of reverse flow near top wall is limited to approximately 10 hydraulic diameters from the outlet. And hence high heat transfer is noticed in this region. As the rotation number, Ro, is increased to 0.25, even for low density ratio, $\Delta\rho/\rho$ of 0.1, buoyancy force is seem to be dominant with flow

reversal taking place near top wall and the penetration of reverse flow is almost 80 percent of the heated length and flow reversal thickness in span-wise direction from top wall is approximately 3 hydraulic diameter. That can be viewed from the Figure 6.1g. Figure 6.17h, 6.17i and 6.17j show the calculated velocity and dimensionless temperature contours midway between leading and trailing wall, for the cases 9 and 10. As density ratio, $\Delta\rho/\rho$, is increased, while keeping the rotation number, Ro to 0.25, the buoyancy force further enhances the flow reversal process. It is clearly visible that the reverse flow reaches the inlet for case 10, and depth and strength of this reverse flow increase with increase in density ratio, $\Delta\rho/\rho$, and it is seen from the dimensionless temperature contours that for all the cases the cold fluid is located at the bottom wall and hence high heat transfer.

To see the effect of buoyancy on fluid flow near leading and trailing wall, velocity vector and dimensionless temperature contour are shown on a plane midway between top and bottom wall, for case 8, 9 and 10. As mentioned before, that the relatively cool and heavier fluid near the trailing wall experience higher buoyancy force than the hot and lighter fluid near leading wall. This action sets imbalance in fluid flow, this imbalance has a tendency to increase the outward velocity near trailing wall and decrease it near leading wall. And since buoyancy force is function of rotation number, Ro, density ratio, $\Delta\rho/\rho$, and radial distance, increase in one of this parameter would enhance the effect of buoyancy force on the fluid flow, and this is evident from Figure 6.12. For the case of high-density ratio, the depth of flow reversal reached half way of the channel height. Same behavior of flow reversal is reported in latest research of Al-Qahtani et al. [27].

To summarize, flow reversals start appearing in the top leading corner region, at rotation number, Ro = 0.125 and density ratio, $\Delta\rho/\rho$ = 0.4, and strength and penetration of reverse flow in both, stream wise and cross stream wise direction increases with further increase in either rotation number or rotation number.
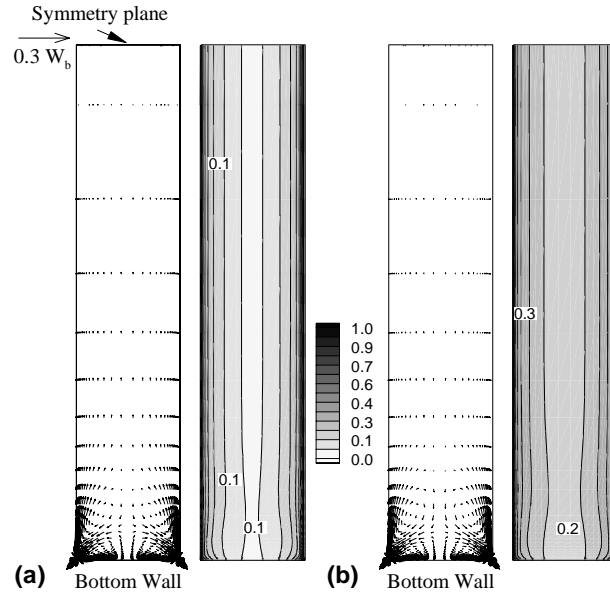
Figure 6.1: Secondary velocity vectors and dimensionless temperature [$\theta = (T-Ti)/(Tw-Ti)$] contours. Re = 30000, Ro = 0.0, and $\Delta\rho/\rho = 0.1$: (a) $Z/D_h = 12$; (b) $Z/D_h = 22$.
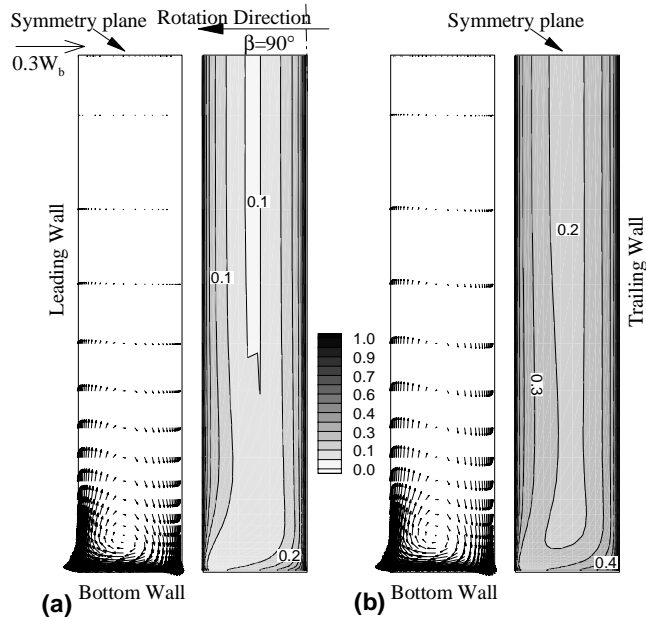

Figure 6.2: Secondary velocity vectors and dimensionless temperature [$\theta = (T-Ti)/(Tw-Ti)$] contours. Re = 30000, Ro = 0.125, $\beta = 90^0$ and $\Delta\rho/\rho = 0.1$: (a) $Z/D_h = 12$; (b) $Z/D_h = 22$.

Figure 6.3: Secondary velocity vectors and dimensionless temperature [θ = (T-Ti)/ (Tw-Ti)] contours. Re = 30000, Ro = 0.125, β = 90^0 and Δρ/ρ = 0.2: (a) Z/D$_h$ =12; (b) Z/D$_h$ = 22.

Figure 6.4: Secondary velocity vectors and dimensionless temperature [θ = (T-Ti)/ (Tw-Ti)] contours. Re = 30000, Ro = 0.125, β = 90^0 and Δρ/ρ = 0.4: (a) Z/D$_h$ = 12;(b) Z/D$_h$ = 22.
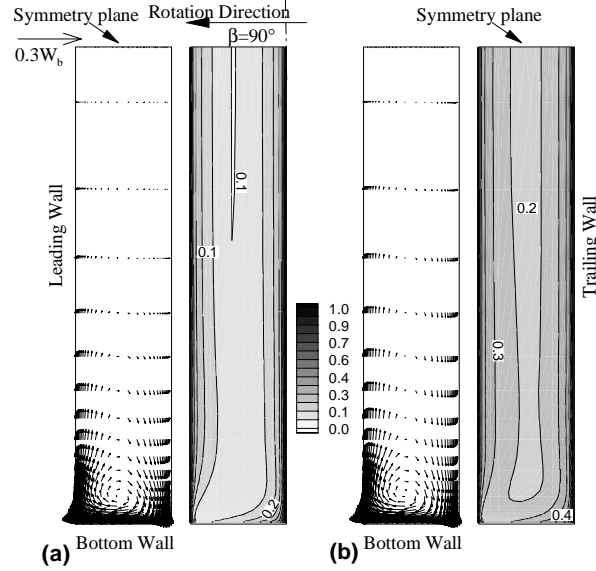
Figure 6.5: Secondary velocity vectors and dimensionless temperature [θ = (T-Ti)/ (Tw-Ti)] contours. Re = 30000, Ro = 0.125, β = 120^0, Δρ/ρ = 0.1: (a) Z/D$_h$ = 12; (b) Z/D$_h$ = 22.

Figure 6.6: Secondary velocity vectors and dimensionless temperature [θ = (T-Ti)/ (Tw-Ti)] contours. Re = 30000, Ro = 0.125, β = 120⁰, Δρ/ρ = 0.2: (a) Z/D_h = 12; (b) Z/D_h = 22.

Figure 6.7: Secondary velocity vectors and dimensionless temperature [θ = (T-Ti)/ (Tw-Ti)] contours. Re = 30000, Ro = 0.125, β = 120^0, Δρ/ρ = 0.4: (a) Z/D$_h$ = 12; (b) Z/D$_h$ = 22.
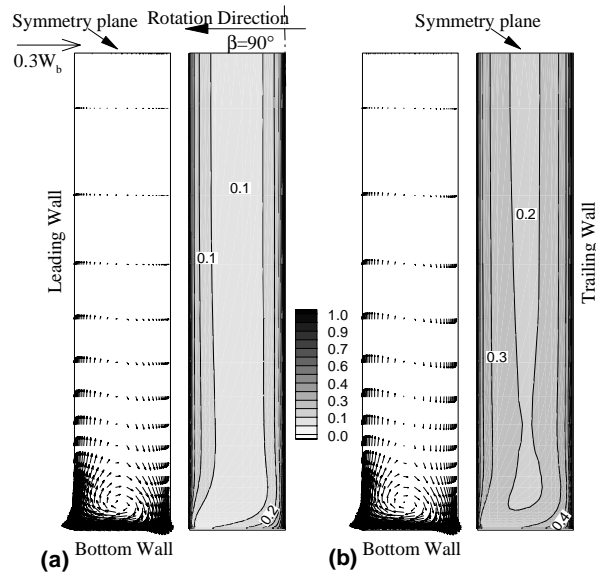
Figure 6.8: Secondary velocity vectors and dimensionless temperature [θ = (T-Ti)/ (Tw-Ti)] contours. Re = 30000, Ro = 0.25, β = 120^0, Δρ/ρ = 0.1: (a) Z/D$_h$ = 12; (b) Z/D$_h$ = 22.
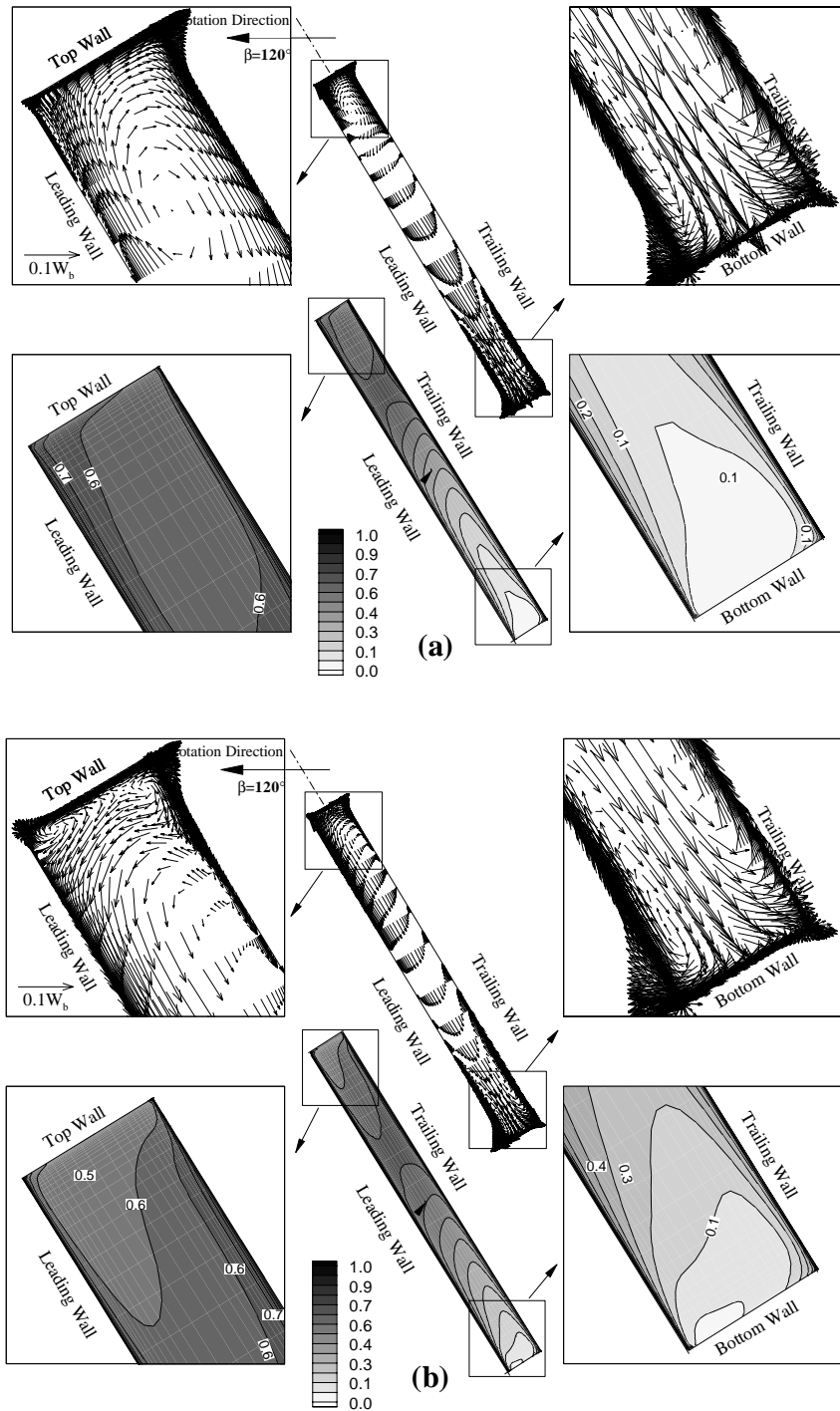
Figure 6.9: Secondary velocity vectors and dimensionless temperature [θ = (T-Ti)/ (Tw-Ti)] contours. Re = 30000, Ro = 0.25, β = 1200, Δρ/ρ = 0.2: (a) Z/D_h = 12; (b) Z/D_h = 22.
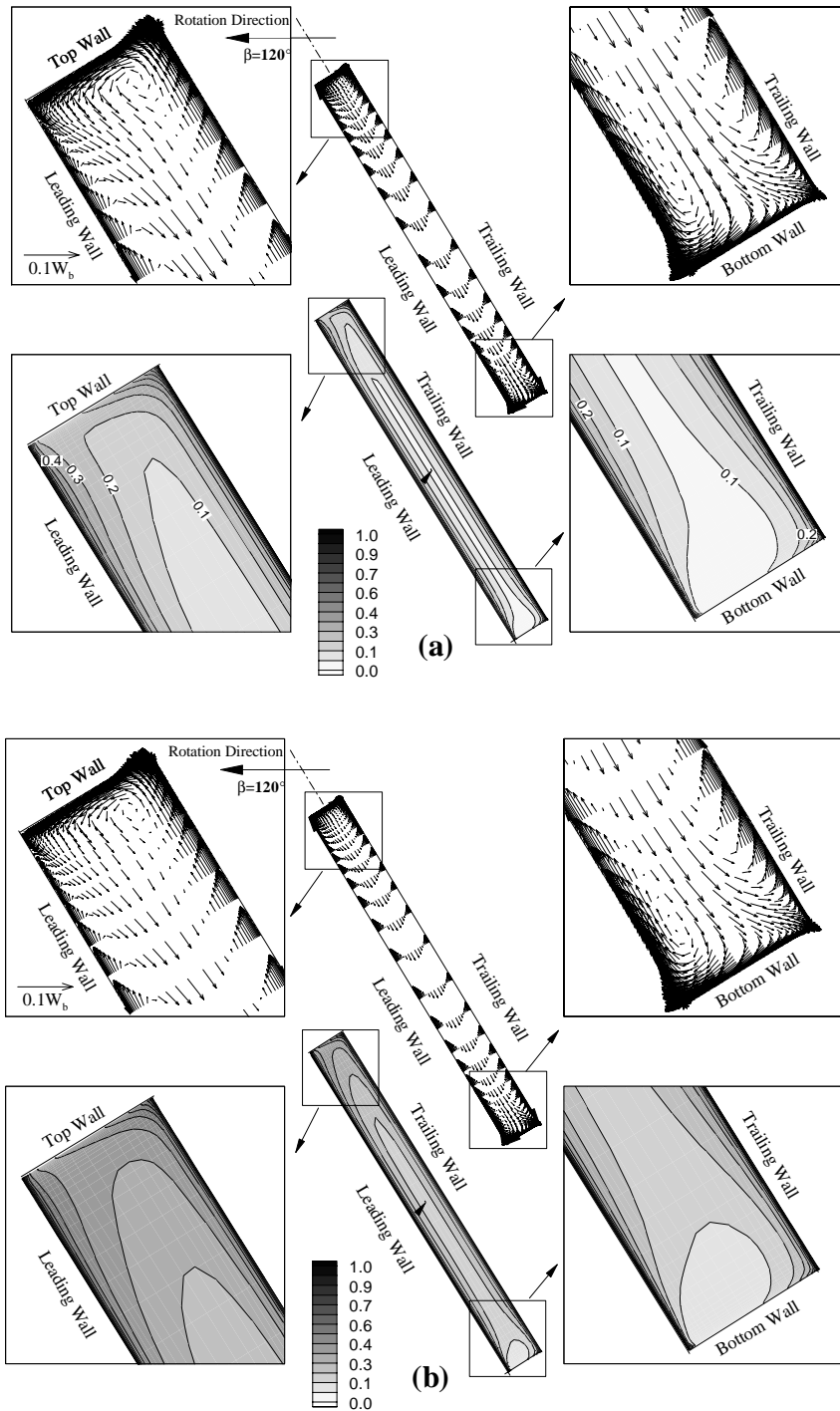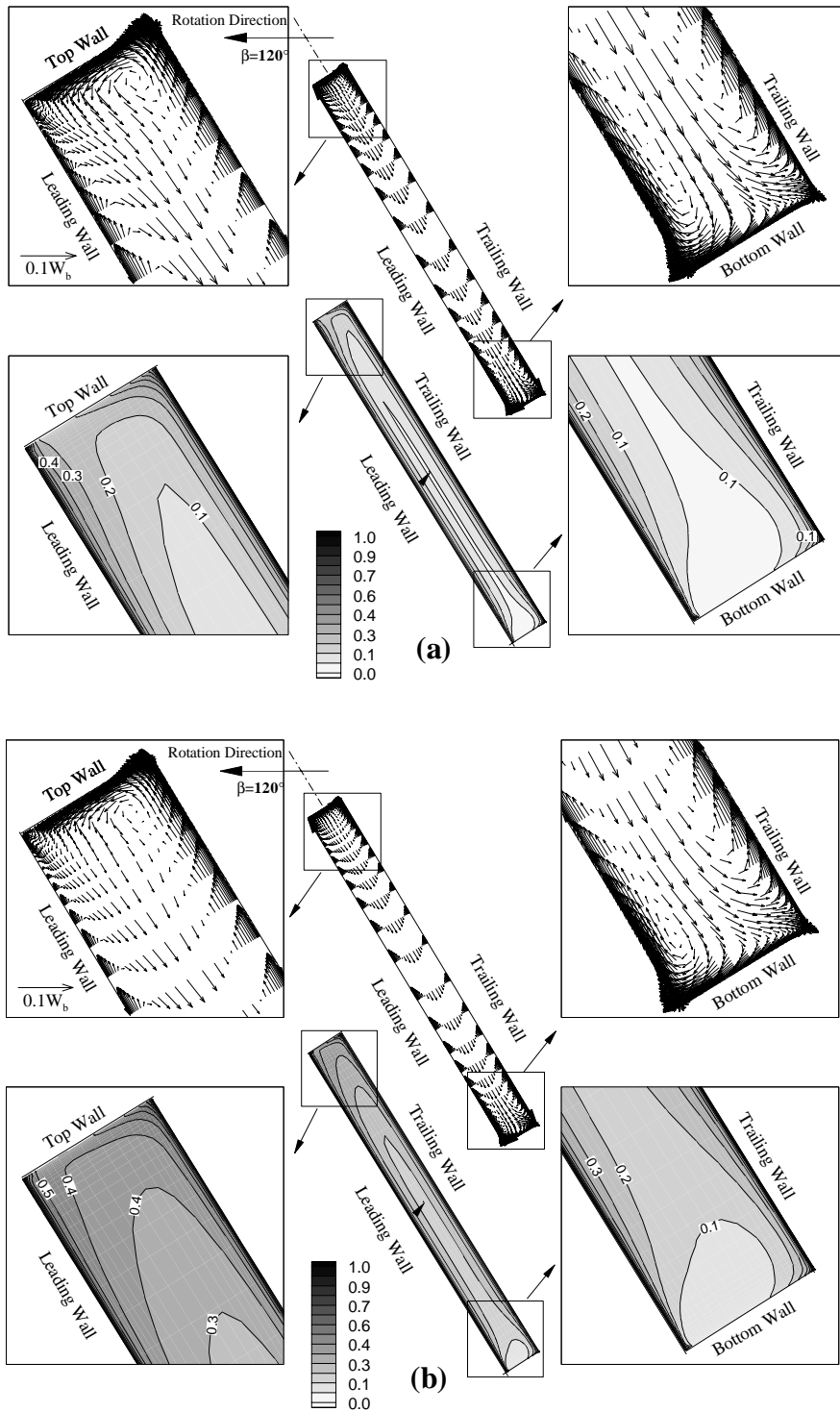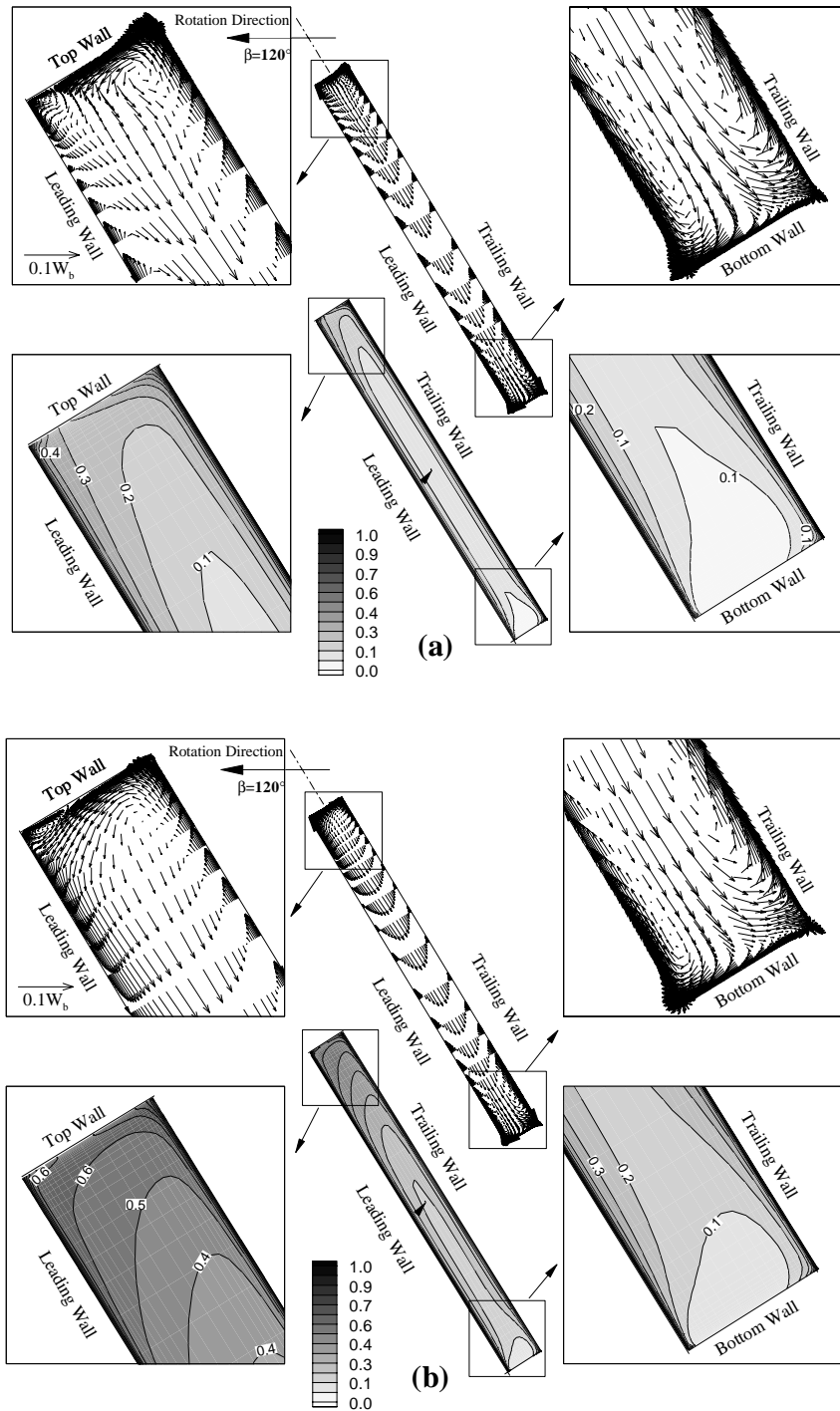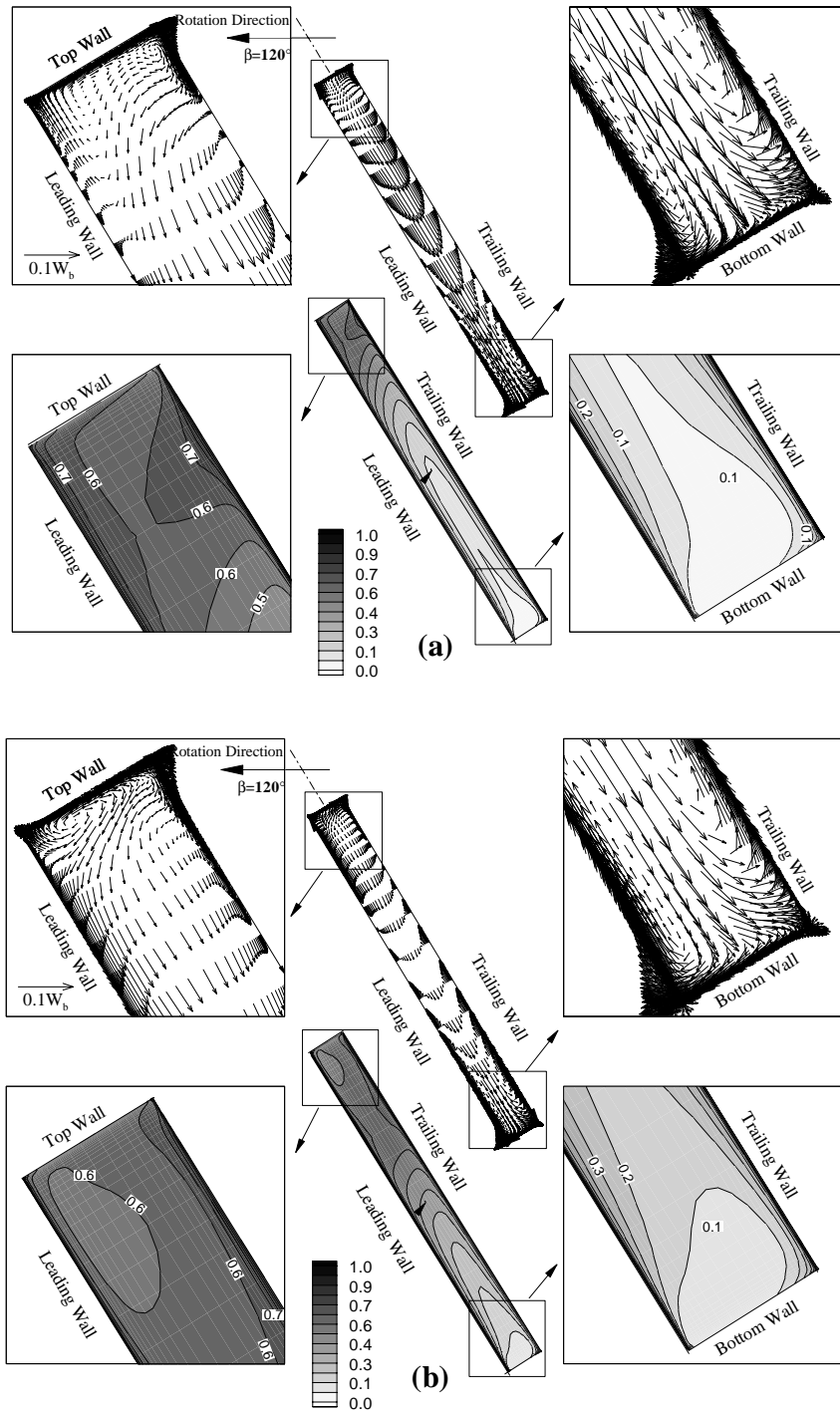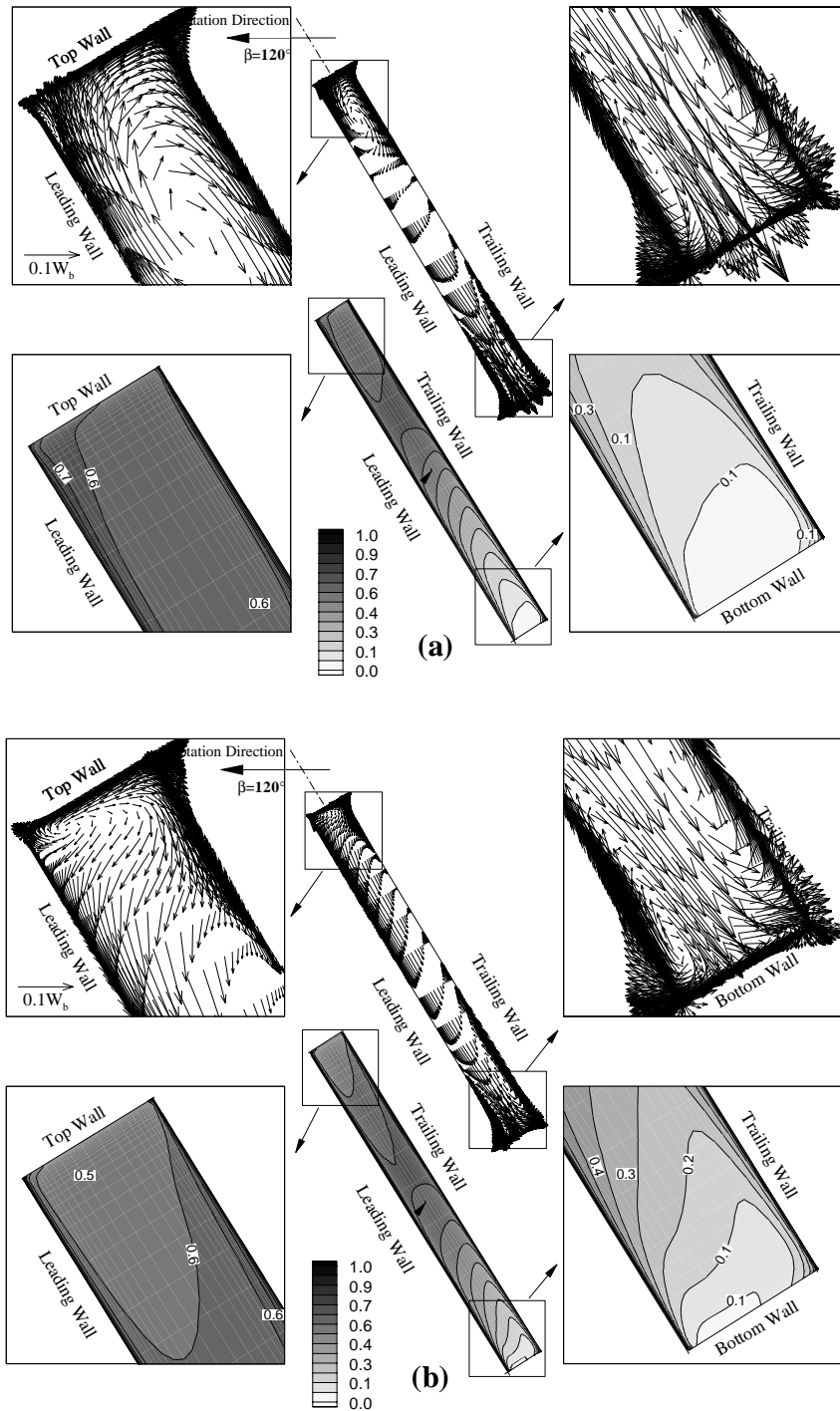
Figure 6.10: Secondary velocity vectors and dimensionless temperature [$\theta = (T-Ti)/ (Tw-Ti)$] contours. Re = 30000, Ro = 0.25, $\beta = 120^0$, $\Delta\rho/\rho = 0.4$: (a) $Z/D_h = 12$; (b) $Z/D_h = 22$.

Figure 6.11: Velocity vectors and dimensionless temperature $[\theta = (T-T_i)/ (T_w-T_i)]$ contours (midway between the leading and trailing wall). Re = 30000: (a) Ro = 0.0 and $\Delta\rho/\rho = 0.1$; (b) Ro = 0.125, $\beta = 90^o$ and $\Delta\rho/\rho = 0.1$; (c) Ro = 0.125, $\beta = 90^o$ and $\Delta\rho/\rho = 0.2$; (d) Ro = 0.125, $\beta = 90^o$ and $\Delta\rho/\rho = 0.4$; (e) Ro = 0.125, $\beta = 120^o$ and $\Delta\rho/\rho = 0.1$; (f) Ro = 0.125, $\beta = 120^o$ and $\Delta\rho/\rho = 0.2$; (g) Ro = 0.125, $\beta = 120^o$ and $\Delta\rho/\rho = 0.4$; (h) Ro = 0.25, $\beta = 120^o$ and $\Delta\rho/\rho = 0.1$; (i) Ro = 0.25, $\beta = 120^o$ and $\Delta\rho/\rho = 0.2$; (j) Ro = 0.25, $\beta = 120^o$ and $\Delta\rho/\rho = 0.4$.

94

Leading Wall

(a)

(b)

(c)

	1.00
	0.83
	0.67
	0.50
	0.33
	0.17
	0.00

Trailing Wall
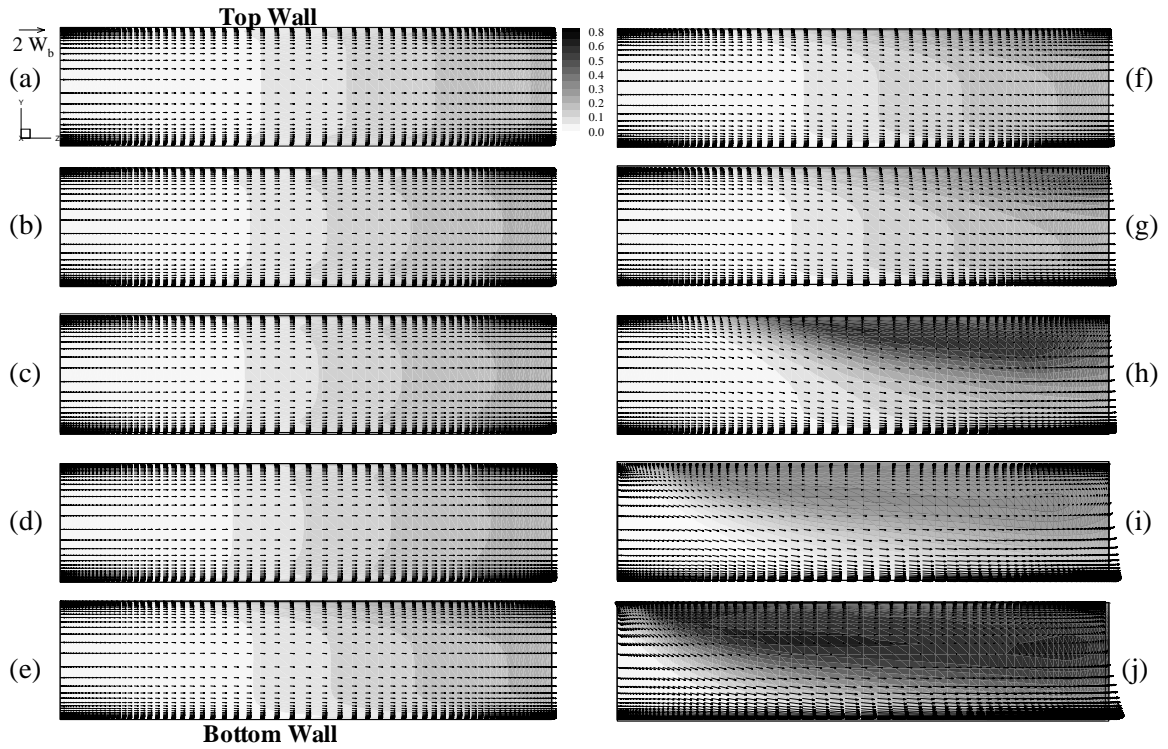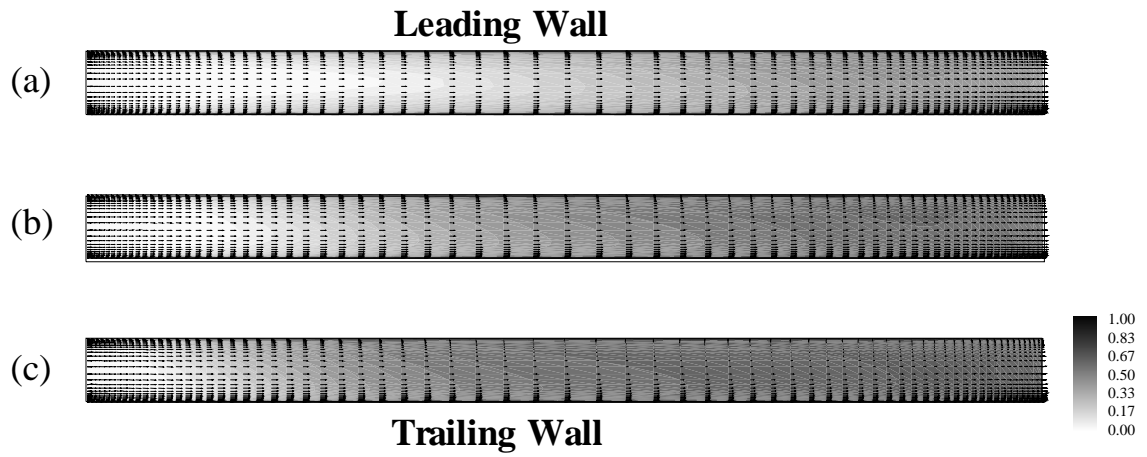
Figure 6.12: Velocity vectors and dimensionless temperature $[\theta = (T-T_i)/ (T_w-T_i)]$ contours (midway between the top and bottom wall). (a) Ro = 0.25, β =120° and $\Delta\rho/\rho$ = 0.1; (b) Ro = 0.25, β = 120° and $\Delta\rho/\rho$ = 0.2; (c) Ro = 0.25, β =120° and $\Delta\rho/\rho$ = 0.4.

6.3. Local heat transfer coefficient

The effect of the Coriolis, buoyancy, and centripetal forces exert strong influence on the heat transfer characteristic in rotating channels. Results of heat transfer for various rotation number, Ro, and density ratio, $\Delta\rho/\rho$, for leading and trailing wall are presented in figure 6.13 through figure 6.18. Heat transfer result of stationary case will be used to compare with rotating cases.

Effect of increasing the rotation number, Ro, on leading wall

Calculated Nusselt number contours on leading wall for stationary case is shown if figure 6.13a, that shows high valued Nusselt number contours near the beginning of leading wall and due to thinner boundary layers. It is seen in region next to the top and bottom wall that Nusselt number is quite high when compared to core of the wall. This is because of high temperature gradient, which resulted due to very nature of boundary condition (top and bottom wall are adiabatic) and mixing of fluid at corner. for the case of rotation number, Ro = 0.125, $\beta = 120^o$ and density ratio, $\Delta\rho/\rho = 0.1$, the Nusselt number pattern changes dramatically with high and low Nusselt number contours being next to bottom wall and top wall (Figure 6.13b), respectively, which is due to action of Coriolis force that sweeps cold fluid from the bottom wall to top wall via leading wall, and hence high heat transfer at the bottom portion of the leading wall. The Nusselt number next to bottom portion in this case is 15 percent higher that of stationary case. For the case of density ratio, $\Delta\rho/\rho = 0.1$, $\beta = 120^o$ and rotation number, Ro = 0.25, the Nusselt number contour at the bottom and down stream is seem to have a value of 3.66. It is seen that low valued Nusselt number contours next to top wall stretched more towards the inlet and to core. And also Nusselt number contour of value 1.03 is observed next to top wall, which

is due to flow reversal. Hence it can be concluded that the Nusselt number pattern and magnitude on leading wall changes and increases, respectively, with increase in rotation number, Ro.

Effect of increasing density ratio,Δρ/ρ, on leading wall

To portray the effect of increasing the density ratio on leading wall, case 5, 6 and 7 are selected, which have common rotation number of 0.25, and figure 6.13i, 6.13j and 6.13k shows the calculated Nusselt number contours for above mentioned cases. In figure 6.13i, the Nusselt number ranges from 3.66 to 0.5.with distribution of higher value Nusselt number contour at the inlet and bottom portion. Increase in density ratio, Δρ/ρ, is seem to have appreciable effect on Nusselt number distribution and magnitude on leading wall, which is depicted in figure 6.13j and 6.13k. The first figure 6.13j is for density ratio, Δρ/ρ = 0.2 and later is for, Δρ/ρ=0.4. Consider figure 6.13j where in the Nusselt number ranges from 0.50 to 4.19, with low heat transfer being found next to top wall in the upstream region. This is because the hot fluid flows back form the outlet to the inlet sweeping top portion of the leading wall and hence heat transfer in top portion at the outlet is high, and then decreases towards the inlet. Further increase in density ratio, Δρ/ρ =0.4, simply leads to increase in heat transfer with no appreciable change in pattern of Nusselt number contours. Nusselt number attains as high as 5.24 times the corresponding Nusselt number value in stationary case (Figure 6.13k).

Effect of increasing rotation number on the trailing wall

To show the effect of rotation on heat transfer characteristic on the trailing wall, calculated Nusselt number for higher rotation number is compared with Nusselt number

obtain for stationary channel. So, again we refer back to figure 6.13a for calculated Nusselt number contours on trailing wall for stationary case. This is because; in stationary channel the heat transfer characteristic is same on both leading and trailing wall. Rotation number, Ro, is increased to 0.125 while keeping the density ratio, $\Delta\rho/\rho$ to 0.1, the calculated Nusselt number contours of this corresponding case is shown in figure 6.14d.   In this figure 6.14d, pattern of the Nusselt number contours is remarkably different from the stationary channel, with orientation of high Nusselt number contour at the beginning and bottom wall of the trailing wall. Again here a low Nusselt number contour starts appearing in the top and outlet portion of the trailing wall, and Nusselt number contour is high as 1.27 times the corresponding Nusselt number contours in stationary case. When rotation number, Ro, is increased to 0.25, while fixing the density ratio to 0.1(Figure 6.14g, case 8), the Nusselt number attains a value of 3.6 next to the bottom of the trailing wall, and Nusselt number decreases gradually to a value of 0.4 at the top. Again this low rate of heat transfer can be accredited to flow reversal, which was elaborated in the velocity and temperature section. And also, it can be noticed that Nusselt number contour equals 1.28, extending from inlet to few hydraulic diameters of the downstream, without variation in span wise direction, depicting the incurrence of flow reversal.

Effect of increasing density ratio, $\Delta\rho/\rho$ on trailing wall

In figure 6.14i, the rotation number, Ro, is kept at 0.25 and density ratio is increased to 0.2. Here the Nusselt number contour next to bottom wall attains to a value of 4.36.and again it is seen that the high and low Nusselt number contours stretched towards the upstream. In figure 6.14j, the density ratio,$\Delta\rho/\rho$ is increased further to 0.4 while keeping

the rotation number, Ro, to 0.25. Nusselt number next to bottom wall attains a value as high as 6.12 times the corresponding Nusselt number in the stationary case, and a Nusselt number contour valued 0.4 stretches to half way of the height reflecting possible depth of flow reversal. It is also noticed from figure 6.14j that a small region of high Nusselt number arises next to top and downstream of the trailing wall, which again is due to flow reversal.

Effect of channel orientation on the leading and trailing wall

Figure 6.13b and 6.13e, shows the leading wall Nusselt number contours for same rotation number, Ro=0.125, but with orientation $\beta = 90^{\circ}$ and 120°, respectively. Nusselt number contour pattern on leading wall for orthogonal orientation, are quite different form the $\beta = 120^{\circ}$, with high Nusselt number contours on top and bottom region. And after comparing with stationary case, it is found the Nusselt number obtained in the later case is higher. When trailing wall Nusselt number for case 5 (which is shown in figure 6.14d), is compared with stationary case, it is found that the Nusselt number for case 5 is 10% higher.

6.4. Spanwise averaged heat transfer coefficients

There are six figures presenting the spanwise averaged Nusselt number on leading and trailing wall for all the cases mentioned in Table 6.1. Figure 6.15 and figure 6.16, shows the Spanwise averaged Nusselt number for leading and trailing wall, respectively for case 1, 2, 3 and 4. In this figure it is seen that the Spanwise averaged Nusselt number decreases at the entry region, with increase in density ration, $\Delta\rho/\rho$. However, downstream and beyond the middle of the leading wall, the spanwise averaged Nusselt number begin

to increase slightly with increase in density ratio, $\Delta\rho/\rho$. While on trailing wall the spanwise averaged Nusselt number seem to decrease with increase in density ratio, $\Delta\rho/\rho$. Figure 6.17a and 6.17b presents the spanwise averaged Nusselt number on leading and trailing wall for the case 5, 6 and 7, in which the channel makes an angle of 120° from the rotation direction. Again it is seen that the spanwise average Nusselt number on leading and trailing wall decreases in the entry region with increase in density ratio, $\Delta\rho/\rho$. But it is seen to increase from middle and downstream of the heated sections. When rotation number, Ro, is increased to 0.25, the spanwise averaged Nusselt number increases dramatically on both leading and trailing wall with increase in density ratio, $\Delta\rho/\rho$, and at the end of the heated sections, spanwise averaged Nusselt number increases drastically showing the effect of flow reversal that can be viewed from the Figure 6.17a and 6.17b. Now, consider Figure 6.18a, which show the spanwise averaged Nusselt number on leading walls and Figure 6.18b shows spanwise averaged Nusselt number on trailing wall , for fixed density ratio, $\Delta\rho/\rho = 0.1$.It is seen from these figures that the spanwise Nusselt number increases with increase in rotation number, Ro, for both leading and trailing wall. It can be concluded that the effect of increasing density ratio is greatly felt on high rotation number than the low rotation number, Ro for channel with $\beta = 120^o$ orientation.

6.5. Comparison with experiment

To validate the results, we carried out extra simulation for rotation number, Ro, and density ratio, $\Delta\rho/\rho$, similar to that of experiments of Willet and Bergles [11], and results were shown in Figure 6.19. It can be seen that the computed Nusselt number is close to experiment data of [11] for leading wall and trailing wall. This difference can be attributed to (1) the uncertainty involved in experimental data ($\pm$ 11 percent), (2) constant

wall-heat-flux boundary condition was applied in experiments of Willet and Bergles [11]. Whereas, computed Nusselt number is based on constant wall temperature & (3) numerical errors.
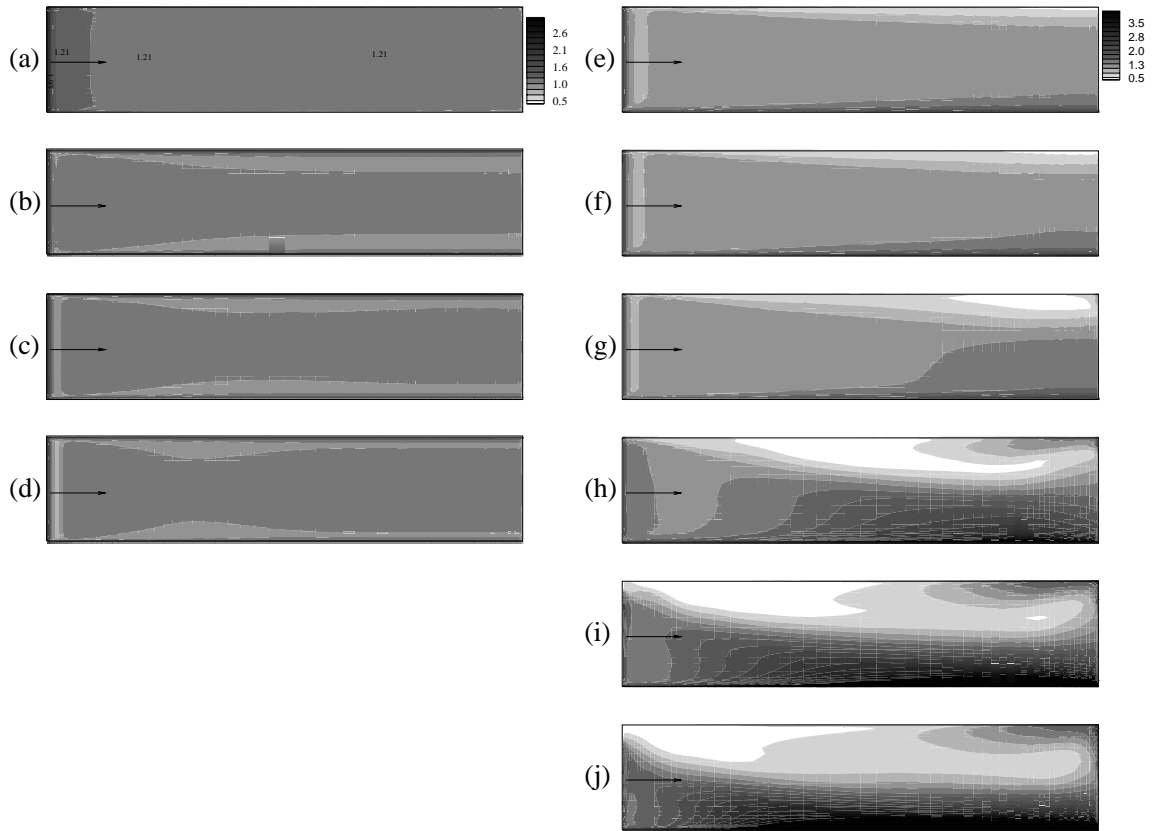
Figure 6.13: Local Nusselt distribution on leading wall. Re = 30000: (a) Ro = 0.0 and $\Delta\rho/\rho$ = 0.1; (b) Ro = 0.125, β = 90º and $\Delta\rho/\rho$ = 0.1; (c) Ro = 0.125, β = 90º and $\Delta\rho/\rho$ = 0.2; (d) Ro = 0.125, β = 90º and $\Delta\rho/\rho$ = 0.4; (e) Ro = 0.125, β = 120º and $\Delta\rho/\rho$ = 0.1; (f) Ro = 0.125, β = 120º and $\Delta\rho/\rho$ = 0.2; (g) Ro = 0.125, β = 120º and $\Delta\rho/\rho$ = 0.4; (h) Ro = 0.25, β = 120º and $\Delta\rho/\rho$ = 0.1; (i) Ro = 0.25, β = 120º and $\Delta\rho/\rho$ = 0.2; (j) Ro = 0.25, β = 120º and $\Delta\rho/\rho$ = 0.4.
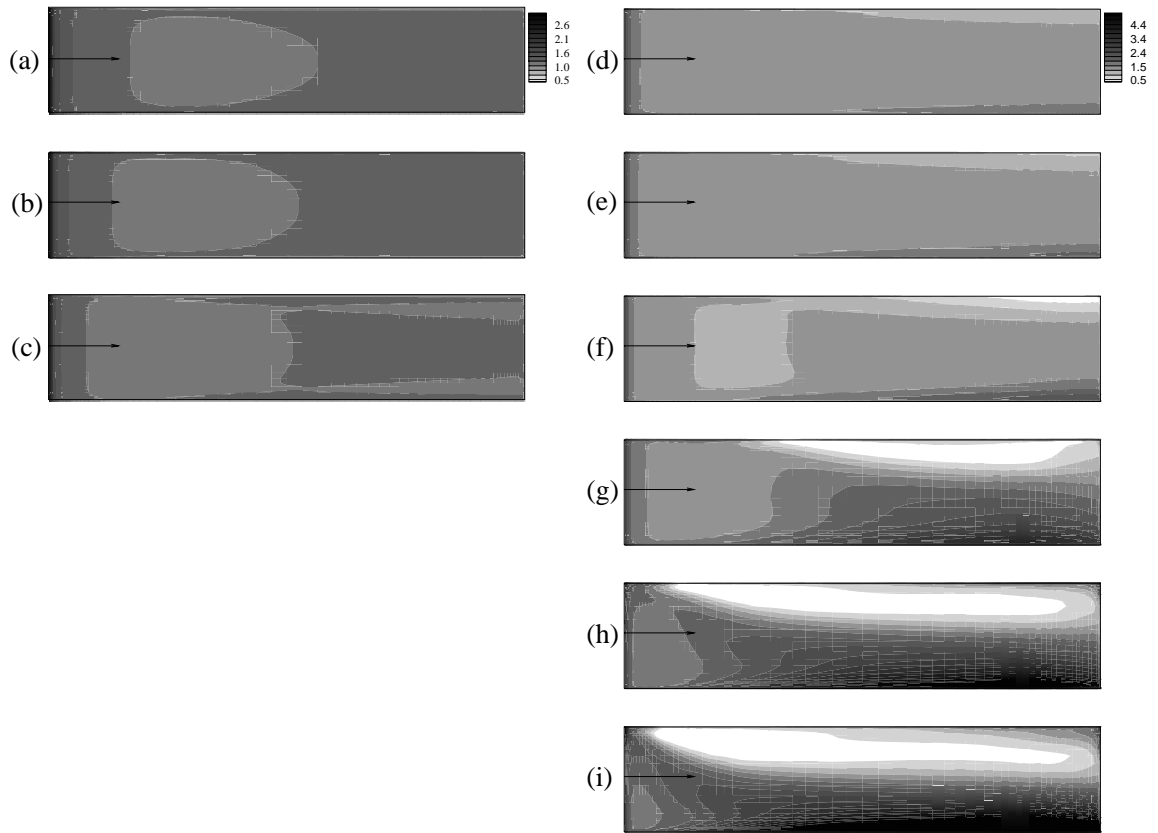
Figure 6.14: Local Nusselt distribution on trailing wall. Re = 30000: (a) Ro = 0.125, β = 90° and Δρ/ρ = 0.1; (b) Ro=0.125, β=90° and Δρ/ρ = 0.2; (c) Ro = 0.125, β = 90° and Δρ/ρ = 0.4; (d) Ro = 0.125, β =120° and Δρ/ρ = 0.1; (e) Ro = 0.125, β=120° and Δρ/ρ = 0.2; (f) Ro = 0.125, β = 120° and Δρ/ρ = 0.4; (g) Ro = 0.25, β = 120° and Δρ/ρ = 0.1; (h) Ro = 0.25, β = 120° and Δρ/ρ = 0.2; (i) Ro = 0.25, β = 120° and Δρ/ρ = 0.4.
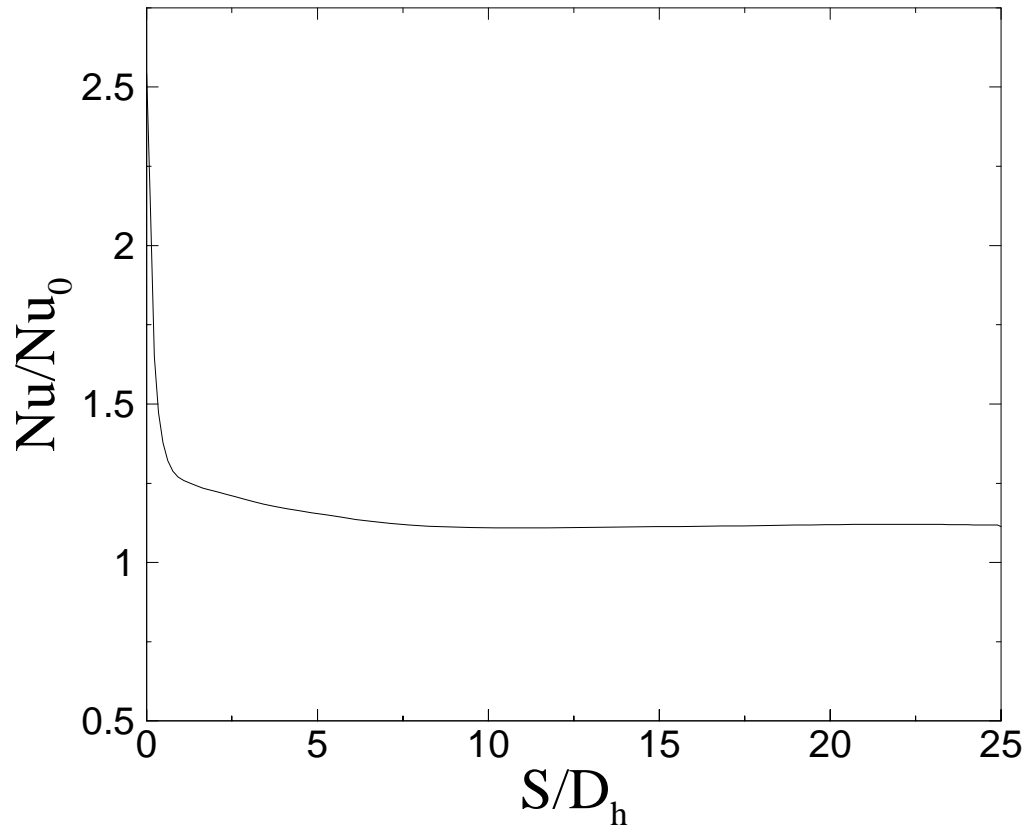
Figure 6.15: Span wise averaged Nusselt number on leading and trailing wall.
Re = 30000, Ro = 0.0 and $\Delta\rho/\rho = 0.1$.
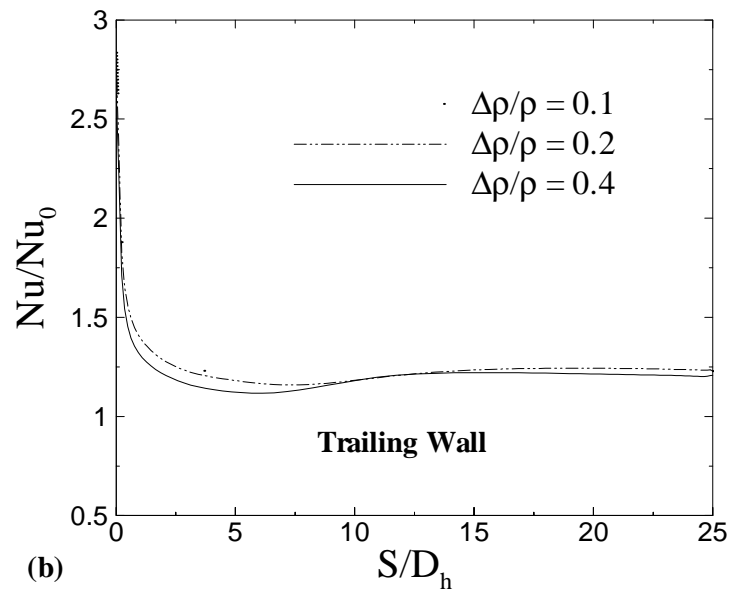
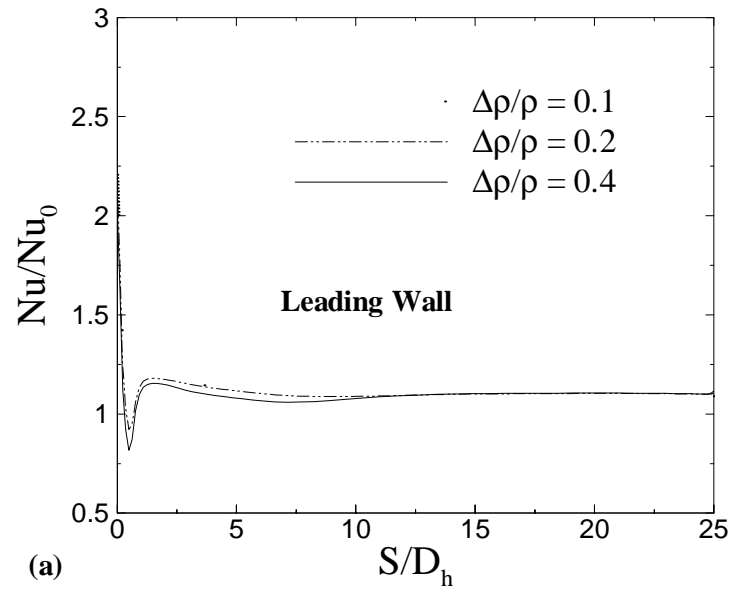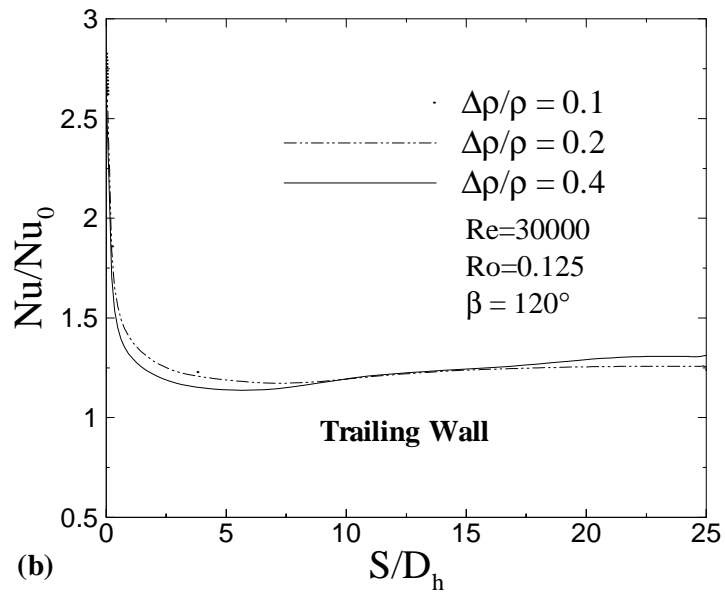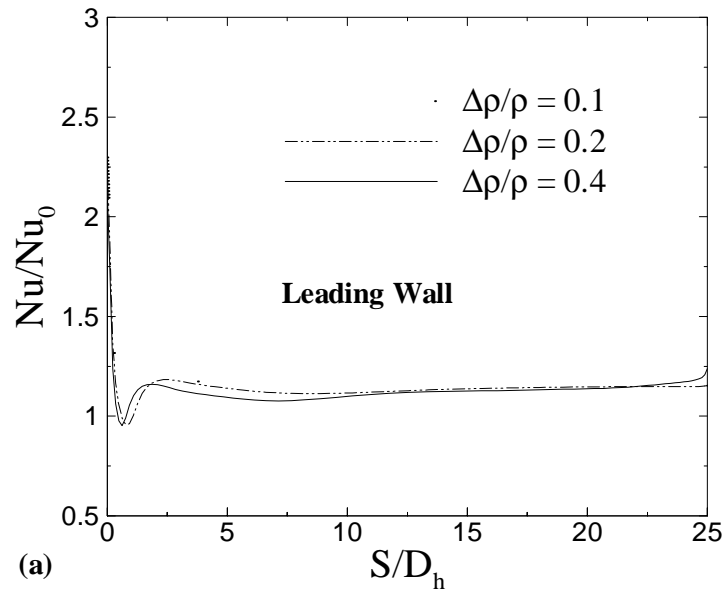Figure 6.16: Span wise averaged Nusselt number. Re = 30000, Ro = 0.125, β = 90°: (a) Leading Wall; (b) Trailing Wall.

Figure 6.17: Span wise averaged Nusselt number. Re = 30000, Ro = 0.125, β = 120°: (a) Leading Wall; (b) Trailing Wall.

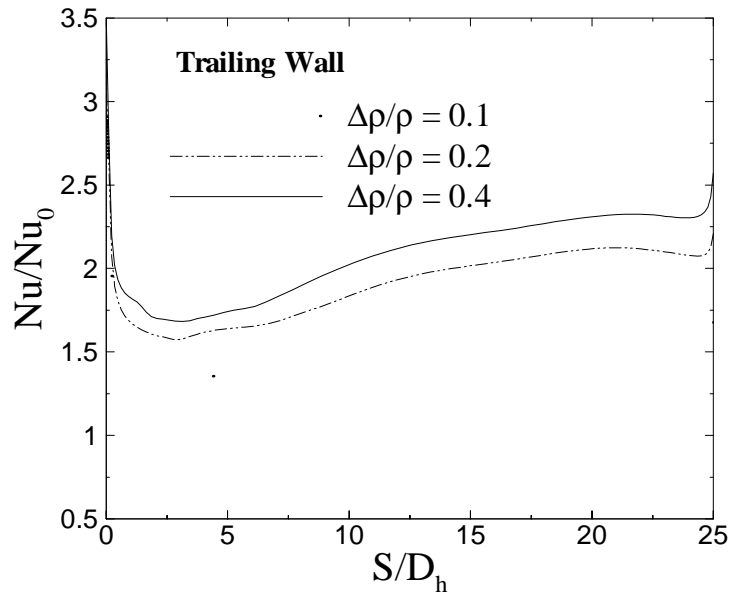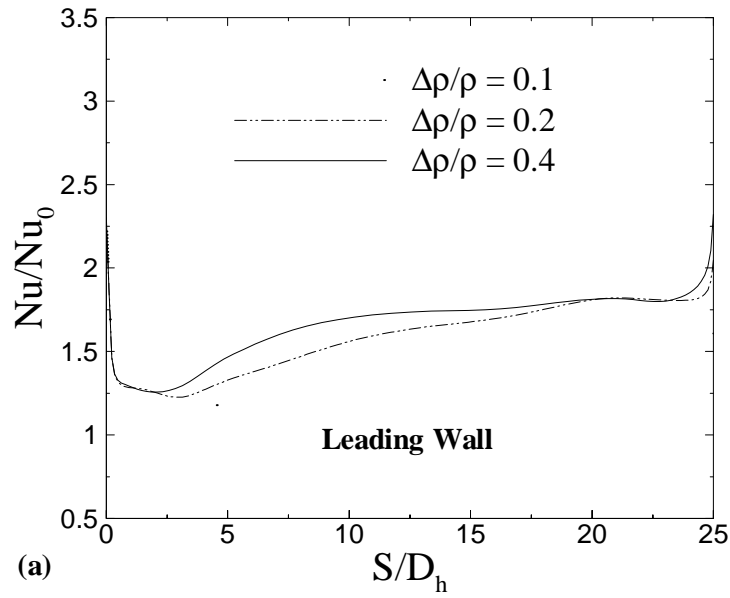Figure 6.18: Span wise averaged Nusselt number. Re = 30000, Ro = 0.25, β = 120°: (a) Leading Wall; (b) Trailing Wall.
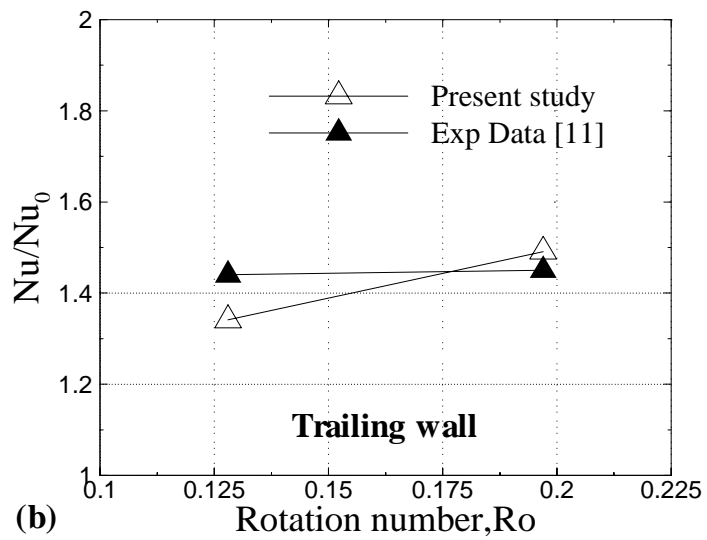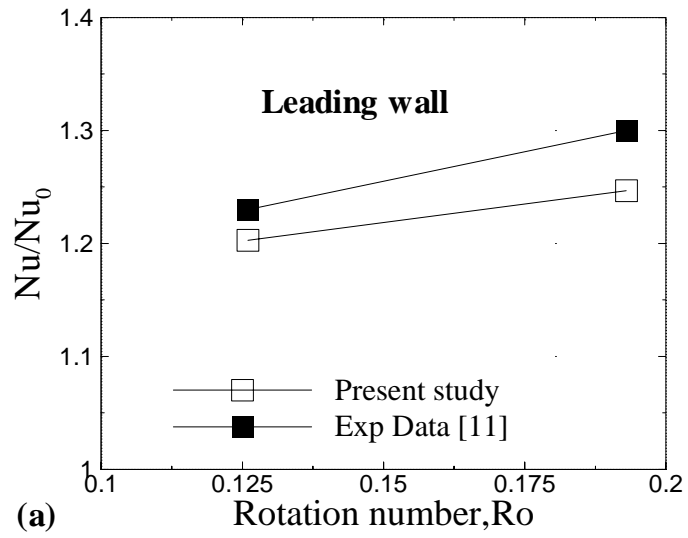
Figure 6.19: Averaged Nusselt number comparison: (a) leading wall; (b) trailing wall.

CHAPTER 7

CONCLUSIONS & RECOMMENDATIONS

7.1. Conclusions

Flow and heat transfer in rotating smooth channel with high aspect ratio (AR = 10) for various rotation number and inlet coolant-to-wall density ratios is predicted using finite volume code. Two channel orientations $\beta = 90^o$ and 120°, with two thermal boundary conditions, namely constant wall-heat flux and constant wall- temperature are studied. Reynolds stress model in conjunction with two-layer model predicted well, the heat transfer results. Results are close to experiment data of Willet and Bergles [11]. The main outcomes of this research are mentioned below.

- Using wall function to approximate flow variable near the wall did not yield satisfactory results for both stationary and rotating channel case.

- In $\beta = 90^o$ case, Coriolis force is from leading to trailing wall, thus increasing heat transfer on trailing wall. Nusselt number decreases with increase in density ratio, for fixed rotation number.

- In $\beta = 120^o$ case, Coriolis force is from top leading corner to bottom wall for low rotation number. For high rotation number and high-density ratio, Coriolis force if from trailing to leading in the top portion of the channel, thereby setting a clockwise rotating vortex.

- In $\beta = 120^o$ case, Nusselt number increase with increase in rotation number as well as density ratio. Especially, for high rotation number, Nusselt number is seen to increase dramatically with increase in density ratio.

- In $\beta = 120^o$ case, flow reversal takes place at higher rotation number and intensity and penetration of reverse flow increases with increase in density ratio.

7.2 Recommendations

There is large room for improvement in such a study.

- Improvement of the grid distribution is very essential.

- The effect of channel orientation, β, Reynolds number, Re, Prandtl number, Pr and the effect of uneven wall heat-flux/temperature would be interesting area of future research.

REFERENCES

1. Willet, F. T., 1999, "An Experimental Study of the Effects of Rotation on Convective Heat Transfer in Smooth and Pin Fin Ducts of Narrow Cross-section," Ph.D. thesis, Rensselaer Polytechnic institute.

2. Logan, E. Jr., and Roy, R., 2003, *Handbook of Turbomachinery*, Marcel Dekker, Inc., New York. Pages 134-147.

3. Morris, W. D., and Salemi, R., 1992, "An Attempt to Uncouple the Effect of Coriolis and Buoyancy Forces Experimentally on Heat Transfer in Smooth Circular Tubes That Rotate in the Orthogonal Mode," Journal of Turbomachinery, Vol. 114, pp. 858-864.

4. Han, J. C., Zhang, Y. M., and Kalkuehler, K., 1993, "Uneven Wall Temperature Effect on Local Heat Transfer in a Rotating Two-Pass Square Channel With Smooth Walls," Journal of Turbomachinery, Vol. 115, pp. 912-919.

5. Han, J. C., Zhang, Y. M., and Lee, C. P., 1994, "Influence of Surface Heating Condition on Local Heat Transfer in a Rotating Square Channel With Smooth Walls and Radial Outward Flow," Journal of Turbomachinery, Vol. 116, pp. 149-158.

6. El-Husayni, H. A., Taslim, M. E., and Kercher, D. M., 1994, "Experimental Heat Transfer Investigation of Stationary and Orthogonally Rotating Asymmetric Heated Smooth and Turbulated Channels," Journal of Turbomachinery, Vol. 116, pp. 124-132.

7. Dutta, S., and Han, J. C., 1996, "Local Heat Transfer in Rotating Smooth and Ribbed Two-Pass Square Channels With Three Channel Orientations," Journal of Turbomachinery, Vol. 118, pp. 578-584.

8. Liou, T. M., and Chen, C. C., 1999, "LDV Study of Developing Flows Through Smooth Duct With a 180 deg Straight-Corner Turn," Journal of Turbomachinery, Vol. 121, pp. 167-174.

9. Bons, J. P., and Kerrebrock, J. L., 1999, "Complementary Velocity and Heat Transfer Measurements in a Rotating Cooling Passage With Smooth Walls," Journal of Turbomachinery, Vol. 121, pp. 651-662.

10. Liou, T. M., Chen, C. C., and Chen, M. Y., 2001, "TLCT and LDV measurements if heat transfer and fluid flow in a rotating sharp turning duct," International Journal of Heat and Mass Transfer, Vol. 44, No. 9, pp. 1777-1787.

11. Willet, F. T., and Bergles, A. E., 2001, "Heat Transfer in Rotating Narrow Rectangular Ducts With Heated Sides Oriented at 60° to the r-z Plane," Journal of Turbomachinery, Vol. 123, pp. 288-295.

12. Willet, F. T., and Bergles, A. E., 2002, "Heat Transfer in Rotating Narrow Rectangular Ducts With Heated Sides Parallel to the r-z Plane," Journal of Turbomachinery, Vol. 124, pp. 1-7.

13. Howard, J. H. G., Patankar, S. V., and Bordynuik, R. M., 1980, "Flow Prediction in Rotating Ducts Using Coriolis-Modified Turbulence Models," Journal of Fluids Engineering, Vol. 102, pp. 456-461.

14. Iacovides, H., and Launder, B. E., 1991, "Parametric and Numerical Study of Fully Developed Flow and Heat Transfer in Rotating Rectangular Ducts," Journal of Turbomachinery, Vol. 113, pp. 331-338.

15. Prakash, C., and Zerkle, R., 1992, "Prediction of Turbulent Flow and Heat Transfer in Radially Rotating Square Duct," Journal of Turbomachinery, Vol. 114, pp. 835-846.

16. Tekriwal, P., 1994, "Heat Transfer Prediction With Extended K-ε Turbulence Model in Radial Cooling Ducts Rotating in Orthogonal Mode," Journal of Heat Transfer, Vol. 116, pp. 369-380.

17. Prakash, C., and Zerkle, R., 1995, "Prediction of Turbulent Flow and Heat Transfer in a Ribbed Rectangular Duct With and Without Rotation," Journal of Turbomachinery, Vol. 117, pp. 255-264.

18. Bo, T., Iacovides, H., and Launder, B. E., 1995, "Developing Buoyancy-Modified Turbulent Flow in Ducts Rotating in Orthogonal Mode," Journal of Turbomachinery, Vol. 117, pp. 474-483.

19. Dutta, S., Malcolm, J. A., and Han, J. C., 1995, "Prediction of turbulent heat transfer in rotating smooth square ducts," International Journal of Heat and Mass Transfer, Vol. 39, No. 12, pp. 2505-2514.

20. Iacovides, H., and Launder, B. E., 1995, "Computational fluid dynamics applied to internal gas-turbine blade cooling: a review," International Journal of Heat and Fluid Flow, Vol. 16, No. 6, pp. 454-470.

21. Chen, H. C., Jang, Y. J., and Han, J. C., 2000, "Computation of heat transfer in rotating two-pass square channel by a second-moment closure model," International Journal of Heat and Mass Transfer, Vol. 43, No. 9, 1603-1616.

22. Lin, Y. L., Shih, T. I. P., Stephens, M. A., and Chyu, M. K., 2001, "A Numerical Study of Flow and Heat Transfer in a Smooth and Ribbed U-Duct With and Without Rotation," Journal of Heat Transfer, Vol. 123, pp. 219-232.

23. Al-Qahtani, M., Jang, Y. J., Chen, H. C., and Han, J. C., 2002, "Flow and heat transfer in rotating two-pass rectangular channels (AR = 2) by Reynolds stress turbulence model," International Journal of Heat and Mass Transfer, Vol. 45, No. 9, pp. 1823-1838.

24. Al-Qahtani, M., Chen, H. C., and Han, J. C., 2002, "A Numerical Study of Flow and Heat Transfer in Rotating Rectangular Channels (AR = 4) With 45° Rib Turbulators by Reynolds Stress Turbulence Model," ASME Paper 2002-GT-30216.

25. Su, G., Chen, H. C., Han, J. C., and Heidmann, J. D., 2004, "Computational heat transfer in rotating two-pass rectangular channel (AR = 1:1, 1:2, 1:4) with smooth walls by a Reynolds stress turbulence model," International Journal of Heat and Mass Transfer, Vol. 47, No. 26, pp. 5665-5683.

26. Belhoucine, L., Deville, M., Elazehari, A. R., and Bensalah, M. O., 2004, "Explicit algebraic Reynolds stress model of incompressible turbulent flow in rotating square duct," Computers & Fluids, Vol. 33, pp. 179-199.

27. Al-Qahtani, M., Chen, H. C., and Han, J. C., 2004, "Flow and Heat Transfer Prediction of Rotating Rectangular Channels Using Reynolds Stress Model," Journal of Thermophysics and Heat Transfer, Vol. 18, No. 4, pp. 1823-1838.

28. Fluent-6 manual. Fluent Inc, 2003.

29. Versteeg, H.K., and Malalasekera, W., "An Introduction to Computational Fluid Dynamics", The Finite Volume Method, Longman Scientific and Technical, 1995.

30. Patankar, S. V., Computer analysis of fluid flow and heat transfer, chapter 8, pages 223-252, Pineridge press ltd., Swansea, U.K., 1981.

VITAE

- Mehaboob Basha N.B.

- Born in Bellary, Karnataka, India.

- Received bachelor's degree in Industrial & Production Engineering from Vijay Nagar Engineering College, Gulbarga University, India in September 2000.

- Completed Master's of Science in Mechanical Engineering at King Fahd University of Petroleum & Minerals, Dhahran, Saudi Arabia in October 2005.